PROPERTIES OF THE SUBDUCTION SYSTEM IN MEXICO

Thesis by

YoungHee Kim

In Partial Fulfillment of the Requirements
for the Degree of
Doctor of Philosophy

California Institute of Technology
Pasadena, California

2011
(Submitted 5/23/2011)

Acknowledgements

First of all, I would like to express my sincere gratitude to my adviser, Rob Clayton, for the continuous support of my Ph.D. study and research, and for his patience, motivation, and immsense knowledge. I greatly appreciate his accessibility and countless advice which helped me a lot to find my way through the research process. His understanding, encouragement and personal guidance have provided a good basis for the present thesis. I could not have imagined having a better adviser and mentor for my Ph.D. study.

I would like to take this opportunity to express my appreciation to Jennifer Jackson for providing me advice, guidance and creative ideas for me to explore. It was such a pleasure to work with someone who was willing to take the extra time to explain all the details and walk me through the process.

I would like to thank my academic adviser, Mike Gurnis. Mike kindly assisted me in choosing courses and selecting committee members. I particularly appreciate him for trying to find time to discuss course progress and always giving me insightful comments regarding my thesis work.

I would like to thank my thesis committee for taking the time to read this thesis and providing me with useful comments. Particularly I appreciate Joann Stock, who kindly agreed to be a substitute committee member. I would also like to thank Don Helmberger and Jean-Philippe Avouac for their insightful comments on my thesis project at my thesis committee meeting.

I would like to thank Paul Asimow, Sung Keun Lee from Seoul National University, Eugene Humphreys from University of Oregon, and Geoff Abers from Lamont-Doherty Earth Observatory for helping me with the petrology and mineralogy of the subducting oceanic crust. I thank them for stimulating conversations exploring other likely scenarios for Mexico subduction zone.

I would like to thank the rest of faculty members at Caltech and other institutions from whom I took/audited courses. In alphabetical order, I would like to thank Jean-Paul Ampuero, Andy Ingersoll, Nadia Lapusta, Malcolm Sambridge, Peter Shearer, Mark Simons, Albert Tarantola, and Paul Wennberg for their great courses. I would like to thank Jason and Zorka Saleeby for their hospitality and great tour of the Hawaii island when I visited Hawaii for the Pahoehoe trip in March 2011.

My very sincere thank you goes to Jeoren Tromp at Princeton University for offering me challenging research topics and leading me to work on exciting projects while he stayed at Caltech. I have learned so much knowledge from him that will help me for my future in seismology or whatever path my career takes.

I am indebted to many of my colleagues who supported me and kept me good company for the past six years at Caltech. I would like to first thank Eunseo Choi, who convinced me to come to Caltech and helped me to settle down into a completely new environment during my first year at Caltech. I would like to thank Ting Chen, Lijun Liu, Michelle Selvans, Sonja Spasojevic, and Daoyuan Sun who made my my time here at Caltech enjoyable. I would like to thank Zhimei Yan, for her wonderful matlab codes and scripts. I would like to thank Min Chen, Vala Hjorleifsdottir, Leif Strand, and Carl Tape who helped me a lot during the initial stage of my Ph.D. when I worked with Jeroen Tromp. A huge thank you goes to Qinya Liu, who helped me tremendously on the manuscript that we finally put together. I appreciate her taking the time out of numerous discussions on many aspects of the adjoint analysis. I would like to thank Tehru Alex Song for fruitful collaboration while discussing receiver function results. I would also like to thank Fraser Keppie for helping me with the analysis on the Yucatan slab. Many thanks go to my current and past officemates: Chris Dicaprio, Vala Hjorleifsdottir, Florence Levy, Lijun Liu, Francois Thibout, Lingsen Meng, Yihe Huang, Asaf Inbal, and Brent Minchew (in order of appearance).

I am so grateful to the secretaries and librarians in the GPS division for helping the department to run smoothly and for assisting me in many different ways. Viola Carter, Donna Mireles, Rosemary Miller, Dian Buchness, Marcia Hudson, Heather Steele, Lisa Christiansen, Tony Diaz, and Jim O'Donnell deserve special mention. I would like to thank GPS IT support team: Jian (Ken) Ou, Scott Dungan and Mike

Black.

Lastly, and most importantly, I warmly thank my parents for their unconditional trust in my personal and professional development and their support throughout my life. Without my parents' constant support and love, this thesis would not have been possible. I thank my parents and parents-in-law for staying with me to raise my son, Logan, for brief periods of time whenever I needed help the most. I am so grateful that I have very understanding parents-in-law, and I appreciate their willingness to help me anytime. I would like to thank my sister YangHee who is always willing to listen to my concerns and do silly things together. Congratulations on your marriage, and I wish for your happiness and success in life, YangHee! My husband, JongHan, deserves my deepest appreciation. I thank JongHan for putting up with me for more than eight years. I thank him for being such a good friend and mentor of my life. I have been extremely happy during my Ph.D. because of Logan, and I am sure that he would be very proud of me someday for completing my thesis at Caltech. I would like to dedicate this thesis to my parents in Korea, my husband, JongHan, and my son, Logan (Joonyoung).

Abstract

This thesis presents seismic imaging results of the structure of the Mexican subduction zone using receiver function (RF) based on teleseismic P-to-S converted waves, in order to gain insight into the physical and chemical factors associated with internal geodynamic processes. More specifically, this thesis investigates (1) the nature of tectonic processes involved in the buildup and subsequent modification of continental and oceanic lithosphere, and (2) the determination of mineralogy/petrology and fluid-phase reactions in the subducting Cocos oceanic crust.

Utilizing the data acquired from two dense broadband seismic lines in Mexico, the geometries and seismic properties of the interface of the subducting Cocos plate beneath Mexico are determined from the RFs. The RF image for central Mexico shows that the subducting oceanic crust dips shallowly north at 15 degrees for a distance of 80 km from Acapulco at the Pacific coast, and then horizontally underplates the continental crust for approximately 200 km to the Trans-Mexican Volcanic Belt (TMVB). Modeling of the RF conversion amplitudes and timings of the underplated features reveals a thin very-low velocity zone between the plate and the continental crust that appears to absorb nearly all of the strain between the upper plate and the slab. The migrated image of the RFs shows that the slab dips steeply into the mantle at an angle of about 75 degrees beneath the TMVB.

The RF results for southern Mexico in the Isthmus of Tehuantepec show an image of the Cocos slab down to about 100 km depth. The same cross-section image also reveals a slab-like south-dipping structure interpreted to be subducted from the Gulf of Mexico. This anomalous slab with the opposite dip direction of the Cocos slab appears to cut off the Cocos slab at 150 km depth. There is no tectonic explanation for the south-dipping slab under the current paradigm of Caribbean plate reconstructions. We present in this thesis the case for a new reconstruction of the Gulf of Mexico and propose that the slab may be due to the collision of the Yucatan Block into Mexico in the Miocene, and may also be responsible for the Cocos plate truncation imaged from previous tomography studies. This hypothesis explains the Chiapas Fold and Thrust Belt to the south of the Yucatan Block and may explain the unusual volcanic arc configuration in southern Mexico.

We formulate and apply a new inversion technique based on the plane wave conversion to obtain the seismic parameters (S wave velocity, Vs, and density) of the oceanic crust. We use such parameters to infer mineralogical properties of subducting oceanic crust. From this effort, we provide tighter constraints on physical properties of the subducting Cocos oceanic crust, and explain the difference in the slab geometries betweeen central and southern Mexico from the mineral physics point of view. Anomalously low Vs (2.4−3.4 km/s) in the upper part of the flat oceanic crust in central Mexico points to elevated Poisson's and Vp/Vs ratios of the oceanic crust. This directly relates to the presence of water and hydrous minerals or high pore pressure; the mechanically weak hydrous layer may explain current subduction geometry at very shallow depth of about 45 km without strong coupling between the plates.

Using Vp/Vs as a function of Vs in a range of likely pressure and temperature for candidate hydrous phases, we identify the major hydrous mineral phases present in the upper (3−5 km thickness) and lower parts (3−5 km thickness) of the subducted oceanic crust of central and southern Mexico. In central Mexico, the upper oceanic crust in the flat slab region is enriched with hydrous minerals such as talc over the normal oceanic crustal compositions such as MORB-like gabbro. Petrologically, the generation of talc during subduction of the oceanic crust is nearly impossible. One possible mechanism to produce such a low-velocity anomaly at the upper oceanic crust is that lower crustal rocks are hydrated with 15-20 percent of free water to reduce the seismic velocities significantly. We thus propose that the thin low-velocity, talc-rich layer in the upper oceanic crust is then generated from the mantle wedge side during the slab flattening process coupled with trench rollback. The talc-rich rocks at the slab interface can be formed in the mantle by the addition of silica transported by rising fluids via the dehydration reaction from the subducting oceanic crust and by mechanical mixing of mantle and siliceous rocks. The evolution of the thin low-strength zone, which decouples the horizontal slab from the continental crust, originating from the mantle wedge side rather than the trench side, has important implications for the dynamics of the subduction system, including the flattening process of the slab, as well as the geochemistry of the mantle wedge and arc in central Mexico. After passing through the flat segment, the major compositions of the steeply subducting oceanic crust underneath the TMVB are zoisite and lawsonite from 60 to 100 km in depth. The eclogitization occurs at the depth of about 100 km. The dominant mineral phase in the upper oceanic crust of southern Mexico from 45 to 120 km depth is amphibole on top of unaltered gabbroic oceanic crust.

Contents

List of Figures

Introduction

Understanding the coupling at the plate boundary is crucial to studying the dynamics of plate tectonics and continental evolution. Continuous deployment of dense portable and permanent seismic arrays near the plate boundary provides critical observations of the lithosphere, asthenosphere and upper mantle structures. Such observations from seismic imaging are a key to understanding the physical and chemical factors associated with internal geodynamic processes in the subduction zone. In particular, the distinguishing feature in the subducted oceanic crust and the mantle is the presence of hydrated phases, which transport water into the Earth's interior (Abers, 2000; Hacker et al., 2003; Jacobsen & van der Lee, 2006; Maruyama & Okamoto, 2007; Mainprice & IIdefonse, 2009). The seismological evidence of the hydrous phases in the subducted oceanic crust in various subduction environments is shown as a reduction in seismic velocities of about $\sim 5-20$ percent compared to surrounding mantle (Yuan et al., 2000; Jacobsen & van der Lee, 2006; Kawakatsu & Watada, 2007; Audet et al., 2009). The depth of such a low seismic velocity zone in the oceanic crust typically varies with the plate thermal history. In this thesis, I show the present-day structure of the Mexico subduction system by mapping seismic discontinuities using the dense seismic array data and by determining candidate hydrous minerals present in the oceanic crust under different pressure (P) and temperature (T) conditions.

Two passive seismic experiments were carried out in central and southern Mexico, respectively, to image the structure of the subducting Cocos plate and investigate different subduction processes along the Middle American Trench (MAT). The data set from 100 broadband seismic stations from March 2005 to February 2007 in central Mexico and 45 stations in southern Mexico from July 2007 to October 2009 is processed for imaging.

In Chapter 1, I present the seismic image of the overall subduction structure including the continental/mid crust, oceanic crust, and upper mantle, using receiver functions (RFs) based on the teleseismic P-to-S converted phases (Pérez-Campos et al., 2008; Kim et al., 2010). Teleseismic signals provide useful information on the nature and structure of the lithosphere and tectonic processes that have contributed to its evolution. Changes in velocity, density, or anisotropy within the crust and mantle scatter upcoming seismic waves and partially convert P waves into S waves to reveal the seismic discontinuities. The sharp increase or decrease in both velocity and density with depth at discontinuities such as the Moho and slab/crustal interfaces can be mapped. In our RF analysis, I use high-frequency seismograms (filtered at 1 s) to analyze any fine-scale features in the subduction system with the highest resolution. This enables us to divide the subducted oceanic crust into two layers (upper and lower oceanic crusts) and to further characterize each layer separately from a seismological-mineral physics perspective. Back-azimuth stacking (Zhu & Kanamori, 2000), either by itself or as a part of depth migration (Kim et al., 2010), is incorporated to suppress the noise as well as to provide higher confidence in our results.

Analyzing seismic data recorded at 100 stations in central Mexico, I present the RF image that shows, for the first time, the Cocos slab in central Mexico that horizontally underplates the base of the continental crust for about 200 km. The northern portion of the profile, more distant from the trench, shows a single strong Moho interface between the continental crust and mantle wedge, that is, a positive velocity transition with depth (Pérez-Campos et al., 2008; Kim et al., 2010). The southern portion, closer to the trench, shows a horizontal interface that has a distinct negative transition over a positive one (Pérez-Campos et al., 2008; Kim et al., 2010). This negative feature is a thin low-velocity zone (2.4-3.4 km/s with a thickness of 4±1 km) or low-viscosity channel, LVC (Manea & Gurnis, 2007) between the lower continental crust and the slab, which is likely to be altered oceanic crust or a mantle wedge remnant (Pérez-Campos et al., 2008; Kim et al., 2010). This thin low-velocity layer may play an important role in explaining the unique, flab slab geometry at a shallow depth ($\sim$45 km) with very low tectonic coupling between plates (Nieto-Samaniego et al., 2006; Morán-Zenteno et al., 2007). My contribution to Pérez-Campos et al. (2008) is in depth analysis of RFs and the finite-difference (FD) modeling for the central Mexico subduction zone. This results in the construction of Figure 2 of Pérez-Campos et al. (2008). Kim et al. (2010) includes extended work including RF migration, FD modeling and RF amplitude inversion for the seismic parameters.

In Chapter 2, I present the RF image showing Cocos slab and a south-dipping slab (denoted hereafter as the Yucatan slab) from the Gulf of Mexico by analyzing data recorded at 50 stations in southern Mexico. This is the opposite dip direction of the Cocos slab, and the Yucatan slab appears to cut off the Cocos slab at 150 km depth. The slab is also visible in a previous global tomographic model by Li et al. (2008). The resolution of the tomographic models is poor at this scale, but they do confirm the existence of the Yucatan slab and that it continues farther to the southeast of the seismic line. The local upper mantle seismicity follows the trend of the Yucatan slab starting at the intersection point with the Cocos slab. There is no tectonic explanation for the Yucatan slab under the current paradigm of Caribbean plate reconstructions. Chapter 2 presents the case for a new reconstruction of the Gulf of Mexico, which will affect the tectonics, geology and oceanography of the Gulf as well as the models for the Caribbean plate. We propose that the Yucatan slab arose from the collision of the Yucatan Block into Mexico at approximately 12 Ma. This scenario would explain the Chiapas Fold and Thrust Belt to the south of the Yucatan Block as the product of this collision, and its age constrains the date of the event to be Miocene (Mandujano-Velazquez & Keppie, 2009).

Knowledge of the material properties (seismic velocities and densities) of mineral phase assemblages plays a central role in interpretation of geophysical observations and geodynamic simulations. The amplitudes of the distinct negative and positive signature of the RF pulses from the top and bottom interfaces of the oceanic crust are used to constrain the S wave velocity (Vs) and density of the low-velocity layer (Kim et al., 2010). The initial pulse depends on the Vs and density contrasts between upper oceanic crust and the layer above it, while the following pulse depends on the contrast in these quantities between lower oceanic crust and the layer below it. The inverted velocities are directly compared to predicted velocities of possible mantle mineral phases using the elastic constants, which were previously constrained experimentally, and the finite strain theory (Duffy & Anderson, 1989) at a range of likely P and T. In cases where the inverted Vs and density are highly sensitive to choice of seismic parameters of the layer above/below the oceanic crust (for instance, underneath the Trans-Mexican Volcanic Belt, TMVB) I approach the problem from a Bayesian perspective, allowing us to completely characterize the model parameter space by computing allowable models instead of seeking a single optimum model. The Bayesian approach to the inverse problem yields an estimate of the probability density function of all the possible input models, which can then be propagated through the forward model to determine the Vs and densities and their associated uncertainty distributions.

In Chapters 1 and 4, the Vs determined for the flat segment of central Mexico's oceanic crust is anomalously low, and the candidate mineral phase such as talc (a low-strength hydrous mineral) is proposed for such a low speed at the depth of the flat slab (∼45 km) and a range of likely T (500−800°C) (Kim et al., 2010). The lower oceanic crustal compositions are suggested to be MORB-like gabbro over depleted mantle rock (Kim et al., 2010). In Chapter 4, I discuss the constructions on the generation of talc. Producing talc by oceanic crustal subduction at the MAT is not possible unless the lower continental crust is hydrated with unreasonably high amount of free water. We thus propose that the talc-rich layer in the upper oceanic crust can be generated from the mantle wedge side during the slab flattening process coupled with trench rollback since 17−12 Ma (Ferrari et al., 1999). Manea & Gurnis (2007) propose that dehydration of subducting lithosphere lowers the viscosity on top of the subducting slab, and show that the LVC has a significant influence on slab evolution based on numerical models. The talc-rich rocks at the slab interface can be formed in the mantle by the addition of silica transported by rising fluids via the dehydration reaction and by mechanical mixing of mantle and siliceous rocks (Peacock & Hyndman, 1999; Moore & Rymer, 2007; Moore & Lockner, 2008; Wang et al., 2009). If the thin low-strength zone originates from the mantle wedge side rather than from the trench side, this has important implications for the dynamics of the subduction system including the flattening process of the slab as well as the geochemistry of the mantle wedge and arc in central Mexico.

Using Vp/Vs as a function of Vs in a range of likely P and T for candindate hydrous phases, in Chapter 3 I conclude that the major mineral phases at 60 to 100 km depth in the oceanic crust in central Mexico are zoisite and lawsonite. The candidate rocks in the oceanic crust at deeper depth (100 to 200 km) are gabbro and eclogite. Based on the inverted Vs and Vp/Vs ratio, seismic and mineral physics analysis suggests that central Mexico is hydrous, and in particular, the volcanic arc is consistent with the observations in central Mexico. The release of H_2O via dehydration could be in the form of a fluid phase or could lower the melting temperature of surrounding phases. Either scenario correlates well with the arc volcanism at the TMVB directly above the slab.

Bibliography

Abers, G. A., 2000. Hydrated subducted crust at 100−250 km depth, *Earth Planet. Sci. Lett.*, **176**, 323–330.

Audet, P., Bostock, M. G., Christensen, N. I., & Peacock, S. M., 2009. Seismic evidence for overpressured subducted oceanic crust and megathrust fault sealing, *Nature*, **457**, 76–78.

Duffy, T. S. & Anderson, D. L., 1989. Seismic velocities in mantle minerals and the mineralogy of the upper mantle, *J. Geophys. Res.*, **94**(B2), 1895–1912.

Ferrari, L., López-Martinez, M., Aquirre-Díaz, G., & Carrasco-Niúñez, G., 1999. Space-time patterns of Cenozoic arc volcanism in central Mexico: From the Sierra Madre Occidental to the Mexican Volcanic Belt, *Geology*, **27**(4), 303–306.

Hacker, B. R., Peacock, S. M., Abers, G. A., & Holloway, S. D., 2003. Subduction factory 2. Are intermediate-depth earthquakes in subducting slabs linked to metamorphic dehydration reactions?, *J. Geophys. Res.*, **108**(B1), 1–20.

Jacobsen, S. D. & van der Lee, S., 2006. *Earth's Deep Water Cycle*, American Geophysical Union, Washington, DC.

Kawakatsu, H. & Watada, S., 2007. Seismic evidence for deep-water transportation in the mantle, *Science*, **316**, 1468–1471.

Kim, Y., Clayton, R. W., & Jackson, J. M., 2010. Geometry and seismic properties of the subducting Cocos plate in central Mexico, *J. Geophys. Res.*, **115**(B6), 1–22.

Li, C., van der Hilst, R. D., Engdahl, E. R., & Burdick, S., 2008. A new global model for P wave speed variations in Earth's mantle, *Geochem. Geophys. Geosyst.*, **9**(5), 1–21.

Mainprice, D. & IIdefonse, B., 2009. *Subduction Zone Geodynamics*, pp. 63–84, Springer.

Mandujano-Velazquez, J. & Keppie, J. D., 2009. Middle Miocene Chiapas fold and thrust belt of Mexico: a result of collision of the Tehuantepec Transform/Ridge with the Middle America Trench, *Geol. Soc. Spec. Publ.*, **327**, 55–69.

Manea, V. C. & Gurnis, M., 2007. Subduction zone evolution and low viscosity wedges and channels, *Earth Planet. Sci. Lett.*, **264**, 22–45.

Maruyama, S. & Okamoto, K., 2007. Water transportation from the subducting slab into the mantle transition zone, *Gondwana Res.*, **11**, 148–165.

Moore, D. E. & Lockner, D. A., 2008. Talc friction in the temperature range 25°−400°C: Relevance for fault-zone weakening, *Tectonophysics*, **449**, 120–132.

Moore, D. E. & Rymer, M. J., 2007. Talc, serpentinite, and the creeping section of the San Andreas fault, *Nature*, **448**, 795–797.

Morán-Zenteno, D. J., Cerca, M., & Keppie, J. D., 2007. The Cenozoic tectonic and magmatic evolution of southwestern Mexico: Advances and problem interpretation, *Spec. Pap. Geol. Soc. Am.*, **422**, 71–91.

Nieto-Samaniego, A. F., Alaniz-Álvarez, A. S., Silva-Romo, G., Eguiza-Castro, M. H., & Mendoza-Rosales, C., 2006. Latest Cretaceous to Miocene deformation events in the eastern Sierra Madre del Sur, Mexico, inferred from the geometry and age of major structures, *Geol. Soc. Am. Bull.*, **118**, 238–252.

Peacock, S. M. & Hyndman, R. D., 1999. Hydrous minerals in the mantle wedge and the maximum depth of subduction thrust earthquakes, *Geophys. Res. Lett.*, **26**(16), 2517–2520.

Pérez-Campos, X., Kim, Y., Husker, A., Davis, P. M., Clayton, R. W., Iglesias, A., Pacheco, J. F., Singh, S. K., Manea, V. C., & Gurnis, M., 2008. Horizontal subduction and truncation of the Cocos Plate beneath central Mexico, *Geophys. Res. Lett.*, **35**(18), 1–6.

Wang, X., Zeng, Z., Liu, C., Chen, J., Yin, X., Wang, X., Chen, D., Zhang, G., Chen, S., Li, K., & Ouyang, H., 2009. Talc-bearing serpentinized peridotites from the southern Mariana forearc: Implications for aseismic character within subduction zones, *Chinese J. Oceanol. Limnol.*, **27**(3), 667–673.

Yuan, X., Sobolev, S. V., Kind, R., Oncken, O., Bock, G., Asch, G., Schurr, B., Graeber, F., Rudloff, A., Hanka, W., Wylegalla, K., Tibi, R., Haberland, C., Rietbrock, A., Giese, P., Wigger, P., Röwer, P., Zandt, G., Beck, S., Wallace, T., Pardo, M., & Comte, D., 2000. Subduction and collision processes in the Central Andes constrained by converted seismic phases, *Nature*, **408**, 958–961.

Zhu, L. & Kanamori, H., 2000. Moho depth variation in southern California from teleseismic receiver functions, *J. Geophys. Res.*, **105**(B2), 2969–2980.

Chapter 1

Geometry and Seismic Properties of the Subducting Cocos Plate in Central Mexico

Published by YoungHee Kim, Robert W. Clayton, and Jennifer M. Jackson (2010) in *Journal of Geophysical Research*, *115*, B06310, doi:10.1029/2009JB006942. Reproduced by permission of American Geophysical Union.

Abstract

The geometry and properties of the interface of the Cocos plate beneath central Mexico are determined from the receiver functions (RFs) utilizing data from the Meso America Subduction Experiment (MASE). The RF image shows that the subducting oceanic crust is shallowly dipping to the north at 15° for 80 km from Acapulco and then horizontally underplates the continental crust for approximately 200 km to the Trans-Mexican Volcanic Belt (TMVB). The crustal image also shows that there is no continental root associated with the TMVB. The migrated image of the RFs shows that the slab is steeply dipping into the mantle at about 75° beneath the TMVB. Both the continental and oceanic Moho are clearly seen in both images, and modeling of the RF conversion amplitudes and timings of the underplated features reveals a thin low-velocity zone between the plate and the continental crust that appears to absorb nearly all of the strain between the upper plate and the slab. By inverting RF amplitudes of the converted phases and their time separations, we produce detailed maps of the seismic properties of the upper and lower oceanic crust of the subducting Cocos plate and its thickness. High Poisson's and Vp/Vs ratios due to anomalously low S wave velocity at the upper oceanic crust in the flat slab region may indicate the presence of water and hydrous minerals or high pore pressure. The evidence of high water content within the oceanic crust explains the flat subduction geometry without strong coupling of two plates. This may also explain the nonvolcanic tremor (NVT) activity and slow slip events (SSEs) occurring in the subducting plate and the overlying crust.

1.1 Introduction

The Cocos plate has been subducting underneath the North American plate in this present geometry at a rate of about 12 cm/yr from 20 Ma to 11 Ma and 6 cm/yr from 11 Ma to present (from EarthByte poles (*Müller et al.*, 2008)). The subduction interface has a strong variation in along-strike dip angles along the central part of Middle American Trench (MAT). To the northwest near the Rivera Plate junction, the dip is 50°, while to the southeast near the Tehuantepec Ridge it is 30° (*Pardo and Suárez*, 1995). As shown in *Pérez-Campos et al.* (2008), the slab at the central part near Acapulco is horizontal. The along-strike change in dip is evident in the trace/strike of the Neogene volcanic arc (TMVB), which trends at a 17 degree angle to the trace/strike of the trench. At 30 Ma, the volcanism ceased in the Miocene arc along the coast, and after a 10 Ma hiatus, reappeared just south of Mexico City and proceeded to migrate to the northern end of the TMVB (*Ferrari*, 2004). Since that time, the slab in central Mexico has apparently been rolling back, as evidenced by the southward migration of TMVB volcanism, to its current location at the south edge of the TMVB.

There have been a number of studies of the Cocos plate subduction especially regarding the slab geometry in central Mexico. *Couch and Woodcock* (1981) described offshore seismic, gravity, and magnetic measurements near Acapulco and suggested a 9 km thick oceanic crust dipping 2° under the continental margin. *Valdes-Gonzalez and Meyer* (1996) provided a model which includes the continental Moho of 45 km and 10° dipping slab with 8 km thickness between the Pacific coast and Mexico City using the Petatlán earthquake aftershocks. *Pardo and Suárez* (1995) described the shallow slab subduction at distances of between 110 km to 275 km from the MAT based on relocated hypocenters of local earthquakes. The work by *Kostoglodov et al.* (2003) further supported the shallow slab subduction by providing a more precise geometry of the subducting Cocos plate up to 200 km from the MAT constrained by the seismicity and gravity data. None of the studies resolved the slab geometry underneath the TMVB because there is very little seismicity away from the seismogenic zone adjacent to the trench.

There are several geochemical studies that infer the fate of the descending slab underneath the TMVB (after 250 km from the MAT) after the shallow subduction near the coast. *Ferrari* (2004) proposed a slab detachment model beneath the TMVB to explain a short (2−3 Myr) eastward-migrating mafic pulse in the late Miocene based on several volcanic and geochemical features of central Mexico. The tear in the slab due to the strong coupling between the Magdalena microplate and the overriding North American plate propagated eastward (*Ferrari*, 2004). Lateral propagation of such a slab detachment episode induced hot subslab material to flow into the slab window causing the volcanism with unusual geochemical features for a subduction setting (*Ferrari*, 2004). Reported adakite observation in the TMVB also supports this. Some adakitic observations are for early Miocene TMVB volcanism (*Gómez-Tuena et al.*, 2008). *Kay* (1978) first attributed adakites to the interaction of a large ion lithophile element-rich hydrous melt from the subducted oceanic crust with overlying mantle, and then eruption without interaction with the island arc crust. According to *Ferrari et al.* (2001), the lavas with such compositions may have been produced by small amounts of melting of a heterogeneous mantle fluxed by fluids released by the subducting slab.

In 2005, the Meso American Subduction Experiment (MASE) was deployed to image the structure of the system and to provide the parameters for a geodynamical model of the subduction process. Approximately 2 years of broadband seismic data were collected at 100 stations along a 550 km transect through Mexico City from Acapulco on the Pacific side to a point 100 km from the Gulf of Mexico, near Tampico. The north-trending transect is oriented nearly perpendicular to the MAT. The geometry of the experiment is shown in Figure 1.1.

The density of the MASE survey (∼6 km station spacing) enables the use of teleseismic converted waves to accurately image the slab and (oceanic and continental) Moho. The receiver functions (RFs) are well suited to constrain the depths of major boundaries such as the top of the subducting slab, the oceanic crust-mantle interface of the slab, and the base of continental crust in the overlying plate. *Pérez-Campos et al.* (2008) provided a back-projected RF image of the slab and crustal structure to a depth of 100 km. In this study, we will show stacked RF images obtained for different back azimuth event groups. We expand our work on RFs to do a Kirchoff-like migration/inversion using teleseismic earthquakes to image the structures underneath the

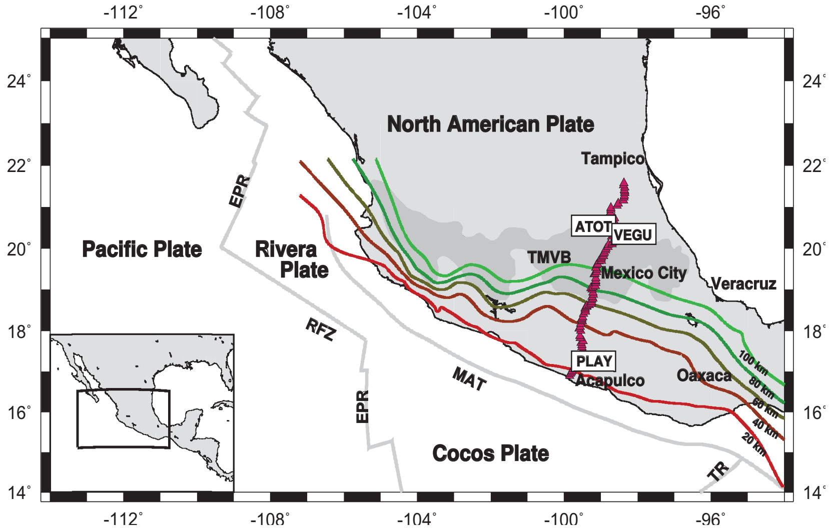

Figure 1.1: Map showing the region of the study and stations in the MASE array indicated as red triangles. The abbreviations shown in the map are EPR, East Pacific Rise; MAT, Middle American Trench; RFZ, Rivera Fracture Zone; TR, Tehuantepec Ridge; TMVB, Trans-Mexican Volcanic Belt. Isodepth contours of the subducted Cocos plate (*Pardo and Suárez*, 1995) are shown. Note that the first station of the MASE array is located at Acapulco (~75 km from the MAT), and the horizontal axis of the RF images are all plotted in reference to that station.

TMVB to a depth of 250 km. The technique is similar to that used by *Bostock et al.* (2002) for the Cascadian subduction zone. In addition, we provide a seismic velocity model from the finite-difference (FD) modeling on the horizontal interface between the lower continental crust and the top of the subducting Cocos plate suggested by *Pérez-Campos et al.* (2008). Last, we will describe a technique to determine and map seismic properties and thickness of the top interface of the Cocos plate using the P-to-S converted phases.

1.2 Data Analysis

1.2.1 Teleseismic Data

The location of the stations in the MASE array is shown in Figure 1.1. For the RF analysis, the data includes 34 earthquakes of magnitude greater than 6.1 that generally occur in three different back azimuth groups from the MASE array (Figure 1.2). After a careful selection based on the signal-to-noise ratio, individual waveform data are time windowed to 90 s, band-pass filtered from 0.01 to 1 Hz, and rotated to radial

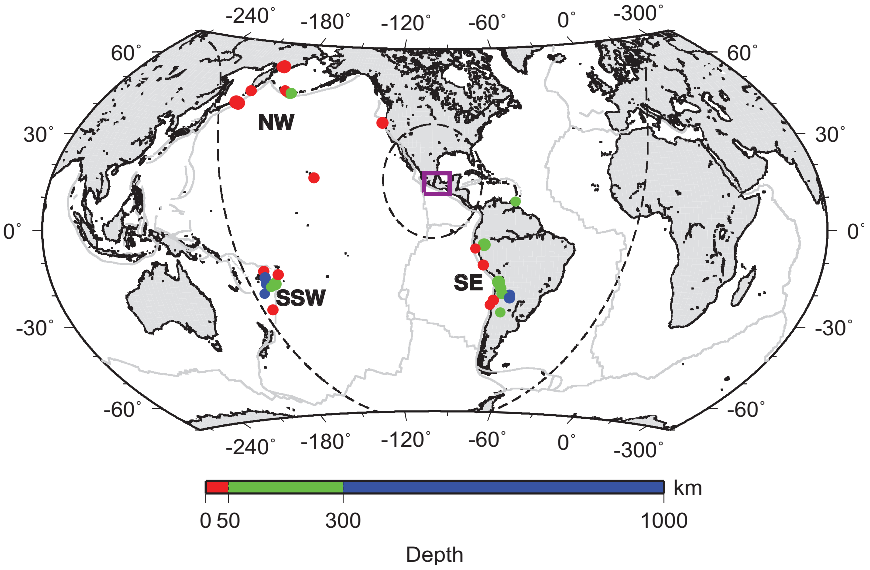

Figure 1.2: Distribution of teleseismic events used, including 12 events in a south-east (SE) back azimuth band from 139° to 145°, 9 events in a south-south-west (SSW) band from 238° to 250°, and 13 events in a north-west (NW) band from 317° to 330° from the station array enclosed in the box. Dashed lines are a distance of 30° and 90° away from Mexico City, the central point of the array. The events are colored according to depths.

and tangential coordinates. The data recorded over the TMVB, which laterally spans from 240 to 410 km from the Acapulco station, tends to be noisier than the other sites because of the cultural noise (six of the stations are in urban Mexico City), and scattering by the volcanic rocks.

The RFs from each back azimuth are separately stacked to give a better estimate of the averaged Moho depth beneath a station and show the azimuthal variations (*Yan and Clayton*, 2007). A total of 34 events span epicentral distances from 30° to 90°, which corresponds to ray parameters from 0.04 to 0.08 s/km. The data are selected if the signal-to-noise ratio is greater than a factor of 3 on the vertical component. Of the total 34 events, 12 events are selected within a SE back azimuth band from 139° to 145° from the MASE array; 9 events within a SSW band from 238° to 250°; and 13 events within a NW band from 317° to 330°.

1.2.2 Receiver Function Analysis

Standard RF processing enhances P-to-S converted phases by removing source complexities through the deconvolution of radial component seismograms by corresponding vertical components. Two types of deconvolution techniques are used in the analysis: (1) the frequency domain deconvolution (*Langston*, 1979; *Ammon et al.*, 1990); (2) the iterative time domain deconvolution technique (*Kikuchi and Kanamori*, 1982; *Ligorria and Ammon*, 1999). The major converted phases in the RFs are observed with both methods for data with high signal-to-noise ratio, but we find that the time domain deconvolution provides the highest resolution for sharply constraining the geometry of the slab and Moho above 100 km depth. The frequency domain deconvolution works better with low-frequency components, but it enhances the strength of the multiples. As an example, Figure 1.3 shows the vertical component seismograms along with the RFs using the time domain deconvolution. Figure 1.4 shows radial and tangential RFs for stations ATOT and VEGU (located in Figure 1.1), plotted according to the back azimuth. Note that the amplitude of tangential RFs is smaller by a factor of 2 compared to that of radial RFs. A detailed analysis of the tangential component is given by *Greene* (2009).

All the reflected/converted modes exhibit a distinct moveout as a function of source-receiver offset. By measuring these moveouts (assuming a locally flat layered structure), it is possible to estimate local depth and average Vp/Vs ratio between the surface and the discontinuity associated with each mode (*Zhu and Kanamori*, 2000). In practice, individual modes can be difficult to observe and identify on individual traces, so stacking many events at similar distances and back azimuths is employed, and a search is performed over a range of depths to the discontinuity and Vp/Vs ratios. Uncertainty estimates on the crustal thickness and the Vp/Vs ratio for the grid search algorithm are estimated from the 95% confidence interval. As an example of this stacking method, Figure 1.5 shows RF seismograms and the resulting stack, and the contour map of depth and Vp/Vs ratio for stations ATOT and PLAY (located in Figure 1.1).

RFs calculated at individual stations can be used to map out features such as Moho topography and slab structure across an array. Figure 1.6 shows the RF cross section obtained by evaluating the 21 March 2005 event recorded at stations from the Acapulco station to inland before the TMVB. The image shows the slab interface with a distinct negative (blue) pulse over a positive (red) pulse starting at 15 km depth at the Acapulco station. It dips down 15° to a point 80 km from the Acapulco

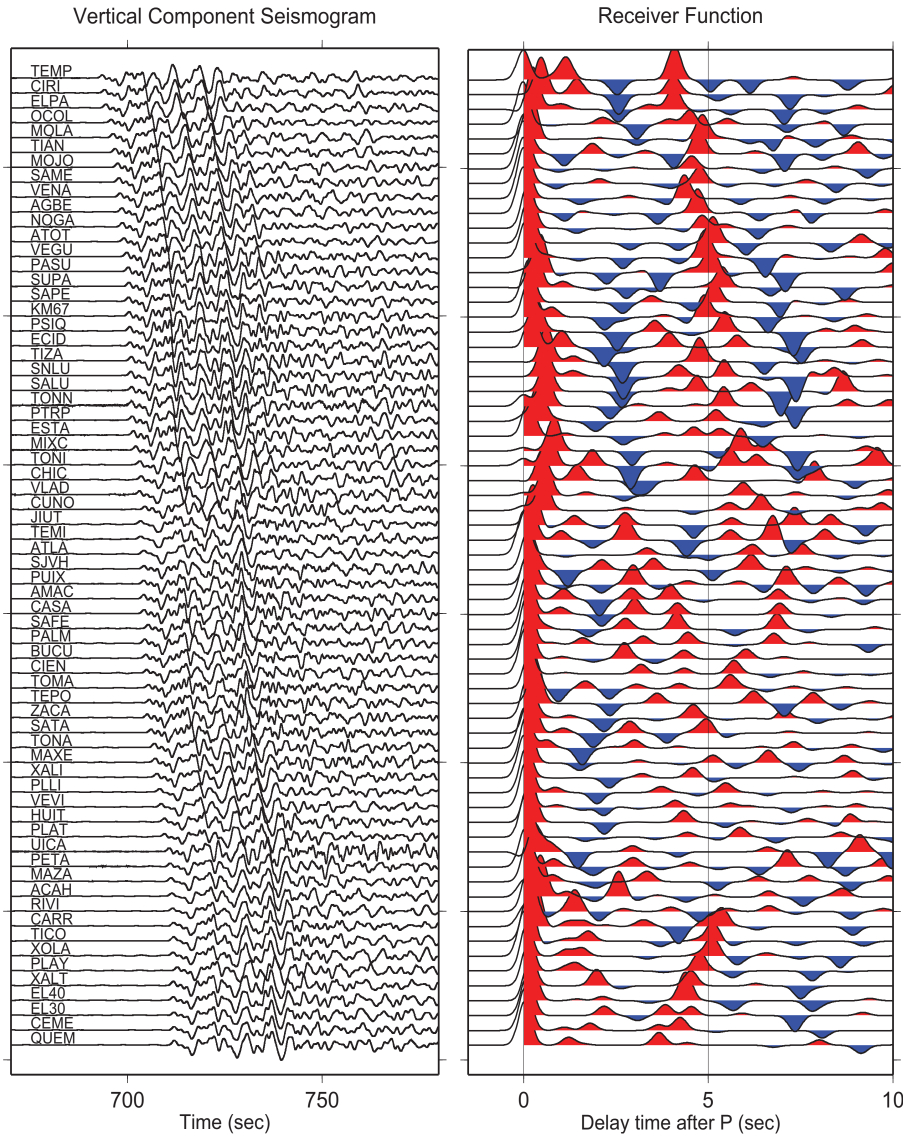

Figure 1.3: A record section of (left) the vertical component seismograms and (right) the corresponding RFs, obtained by processing the event on 20 April 2006 recorded from the MASE array. The seismograms and RFs are aligned in the order of increasing station latitude from bottom to top.

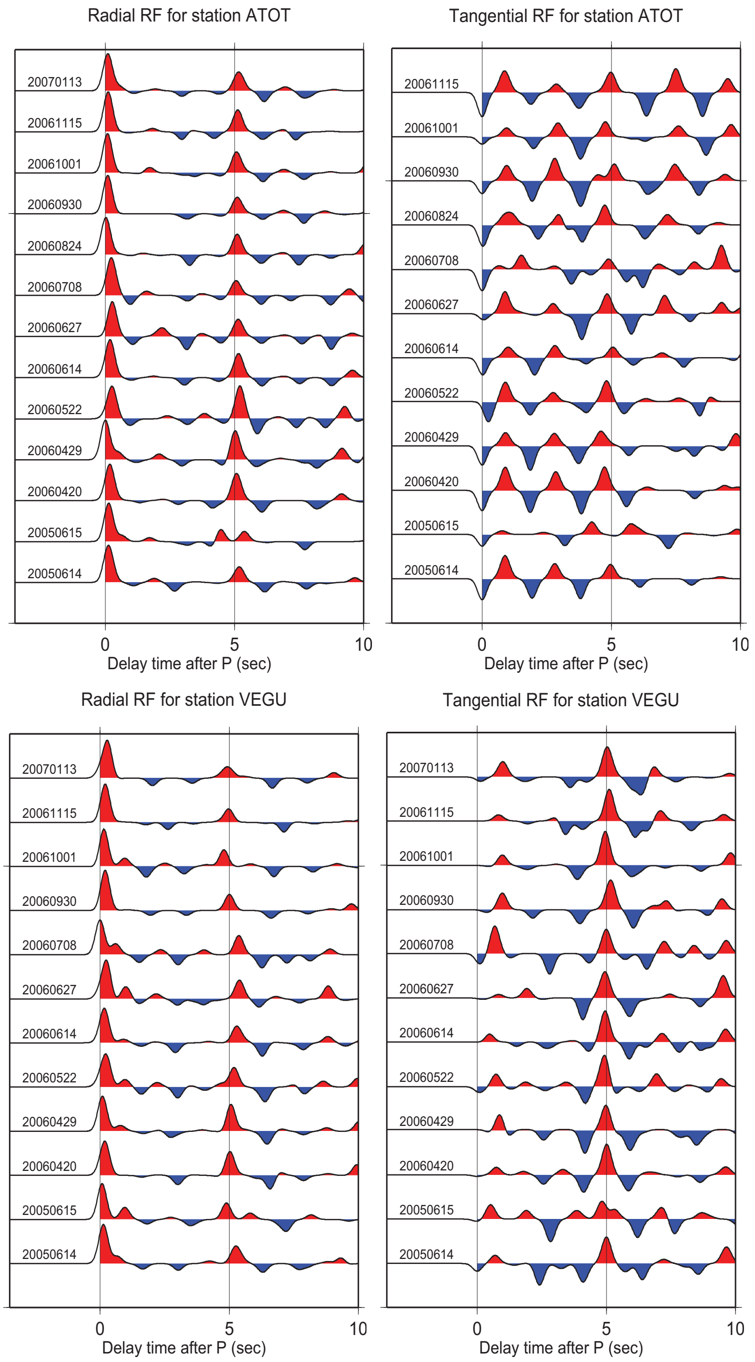

Figure 1.4: Radial and tangential RFs for station ATOT and VEGU. Each event date is indicated at the left of each trace. Ps conversion from Moho (the second largest peaks in radial RFs) arrives at 5 s for both stations. For comparison purposes, we boost amplitudes of the tangential RFs by a factor of 2.

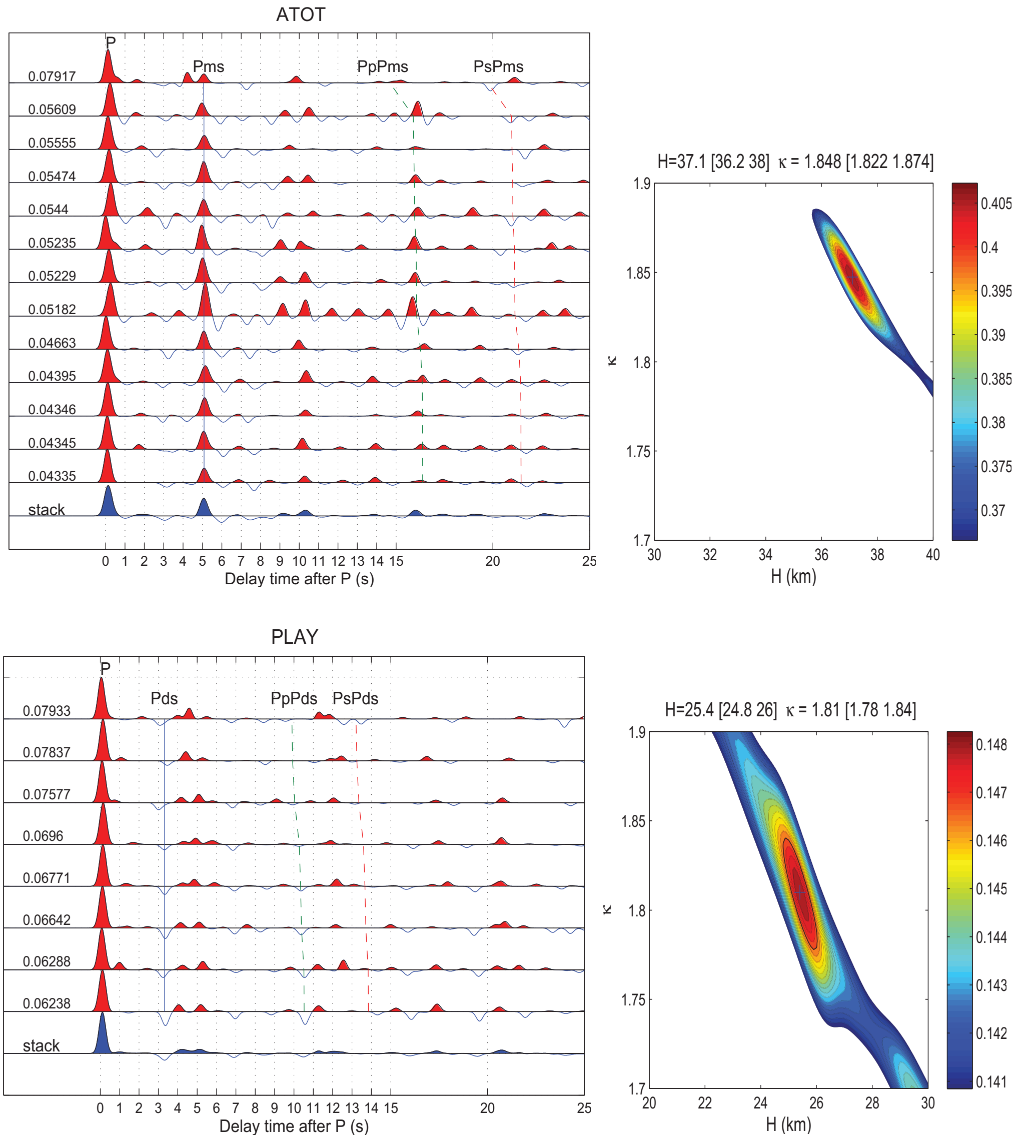

Figure 1.5: Crustal thickness (Moho, discontinuity depth H) and Vp/Vs ratio (κ) for stations (top) ATOT and (bottom) PLAY. (left) RF traces sorted according to the ray parameter indicated at the left of each RF trace. The predicted arrival times of the primary phase ((top) Pms and (bottom) Pds) and two multiples ((top) PpPms and PsPms, and (bottom) PpPds and PsPds) are marked by the solid and dashed lines. (right) Contour map of the weighted summation function (*Zhu and Kanamori*, 2000) for the discontinuity depth (H) and Vp/Vs ratio (κ). The black cross is the picked H and κ, which maximize the summation function, and the black line is the 95% confidence bound, which represents their uncertainty estimate.

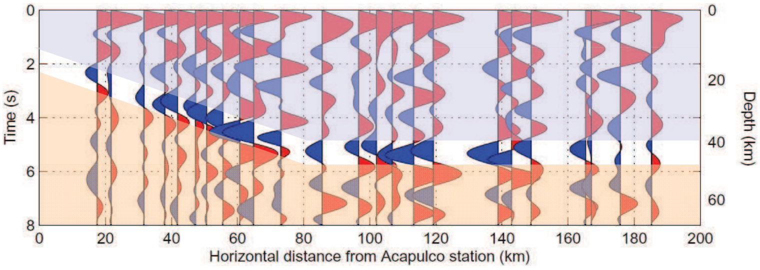

Figure 1.6: RF cross section showing the subducting Cocos plate using stations from Acapulco (~75 km from the trench) to the start of the TMVB. The single event that occurred on 21 March 2005 is processed by the frequency domain deconvolution. The blue, white, and orange overlays denote the continental crust, oceanic crust, and oceanic lithosphere, respectively.

station and then runs horizontally for 120 km. This horizontal section of the slab underplates the continental crust and ends just before the TMVB. The negative RF pulse indicates an existence of the low-velocity layer at the top part of the subducting oceanic crust. Details on this low-velocity layer are discussed in Sections 1.2.4 and 1.2.5.

Figure 1.7 shows a stacked RF cross section from each back azimuth event group recorded at all the stations. The stacked RF from each direction enhances different parts of the slab and Moho due to 3-D heterogeneities in the crust. For all three images in Figure 1.7, we observe the horizontal interface of the subducting Cocos plate indicated by the negative pulse followed by the oceanic Moho by the positive pulse after an initial dip of 15° at 5 to 6 s (~40 to 50 km in depth) and a lateral distance of 80 to 225 km from the Acapulco station. Furthermore, the RFs, especially from Acapulco to a point 100 km to the north in the continental crust, show horizontal layers of the negative and positive RF pulses (Figure 1.7). We determine the mechanism for the crust attenuation at the trench end of the slab to be undersided erosion by the slab and not uplift by the slab followed by surface erosion. The crustal thickness before the TMVB is 45 km on average, agreeing with the seismic refraction data and gravimetric studies (*Jordings et al.*, 2000; *Valdes-Gonzalez and Meyer*, 1996).

For all the back azimuth groups, the mid-section beneath the TMVB exhibits a relatively flat and strong Moho varying slowly in depth between 38 and 43 km (Figure 1.7). There is no apparent thickening of the crust under the TMVB. If the topography of the TMVB (2.2 km) were compensated by an Airy mechanism, one

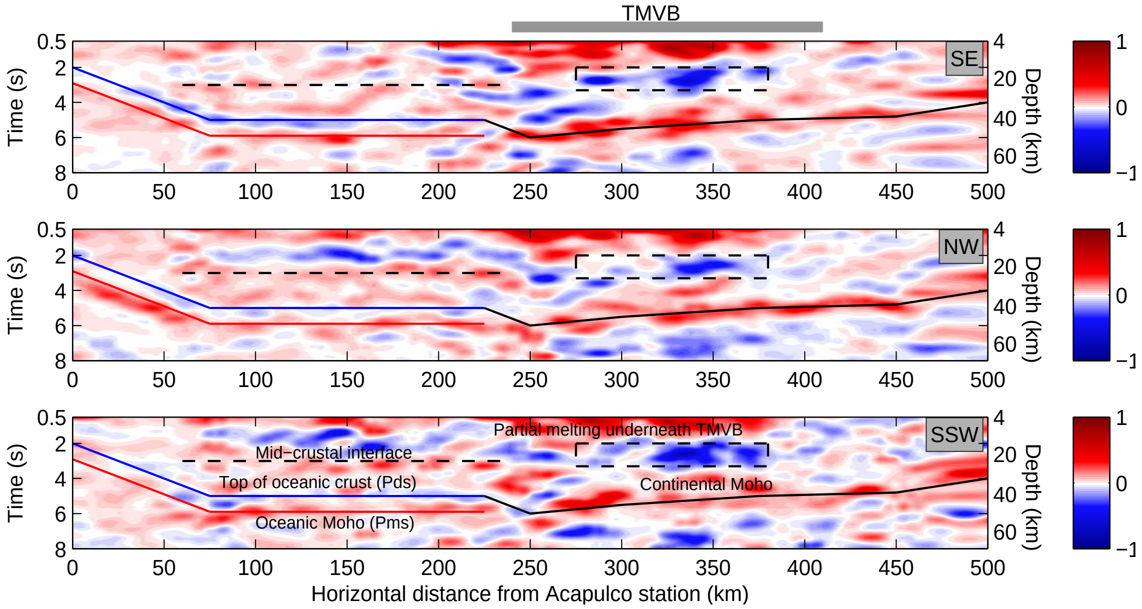

Figure 1.7: Stacked RF images for (top) SE, (middle) NW, and (bottom) SSW back azimuths. The RFs are computed by the iterative time domain deconvolution (*Kikuchi and Kanamori*, 1982; *Ligorria and Ammon*, 1999). Each image is created by assigning RF amplitudes into a separate output grid and filling the missing data by the linear interpolation. Note that the image is not sharply constrained from 450 to the end of the array (∼533 km) in the horizontal axis due to the data sparsely spaced at the northern section. The RFs in the SSW group are relatively noisier possibly due to the complications in the earthquake source and travel paths of seismic waves. Note that the P phase at zero seconds (the largest peak at the RF) is removed in the image to enhance the smaller signals after P. The color bar denotes the normalized RF amplitude.

would expect a root of approximately 13 km beneath it. Underneath the TMVB, a strong low-velocity zone is present at 3 s (∼25 km in depth) indicating partial melting features (Figure 1.7). This is in agreement with the shear wave velocity results presented by *Iglesias et al.* (2009) from surface wave studies. They propose that reduced velocities may correspond to reduced densities and hence provide a Pratt-type compensation method for the TMVB. High Vp/Vs ratio of 1.806 (Poisson's ratio of 0.279) is estimated for the TMVB, which may indicate an overall more mafic crustal composition (*Zandt and Ammon*, 1995). In addition, the crustal Vp/Vs ratios for the whole profile range from 1.65 to 1.898 with an overall average crustal Vp/Vs ratio of 1.79 (Poisson's ratio of 0.273). North of the TMVB, the crust thins from 35 to 25 km towards the end of the MASE array.

For all the back azimuth groups, the geometry of the slab plunging into the mantle underneath the TMVB is less well determined. The thick red P pulses in the TMVB are likely caused by resonances in basins such as the Valle of Mexico. Strong lateral velocity contrasts at the vicinity of the mantle wedge, including the oceanic plate projecting into the mantle, would further complicate the waveforms. P wave tomographic images provided by *Gorbatov and Fukao* (2005) and *Husker and Davis* (2009) showed that the slab is dipping 90° and 75°, respectively. The RF method is not capable of detecting such near-vertical structures (see Section 1.2.4 for details).

1.2.3 Receiver Function Imaging

The dense station spacing (6 km on average) is well suited for applying more accurate seismic migration techniques to teleseismic RF imaging. The method behind the inversion of the teleseismic waves and detailed discussion are given in *Bostock et al.* (2001). Here, we migrate the P-to-S converted phases (Pds, conversion from the top of the oceanic crust to the base of the continental crust, and Pms, conversion from the mantle to the bottom of the oceanic crust) using a Kirchhoff-style migration, which characterizes the output model as a grid of point scatterers. We assume that teleseismic P waves are arriving sufficiently far away that they can be approximated by plane waves. Traveltimes for the P-to-S converted waves are calculated by assuming that the ancident plane P wave converts to S wave energy at every possible scattering

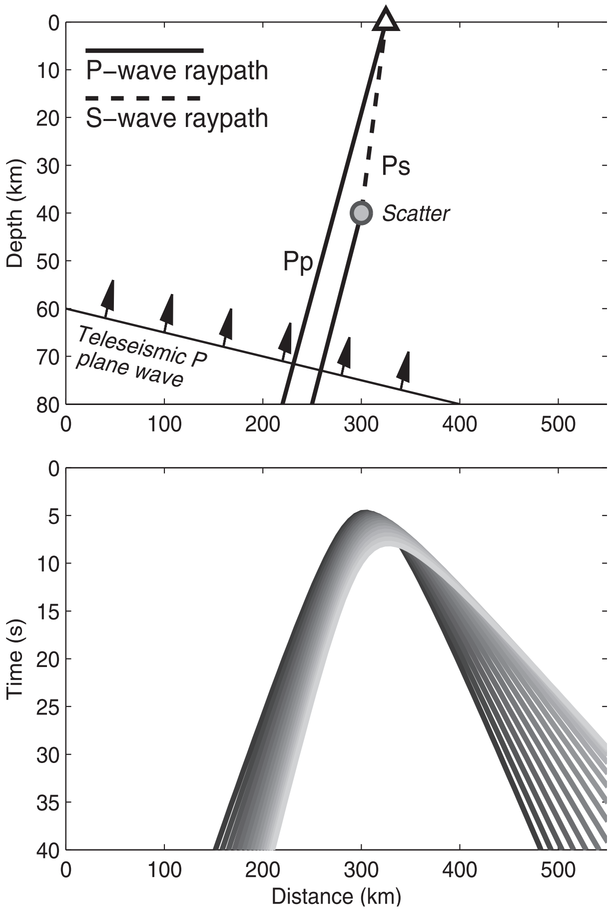

Figure 1.8: Schematic view showing (top) a plane wave that travels from below and converts into phases such as Pms and Pds at the scattering point and (bottom) the traveltime curve for Ps wave by varying the incidence angle of the plane wave and fixing the scattering point. For the traveltime calculation, the scattering point is fixed at (300 km, 40 km), and the P and S wave velocities are 6.3 and 3.6 km/s, respectively. The incident angle is varied from 10° to 80° in every 5°. Each line is shaded according to the incident angle, and its lighter color corresponds to larger incident angle.

point (see Figure 1.8, top). Figure 1.8 (bottom) shows the traveltime curves for the converted phase at one scattering point for varying incident angles of the plane wave. After determining the traveltimes of the converted wavefields at the scattering point, corresponding amplitudes are stacked to form an image. A similar procedure can be used for the multiples as was done by *Bostock et al.* (2002), but in our case the multiples are very weak, and do not contribute significantly to the image.

Figure 1.9 shows a migrated image from the direct P-to-S converted phases of all 34 teleseismic events. We use a simple layer velocity model to compute traveltimes for the converted wave according to the raypath geometries specified in Figure 1.8.

Several velocity sensitivity tests were performed to find that the energy is sharply focused when the average crustal P wave velocity is 6.3 km/s and S wave velocity 3.6 km/s. The dip and depth of the subducting oceanic crust and the oceanic Moho south of the TMVB as determined from the imaging are in good agreement with the RF images shown in Figure 1.7. The crustal interfaces at depths of 25 km and 30 km above the horizontal oceanic crust are observed. The continental Moho is clearly shown from the beginning of the TMVB to 450 km in lateral distance. The migration enhances the strength of the seismic multiples (PpP(d,m)s, PsP(d,m)s, and PpS(d,m)s).

The image beneath the TMVB shows that the slab plunges steeply (∼75°) in the mantle at 250 km from the Acapulco station, which agrees well with the tomography result provided by *Husker and Davis* (2009). The location of the steeply dipping slab can also be easily traced from the place where the depths of the seismic multiples abruptly change at 250 to 300 km in lateral distance (Figure 1.9). The positions of the multiples (PpPms, PsPms, and PpSms) are elevated when transitioning from the oceanic Moho to the continental Moho (Figure 1.9). The dip of the slab is more apparent in the migrated image despite the noisy RFs from the TMVB.

1.2.4 Receiver Function Finite-Difference Modeling

To further investigate the images, we produce synthetic RFs with a 2-D finite-difference wave propagation program for particular velocity and slab geometry models and compare these to the data. The laterally complicated structure (continental crust, oceanic crust, and mantle before the TMVB and continental crust, mantle wedge, oceanic crust, and mantle underneath and north of the TMVB), leads to very complicated images containing Pds and Pms phases, and their seismic multiples. The FD modeling helps verify several seismic phases due to the complicated structure present underneath the MASE array. In this section, we show one velocity model to represent our horizontal oceanic crust before the TMVB.

On the basis of our observations in Sections 1.2.2 and 1.2.3, the model consists of an average crust of 45 km, an oceanic crust, which runs horizontally for 145 km, and a mantle zone (see the P wave model in Figure 1.10). Delays between the direct

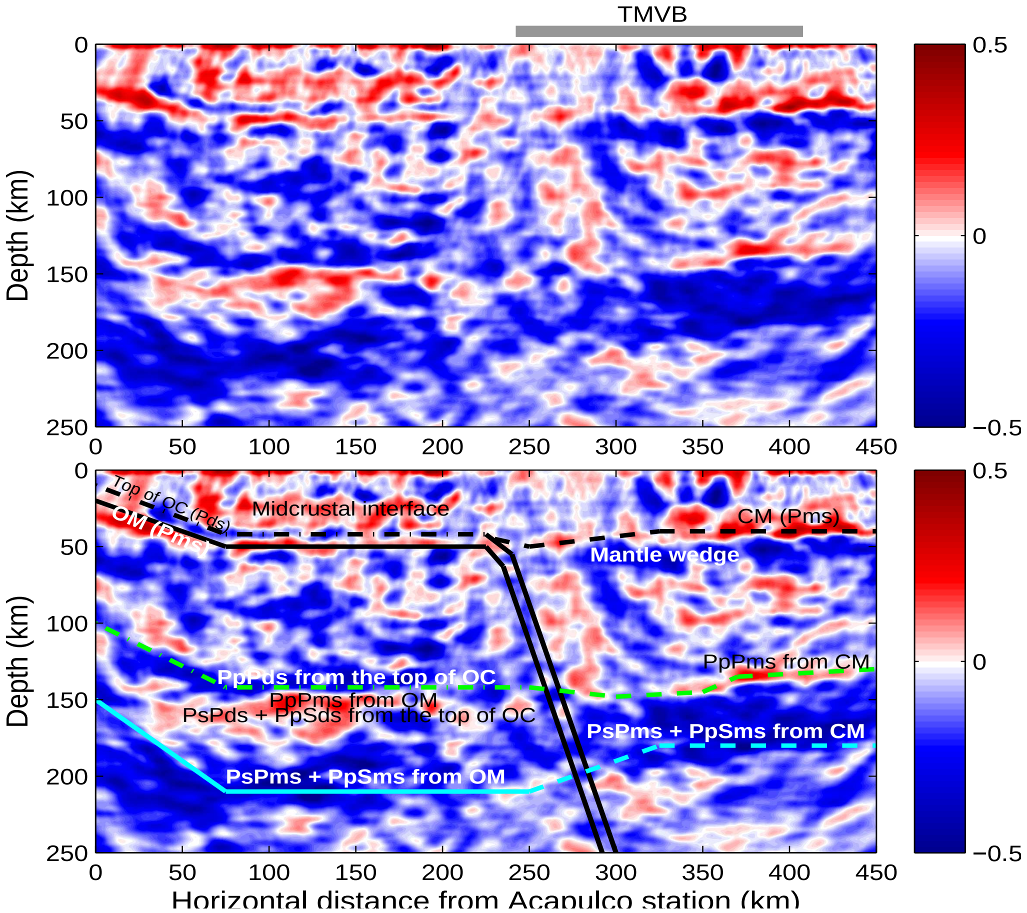

Figure 1.9: Migrated image of (top) uninterpreted display and (bottom) interpreted display using Pms and Pds phases, showing the steeply dipping oceanic crust at about 75° underneath the TMVB. The dash-dotted lines indicate the top of the subducting oceanic crust characterized by the very low-velocity. The dashed line incidates the continental Moho, which extends from TMVB to the coast near Gulf of Mexico. Seismic multiples from oceanic Moho (OM) and continental Moho (CM) as well as the subhorizontal oceanic crust are shown clearly in the image. Note that the green (dash-dotted and dashed) lines are the multiples from the crustal interface (Pds and Pms), and the cyan (solid and dashed) lines the multiples from the oceanic and continental Moho. Subducting Cocos plate is located by changes in the depth of the seismic multiple changes. Note that the image does not include the section from 450 to the end of the array (∼533 km) in the horizontal axis because the data are sparsely spaced at the northern section. The color bar denotes the normalized RF amplitude.

and converted wave are proportional to the depth of the interface and depend on the transmission velocities along their paths, while the amplitude of the converted arrival depends on the magnitude and sign of the velocity contrast. Thus, the thickness and the RF amplitude peak-to-peak height of the oceanic crust are used as additional constraints to construct the model. To match the negative (blue) and positive (red) RF pulses at 5 and 6 s, respectively, from Figure 1.6, the oceanic crust should be characterized as a low-velocity layer above the mantle. However, a single layer cannot reproduce the amplitudes of the positive and negative pulses, so it is further divided into two low-velocity layers to achieve a comparable (but opposite in polarity) velocity contrast that we see from the 1 s RF data (Figure 1.6). The additional low-velocity zone (denoted hereafter as the upper oceanic crust) includes velocities much lower than normal oceanic crustal velocities (of the lower oceanic crust). *Song et al.* (2009) also inserted the ultraslow velocity layer (S wave velocity of 2.0 to 2.7 km/s) over the low-velocity layer in their model to reproduce the converted SP arrivals and teleseismic underside reflections from the top of the subducting plate. In the P and S wave velocity model (Figure 1.10), the upper oceanic crust has a thickness of 3 km, a P wave velocity of 5.54 km/s, and an S wave velocity of 2.6 km/s; the lower oceanic crust a thickness of 5 km, a P wave velocity of 6.98 km/s, and an S wave velocity of 4.06 km/s. Plane waves with variable ray parameters in the range of 0.04 to 0.08 are then entered as boundary conditions on the left bottom corner of our constructed model. Iterative time domain deconvolution (*Kikuchi and Kanamori*, 1982; *Ligorria and Ammon*, 1999) is used to convert the synthetic seismograms to the radial RFs (Figure 1.10).

Figure 1.11 shows the result of a dip sensitivity test. We vary the dip from shallow to steep angles (10°, 25°, 50°, and 75°), using the same velocity model specified in Figure 1.10, and observe how the RF image reproduces the dipping slab. When the dip angle exceeds 50°, the polarity of the synthetic RFs changes sign, in agreement with the change in sign of the transmission coefficient. This explains why we do not see a clear image of the slab descending into the mantle in 75° from Figure 1.7. The effect of the sign change is not included in the migrated image (Figure 1.9).

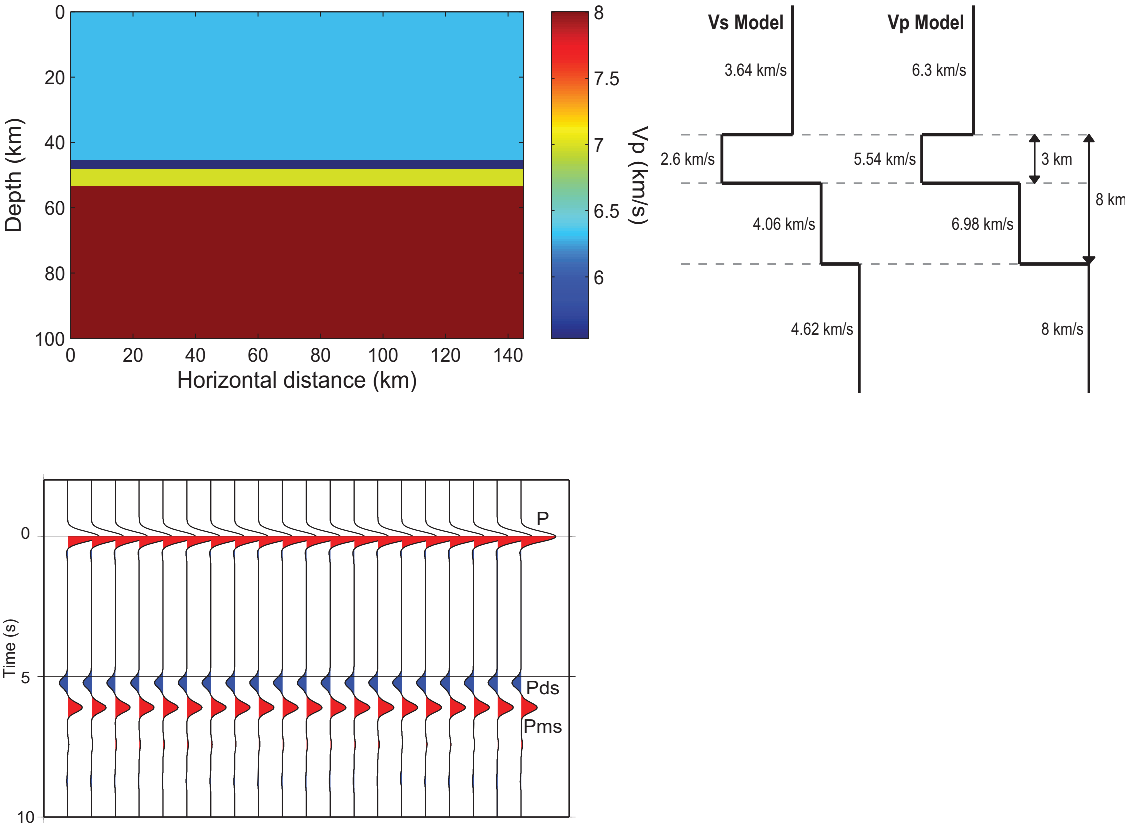

Figure 1.10: (top left) P wave velocity model, (top right) P and S wave velocity models, and (bottom) corresponding synthetic RFs for the subhorizontal part of the Cocos plate subduction south of the TMVB.

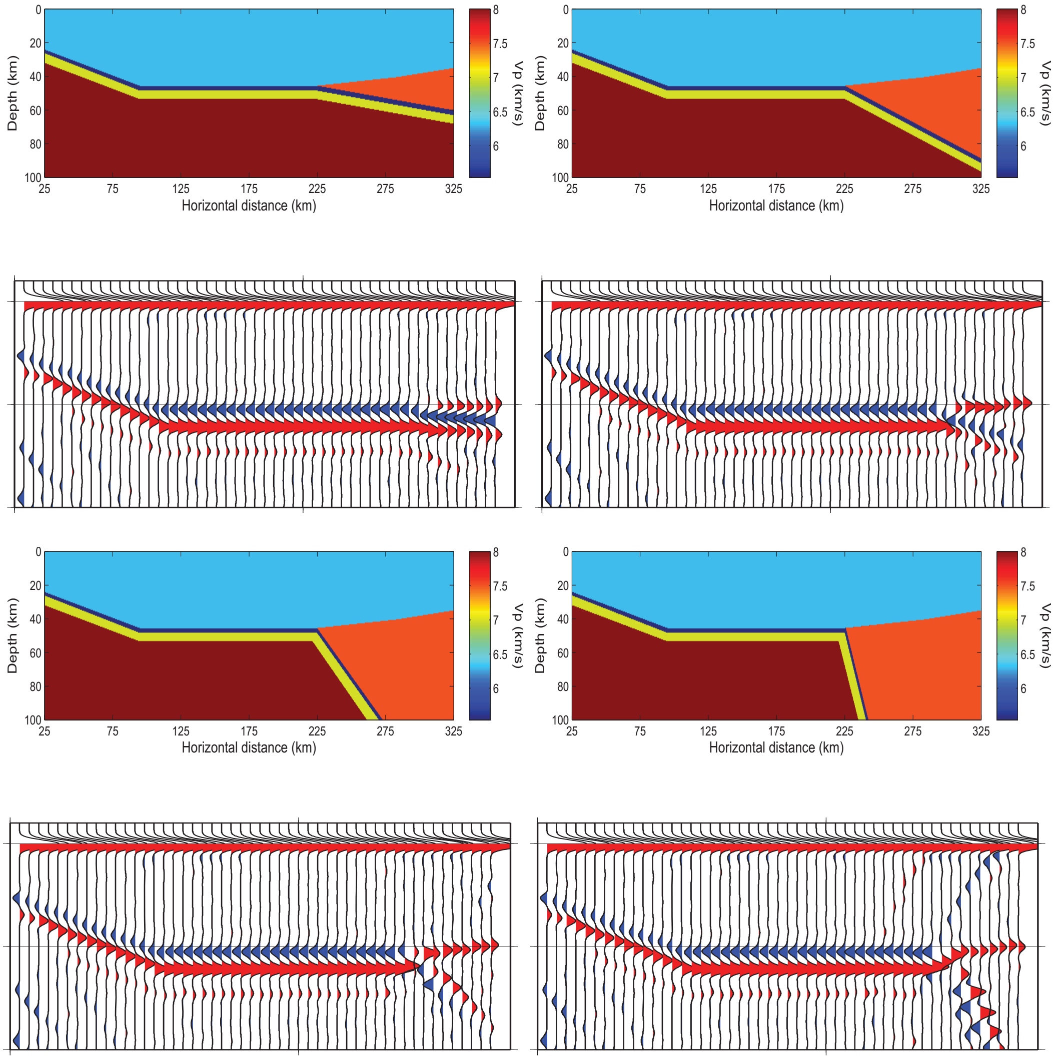

Figure 1.11: Dip sensitivity test results using 2-D finite-difference modeling to demonstrate that RFs at steeper angles do not work. The dip angles vary from 10°, 25°, 50°, and 75°. Note that the polarity of the synthetic RFs changes the sign when the dip angle exceeds 50°. Also, the diffraction artifact from a sharp corner appears to be strong in the overlying crust.

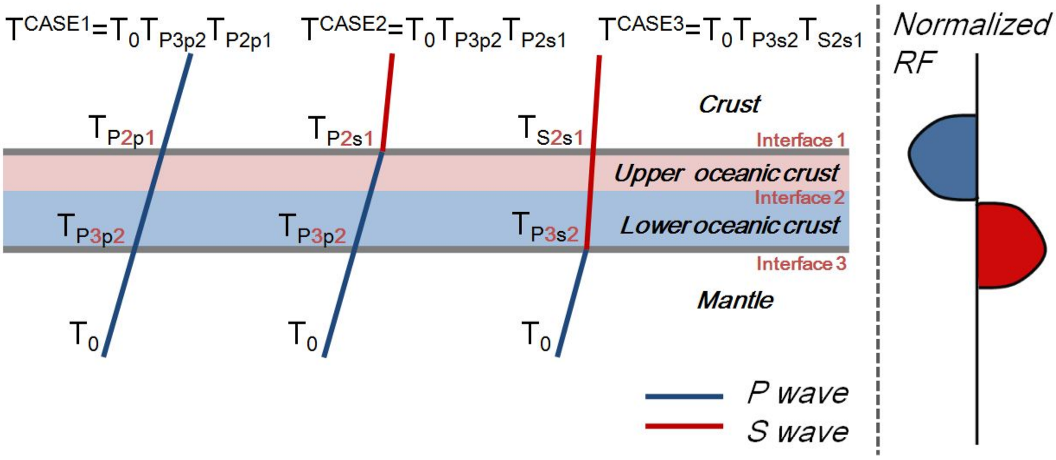

Figure 1.12: Schematic showing transmitted responses at top and bottom interfaces of the oceanic crust. The RF responses responses are normalized by the P arrival. The peak of the negative RF pulse is obtained at the interface 1 between the crust and the upper oceanic crust; the peak of the positive RF pulse at the interface 3 between the lower oceanic crust and the mantle.

1.2.5 Inversion of Receiver Function Amplitudes

The FD modeling result in Section 1.2.4 reveals that very-low P and S wave velocity layer is necessary to reproduce a strong negative impedance contrast seen at the top of the subducting oceanic crust in our 1 s RF data set. To further investigate the nature of our upper and lower oceanic crust, we develop a technique based on plane wave conversion to invert the seismic parameters such as impedance (a product of S wave velocity and density). The method utilizes the RF amplitude information of the P-to-S converted phases (Pds and Pms) in the four-layer model (crust, upper and lower oceanic crust, and mantle), and leads to an estimation of the seismic properties of the upper and lower oceanic crust.

We obtain three different cases when the P wave is transmitted as a P or S wave at the top and bottom of the oceanic crust as shown in Figure 1.12. Case 1 is when there is no conversion; case 2 is when the P wave is converted into S wave at the top of the (upper) oceanic crust; and case 3 is when the P wave is converted into S wave at the bottom of the (lower) oceanic crust. By denoting the transmission coefficient at the interface as T for simplicity, we can express the transmission coefficient for each case as

$$T^{CASE1} = T_0 T_{P3p2} T_{P2p1}, \tag{1.1}$$

$$T^{CASE2} = T_0 T_{P3p2} T_{P2s1}, \tag{1.2}$$

$$T^{CASE3} = T_0 T_{P3s2} T_{S2s1}, \tag{1.3}$$

where T_0 denotes the amplitude arriving at the bottom of the layer, and the subscript indicates the travel path of converted P or S wave at each interface, numbered as 3 (mantle to lower oceanic crust), 2 (lower oceanic crust to upper oceanic crust), and 1 (upper oceanic crust to crust). To obtain the transmission response at the top and bottom of the oceanic crust, we divide the transmission coefficients for the case 2 and 3 by the case 1:

$$\frac{T^{CASE2}}{T^{CASE1}} = \frac{T_0 T_{P3p2} T_{P2s1}}{T_0 T_{P3p2} T_{P2p1}} = \frac{T_{P2s1}}{T_{P2p1}} \sim T_{P2s1} \tag{1.4}$$

$$\frac{T^{CASE3}}{T^{CASE1}} = \frac{T_0 T_{P3s2} T_{S2s1}}{T_0 T_{P3p2} T_{P2p1}} = \frac{T_{P3s2} T_{S2s1}}{T_{P3p2} T_{P2p1}} \sim T_{P3s2}, \tag{1.5}$$

where T^{CASE1} is the transmitted response for P wave with no conversion at each interface. T_{P2s1} from equation (1.4) directly relates to the amplitude of negative RF pulse; T_{P3s2} from equation (1.5) is that of positive RF pulse, shown in Figure 1.12.

In the inversion, we use the linearized Zoeppritz equation, which describes the elastic, plane wave reflection and transmission coefficients between two half-spaces (*Aki and Richards*, 2002) for small incidence angles. The P-to-S transmission coefficient depends only on the S wave velocity and density variations,

$$T^{PS} = \frac{p\alpha}{2\cos j}\left[\left(1 - 2\beta^2 p^2 - 2\beta^2 \frac{\cos i}{\alpha}\frac{\cos j}{\beta}\right)\frac{\Delta\rho}{\rho} - 4\beta^2\left(p^2 + \frac{\cos i}{\alpha}\frac{\cos j}{\beta}\right)\frac{\Delta\beta}{\beta}\right], \tag{1.6}$$

where p represents the ray parameter, α the P wave velocity, β the S wave velocity, ρ the density, and i and j the incident and transmitted angle, respectively. Assuming the small angle approximation (thus $p^2 \rightarrow 0$), equation (1.6) is reduced as follows:

$$T^{PS} = \frac{p\alpha}{2}\left[\left(1 - \frac{2\beta}{\alpha}\right)\frac{\Delta\rho}{\rho} - \frac{4\beta}{\alpha}\frac{\Delta\beta}{\beta}\right]. \tag{1.7}$$

The approximation is valid for small angles, which is suitable for conversions along the portion of the oceanic crust before the TMVB. In the inversion, we prescribe seismic parameters (α (or Vp), β (or Vs), and ρ) for the crust and mantle, and the P wave velocity of the upper and lower oceanic crust. Finally, we use least squares inversion to obtain the impedance (a product of S wave velocity and density) for the upper and lower oceanic crust. The data set for the inversion are the measured amplitude height of the negative and positive RF pulses normalized by the P wave pulse arriving at 0 s. In addition, the separation in time is used to invert for the thickness of the oceanic crust.

We note that the inversion is mainly sensitive to the shear-wave velocity variations and not density variations, and consequently S wave velocity and density are highly correlated to each other. The impedance values at the upper and lower oceanic crust are not correlated to each other (see Figure 1.13, bottom). The S wave velocity is, however, still useful because a product of separately inverted S wave velocity and density is consistent with the inverted impedance for the upper and lower oceanic crust as shown in Figure 1.13. Density variations along the array are moderate (2600−2750 kg/m^3 in the upper oceanic crust; 3125−3275 kg/m^3 in the lower oceanic crust). The inverted S wave velocity is extremely low and highly variable (2.4−3.4 km/s in the upper oceanic crust; 3.6−4.2 km/s in the lower oceanic crust). This S wave velocity is later used to compute Vp/Vs and Poisson's ratios with prescribed P wave velocities for the upper and lower oceanic crust. Since the Vp/Vs ratio strongly depends on the mean rheology of the oceanic crust, we use a range of P wave velocities for the oceanic crust that would give reasonable ratios. We did not attempt to independently measure the P wave velocity in the layer with multiples (*Audet et al.*, 2009) because they are very weak in the raw data.

We further test and refine this set of P wave velocities by plotting the Vp/Vs ratio versus S wave velocity at a depth of 35 km and a range of likely temperatures at this depth for the candidate low-pressure hydrated phases in Figure 1.14. The mineral properties were calculated using finite strain theory (*Duffy and Anderson*, 1989) and recently reported velocities (*Pawley et al.*, 1995; *Bailey and Holloway*, 2000; *Reynard et al.*, 2007; *Mainprice et al.*, 2008; *Sanchez-Valle et al.*, 2008). Data points corresponding to the upper oceanic crust are highly varying in the Vp/Vs versus Vs domain (average Vp/Vs of 1.85) whereas those to the lower oceanic crust are tightly bounded (average of 1.72). The uncertainty range, specified in Figure 1.14, is set such that the average of the data points for the upper oceanic crust lies between the Vp/Vs ratios of 1.8 and 1.9, and that for the lower oceanic crust between 1.7 and

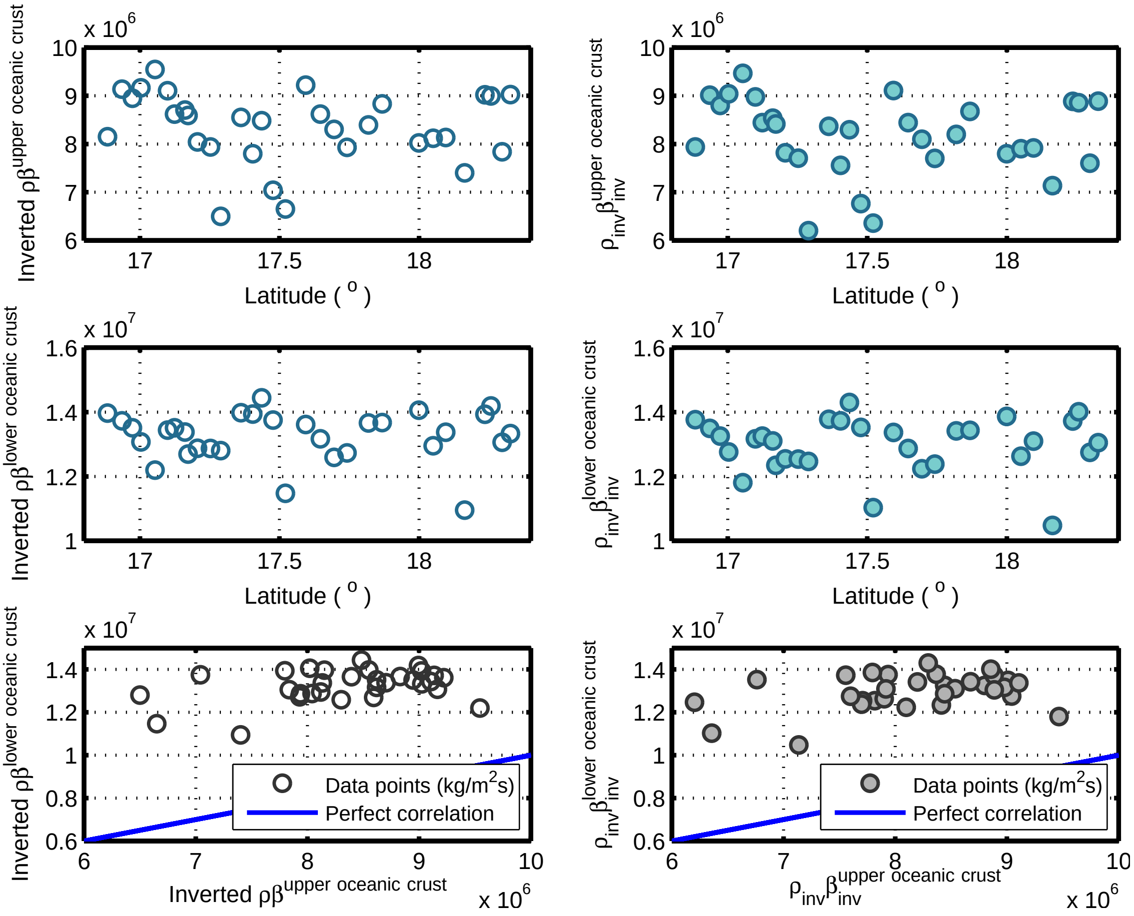

Figure 1.13: Comparison between (left) the inverted impedance and (right) the product of inverted S wave velocity and density for the upper and lower oceanic crust. (bottom) Linear correlation plots showing that the impedance for the upper oceanic crust and that for the lower oceanic crust are not correlated.

1.74. Corresponding P wave velocity for the upper oceanic crust lies between 5.387 and 5.689 km/s (data points are plotted in Figure 1.14 when Vp = 5.537 km/s), and that for the lower oceanic crust lies between 6.898 and 7.06 km/s (data points are plotted in Figure 1.14 when Vp = 6.979 km/s).

The data points for the upper oceanic crust are highly depth dependent and lie in between data obtained for preferentially oriented talc (*Bailey and Holloway*, 2000) and randomly oriented talc phases (*Mainprice et al.*, 2008) (Figure 1.14). The shallow depth (near the Pacific coast) corresponds to the lower Vp/Vs and Poisson's ratios (higher Vs), and the deeper depth of the subhorizontal part of the oceanic crust corresponds to the higher Vp/Vs and Poisson's ratios (lower Vs) (Figure 1.14). On the other hand, the data points for the lower oceanic crust lie close to hydrous phases like antigorite and lizardite. Gabbro is also capable of explaining the lower oceanic crust data. High-pressure hydrous phases, like Fe-bearing phase A and depleted mantle rocks, like pyroxenite and harzburgite, are characterized by higher Vs values than what we observe. This may imply that lower oceanic crust is unaltered one over the dry-depleted mantle rock.

Inverted impedance (normalized by the maximum impedance) for all the off-axis piercing points is shown as a 2-D strip of variations along the array (Figure 1.15). The Vp/Vs and Poisson's ratios are plotted in a similar fashion to show the lateral variability for the upper and lower oceanic crust in a map view (Figure 1.16 and 1.17). In general, variably low impedance as well as highly variable Vp/Vs and Poisson's ratios (both due to extremely low S wave velocity) are observed at the flat part of the upper oceanic crust. On the other hand, the lateral variability of each seismic parameter is minimal along the array in the lower oceanic crust. The average impedance for the lower oceanic crust is computed to be 1.3172x10^7 kg/m^2/s.

The time separation of the two converted phases is used to invert for the thickness of the oceanic crust. Figure 1.18 shows the thickness of the continental crust, oceanic crust and oceanic Moho. The thickness of the crust and oceanic Moho agree well with our observation of shallow-to-horizontal interfaces shown in Figures 1.6 and 1.7. The thickness of the oceanic crust becomes gradually thicker as the slab dips at a shallow angle, and it becomes almost constant (1 or 2 km thinner away from the coast).

We can further explore our data set to compute for the thickness of the upper and

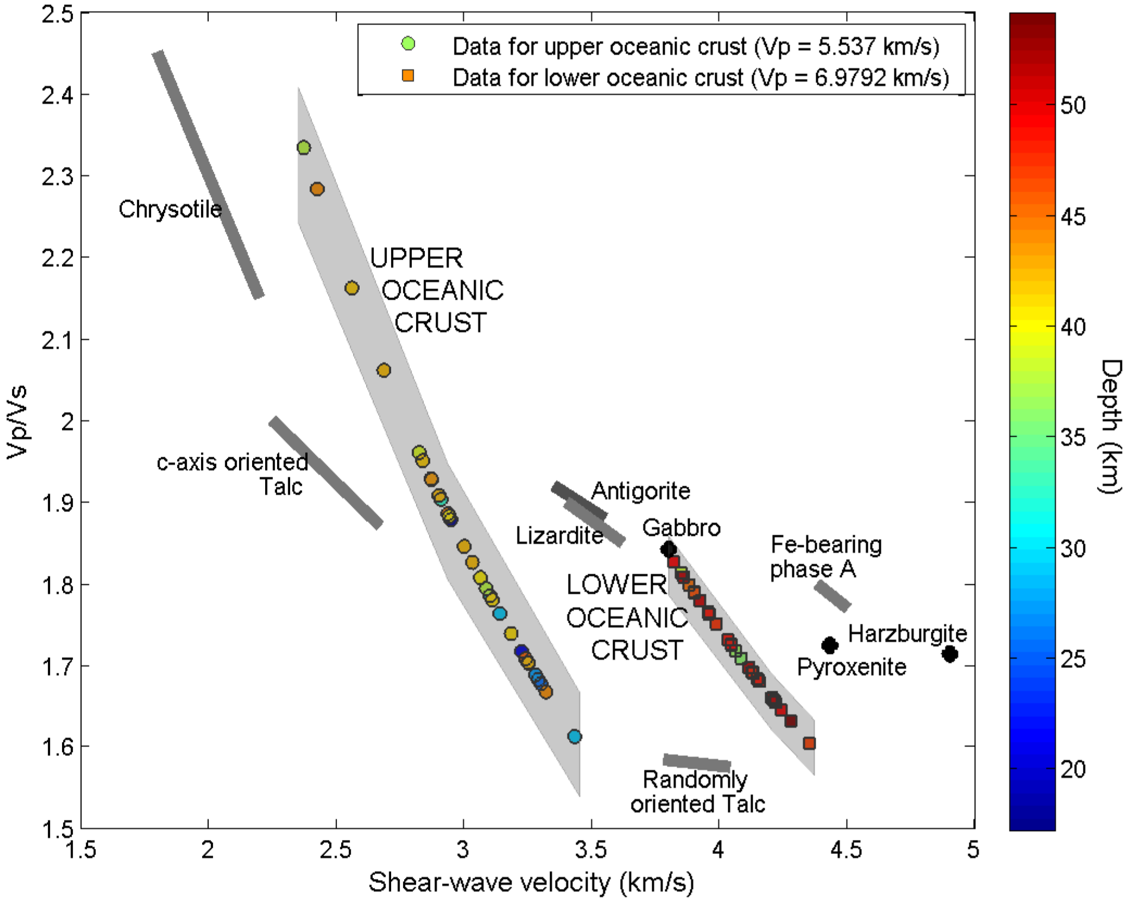

Figure 1.14: Calculated Vp/Vs ratio versus S wave velocity (Vs) at a depth of 35 km and a range of likely temperatures (500−800°C) at this depth for candidate hydrated phases (gray lines) and rock types (black diamonds). The points for randomly oriented talc and c axis oriented talc are from *Mainprice et al.* (2008), and those for different rock types from *Christensen and Salisbury* (1975). The data points for the upper oceanic crust are highly varying in Vp/Vs and Vs domain (average Vp/Vs of 1.85) and lie close to talc phases, whereas those for the lower oceanic crust are tightly bounded (average of 1.72). The light-gray shaded regions denote uncertainties due to the choice of Vp. The lower bound of the uncertainty for the upper oceanic crust is computed when Vp = 5.387 km/s, and the upper bound is when Vp = 5.689 km/s. The lower bound of the uncertainty for the lower oceanic crust is computed when Vp = 6.898 km/s, and the upper bound is when Vp = 7.06 km/s.

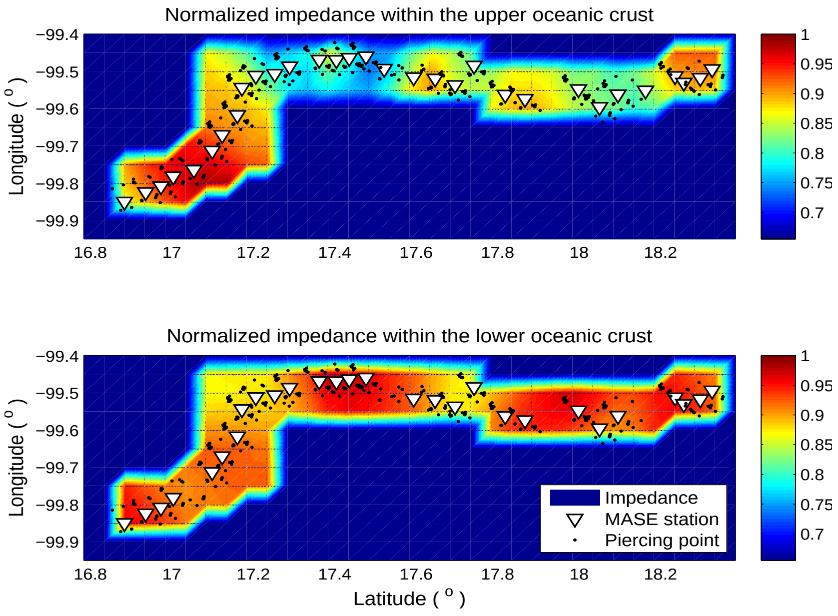

Figure 1.15: Variations in the (normalized) impedance within upper and lower oceanic crust along the MASE array south of the TMVB. The flat part of the oceanic crust starts at latitude of 17.2°. Each plot is generated using the nearest-neighbor interpolation scheme.

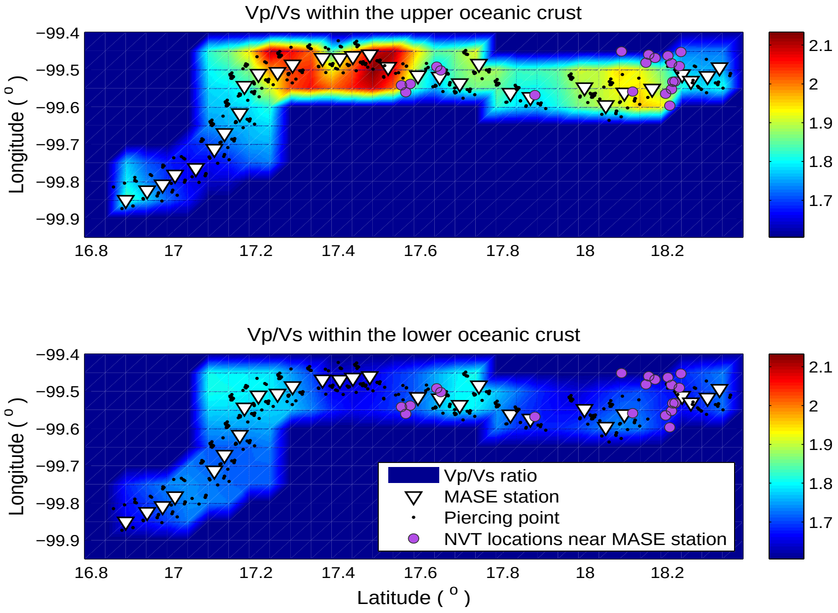

Figure 1.16: Variations in the Vp/Vs ratio within upper and lower oceanic crust along the MASE array south of the TMVB. The flat part of the oceanic crust starts at latitude of 17.2°. Each plot is generated using the nearest-neighbor interpolation scheme. The NVT locations that are located on a near the slab interface near the MASE stations are shown as purple circles.

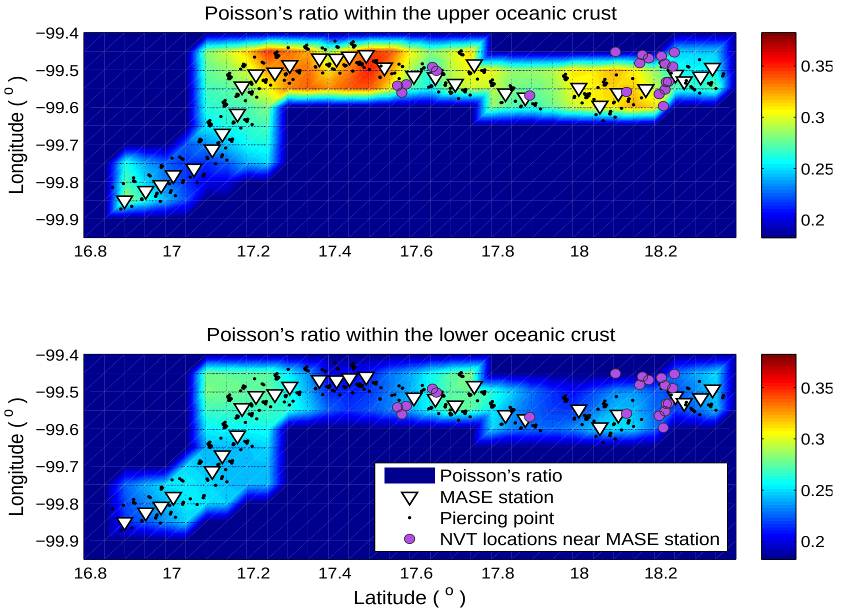

Figure 1.17: Variations in the Poisson's ratio within upper and lower oceanic crust along the MASE array south of the TMVB. The flat part of the oceanic crust starts at latitude of 17.2°. Each plot is generated using the nearest-neighbor interpolation scheme. The NVT locations that are located on a near the slab interface near the MASE stations are shown as purple circles.

lower oceanic crust by using the FD modeling. In the modeling, we fix the thickness of the oceanic crust (8 km) and the seismic parameters (Vp, Vs, and ρ) for the lower oceanic crust because it is suggested to be generally homogeneous in composition as shown in Figure 1.14. We only vary the parameters (Vs, ρ, and thickness) for the upper oceanic crust, keeping the impedance the same as the previously inverted impedance. Figure 1.19 shows three P and S wave velocity models that would produce RF pulses with almost equal amplitude height corresponding to Pms and Pds phases. The thickness of the upper oceanic crust needs to be thicker as the S wave velocity increases: 3 km for the S wave velocity of 2.6 km/s, 4 km for 2.7 km/s, and 5 km for 2.8 km/s.

Figure 1.20 shows our final model showing lateral variations in the seismic parameters (Vp/Vs and Poisson's ratios) with inverted thickness of the oceanic crust in a depth cross section. The thickness of the upper oceanic crust is set to 3 km from our FD modeling and inversion (Figure 1.10 and 1.19). The nonvolcanic tremor (NVT), specified in red squares, mostly occurs in the continental crust (5−40km depth) with a few events localized on the horizontal plate interface or in the subducted plate crust

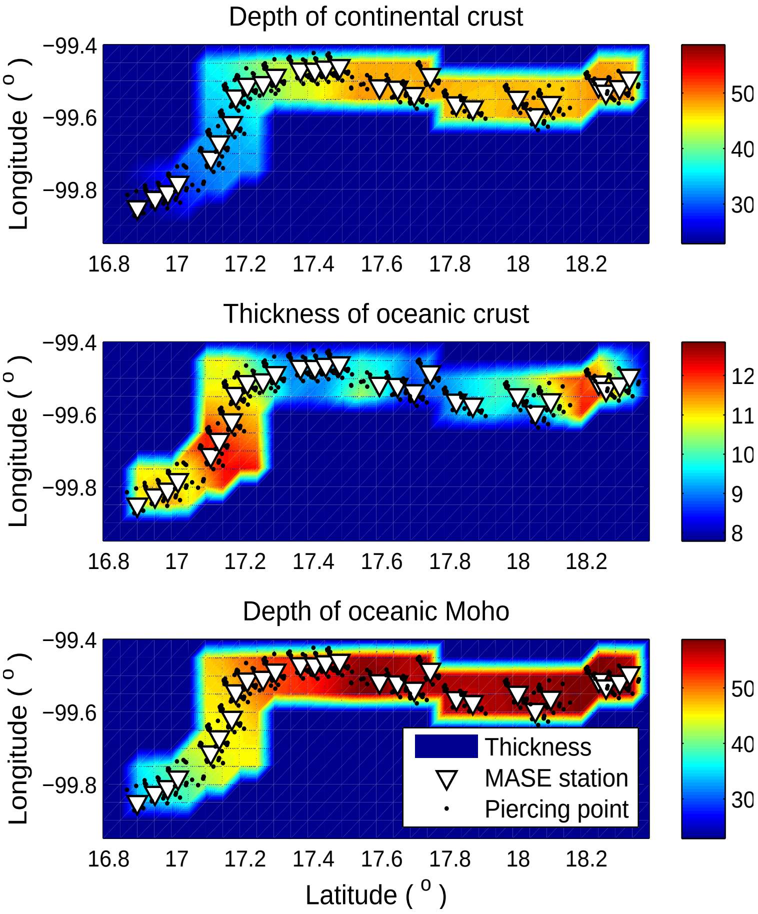

Figure 1.18: Thickness of the continental crust, oceanic crust, and oceanic Moho. We invert for the thickness of the continental crust and the oceanic crust by measuring the time difference between two RF pulses corresponding to Pds and Pms phases. Note that the thickness of the oceanic crust becomes gradually thicker as the slab dips at a shallow angle, and it becomes almost constant and 2 or 3 km thinner in the flat slab region (after the latitude of 17.2°). The slab thickens before it plunges into the mantle. Each plot is generated using the nearest-neighbor interpolation scheme.

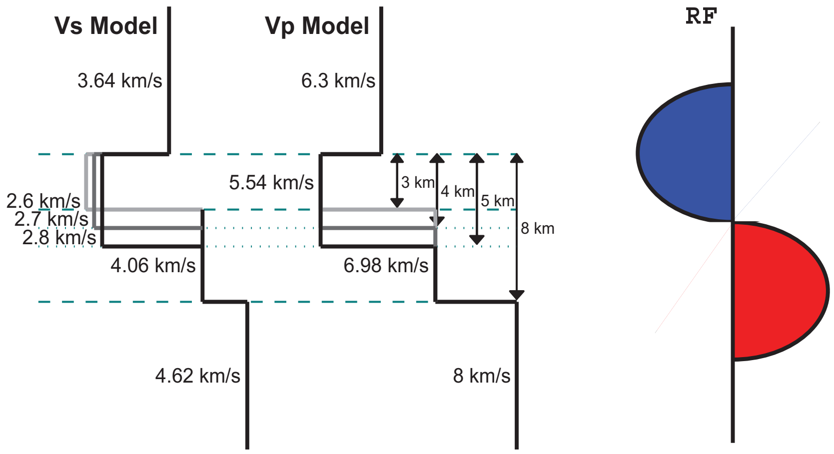

Figure 1.19: Velocity models that produce RF pulses with the equal amplitude height and opposite polarity corresponding to Pms and Pds phases. In the FD modeling, we only vary the S wave velocity, density, and thickness of the upper oceanic crust.

(*Payero et al.*, 2008). The slow slip events (SSEs) that occurred in 2006 coincide with our study area from Acapulco to a point 100 km to the north (*Larson et al.*, 2007).

1.3 Discussion

The flat slab regions occur in 10% of modern convergent margins and have been studied in several places in the world (central Chile, Peru, SW Japan, etc.) (*Gutscher et al.*, 2000). It is proposed that the flat subduction in most of places was formed primarily by the buoyancy of thickened oceanic crust and a delay in the basalt to eclogite transition due to the cool thermal structure of the overlying plate (*Gutscher et al.*, 2000). Other proposals are plate velocity (*Lallemand et al.*, 2005), resistance to plate bending (*Schellart et al.*, 2007; *Schellart*, 2008), topographic asperities (*Gutscher*, 2002), and symmetry (*Gephart*, 1994). It has also been suggested that there might be a direct relationship between flat slab subduction and silica enrichment in the continental lithosphere (*Wagner et al.*, 2008). Of the flat subduction regions, the subduction system in central Mexico is unique in the sense that the horizontal oceanic crust with normal crustal thickness is situated at a very shallow depth (~40 km) and the asthenosphere is absent (*Pérez-Campos et al.*, 2008). Our RF analysis shows the oceanic crust is subducting in a shallow (15°) to horizontal dip, extending to 250 km from the MAT, and underneath the TMVB descending into the mantle at a very

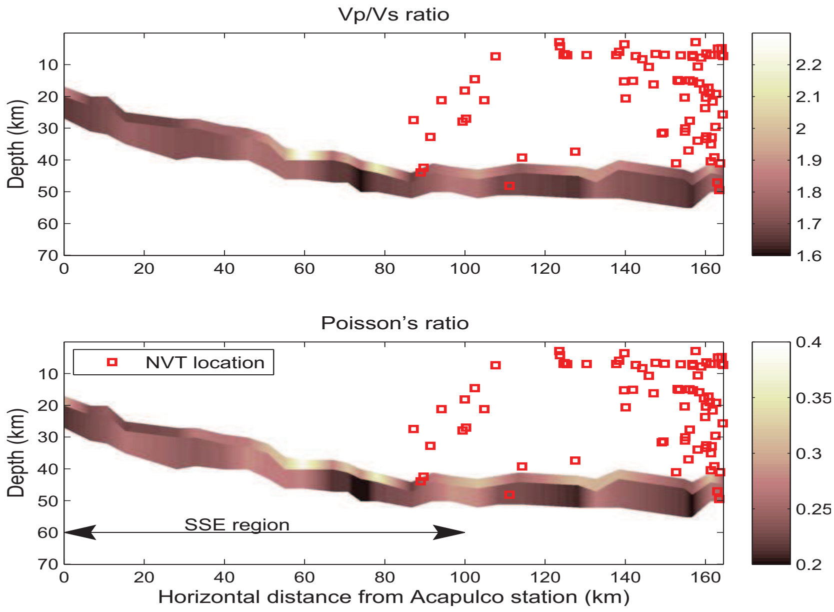

Figure 1.20: Final model including the (top) Vp/Vs and (bottom) Poisson's ratios of the subducted oceanic crust. The upper oceanic crust region has rapidly variable values (high Vp/Vs and Poisson's ratios on average) as opposed to the lower oceanic crust with moderately variable seismic properties. Most of the NVTs are located above the oceanic crust (a very few points inside the oceanic crust). The 2006 SSEs extend from the coast near Acapulco to a point 100 km to the north (*Larson et al.*, 2007).

steep angle of 75°. Such unusual subduction geometry suggests that central Mexico is in a slab rollback mode (*Pérez-Campos et al.*, 2008). This is confirmed by the age progression of the volcanism (*Ferrari*, 2004). An MT survey result (*Jödicke et al.*, 2006) also supports this idea based on a few isolated low-conductivity zones in the crust that they interpreted as episodes of slab dewatering as it rolls back.

The thin low-velocity (S wave velocity of 2.4−3.4 km/s) layer on top of the oceanic crust at a shallow depth (∼40 km) has important implications during the subduction history at central Mexico. If we assume the low-velocity layer is low-strength, then this would explain the decoupling of the slab from the overriding plate despite the horizontal interface. The decoupling is evidenced by the lack of compressional structures in the last 20 Ma (*Nieto-Samaniego et al.*, 2006; *Morán-Zenteno et al.*, 2007). Present GPS observations and the lack of compressional seismicity in the overlying plate also support this. *Manea and Gurnis* (2007) suggested that a thin channel of low-velocity mantle above the oceanic crust is a remnant of the mantle wedge, and provided a numerical model to support the present slab configuration.

Detailed mapping of inverted seismic parameters reveals that the upper oceanic crust is highly heterogeneous, and is composed of mechanically weak hydrous minerals (talc) on top of unaltered lower oceanic crust. The presence of such hydrous minerals in the oceanic crust reduces the seismic velocity to considerably less than the velocity of the surrounding mantle (*Kawakatsu and Watada*, 2007). The hydrous minerals become unstable at pressure and temperature conditions at around 50 km at the shallow subduction system and are dehydrated to become anhydrous eclogitic oceanic crust (*Kawakatsu and Watada*, 2007). Higher Vp/Vs and Poisson's ratios at the subhorizontal part of the oceanic crust at a depth of ∼40 km imply the presence of more free water and thus an active dewatering process due to the serpentinization process. In addition, lateral variations in the impedance (especially S wave velocity) in the upper oceanic crust directly correspond to its variable thickness. On the other hand, the lower oceanic crust is less heterogeneous and suggested to be unaltered by water.

Our interpretation for the low-velocity layer on top of the subducting Cocos plate can be correlated to the recent observations on the NVT and SSEs in central Meixco. Recent studies of episodic tremor and slip (ETS) in both Cascadia and Japan point to an origin that involves fluids near the plate boundary (*Audet et al.*, 2009; *Rubinstein et al.*, 2009). In particular, the NVT is a result of fluid-flow and fluid processes at the plate interface and within the overlying plate (*Rubinstein et al.*, 2009). The NVT coincides with the place within and above the subducting oceanic crust where the fluid content is suggested to be high. If the NVT is within the layer, then it is likely due to fluid motion. If it is above, it is likely due to fluid escaping from the interface into the continental crust. Furthermore, most slow slip patches coincide with the presence of the very low-velocity layer on top of the oceanic crust (*Larson et al.*, 2007).

High pore pressure might be in part responsible for anomalously low S wave velocity in the flat slab region which directly points to elevated Vp/Vs and Poisson's ratios in central Mexico (*Audet et al.*, 2009; *Christensen*, 1984; *Kawakatsu and Watada*, 2007; *Kodaira et al.*, 2004; *VanAvendonk et al.*, 2010). The thin (slab-parallel) layer characterized by depressed absolute velocities, and high Vp/Vs and Poisson's ratios is also seen in other subduction systems in SW Japan, Cascadia, and Costa Rica.

Christensen (1984) explained that the zone of high pore fluid pressure might be the cause of the high Poisson's ratio in the subducted crust based on the laboratory measurements of the P and S wave velocities as a function of confining pressure and pore pressure for oceanic crust (basalt) samples. In his experiment, the data show that decreases in seismic velocities accompany increasing pore pressure in oceanic rocks at fixed confining pressure. Thermal models provided by *Manea et al.* (2004) indicate that temperature and pressure gradients are small in the flat slab region before the TMVB (at about 45 km in depth). This suggests that the added pore pressure and the presence of hydrous minerals might be one of the key factors to explain the low S wave velocity (or high Poisson's ratio) in the horizontal part of the upper oceanic crust. Also, the friction across the slab interface may be further reduced by high fluid pressures as a result of metamorphic dehydration of the slab (*VanAvendonk et al.*, 2010). The influence of the pore pressure on seismic velocities is however expected to be diminished with depth and is unlikely to be significant at lower oceanic crustal depths where the porosity is extremely low (*Christensen*, 1984).

1.4 Conclusions

We have produced an image of the subducted Cocos plate beneath central Mexico with RFs utilizing data from the MASE. Some key observations include the most detailed images of the Moho and oceanic crust from the RF analysis. The RFs show that the subducting oceanic crust is shallow, dipping to the north at 15° for 80 km from Acapulco and then horizontally underplates the continental crust for a distance of approximately 250 km from the MAT to the southern extent of the TMVB. Beyond the flat subduction, the slab steeply subducts 75° beneath the TMVB shown from our migrated image using the P-to-S converted phase, which agrees with the tomography result (*Pérez-Campos et al.*, 2008; *Husker and Davis*, 2009), although the steeply dipping slab beneath the TMVB is not shown from our raw RFs.

The FD modeling result shows that we need a thin low-velocity layer (a thickness of 3 km; P wave velocity of 5.54 km/s; S wave velocity of 2.6 km/s) on top of the oceanic crust between the lower continental crust and the oceanic crust to explain the strong negative impedance contrast shown in the 1 s RF data. We suspect that hydrous materials or high pore pressure are responsible for the low velocities observed. Furthermore, they are likely a major factor for sustaining our flat subduction geometry and also reducing the tectonic coupling of two plates for more than 20 Ma. Most of the NVTs provided by *Payero et al.* (2008) are concentrated on the plate interface and the overlying crust, suggesting that the Cocos plate interface is an important pathway by which water is transported into the overlying crust. In particular, anomalously low S wave velocity in the upper oceanic crust deduced from our inversion directly points to elevated Vp/Vs and Poisson's ratios, indicating that the layer contains highly heterogeneous, weak, and hydrous minerals (talc) on top of normal lower oceanic crust.

Bibliography

Aki, K., and P. G. Richards (2002), *Quantitative Seismology*, 2nd ed., Univ. Sci. Books, Sausalito, Calif.

Ammon, C. J. (1991), The isolation of receiver effects from teleseismic P waveforms, *Bull. Seism. Soc. Am.*, *81*, 2501–2510.

Ammon, C. J., G. E. Randall, and G. Zandt (1990), On the nonuniqueness of receiver function inversions, *J. Geophys. Res.*, *95*(B10), 15,303–15,318, doi:10.1029/JB095iB10p15303.

Audet, P., M. G. Bostock, N. I. Christensen, and S. M. Peacock (2009), Seismic evidence for overpressured subducted oceanic crust and megathrust fault sealing, *Nature*, *457*, 76–78, doi:10.1038/nature.07650.

Bailey, W., and J. R. Holloway (2000), Experimental determination of elastic properties of talc to 800°C, 0.5 GPa; calculations of the effect on hydrated peridotite, and implications for cold subduction zones, *Earth Planetary Sci. Lett.*, *183*, 487–498, doi:10.1016/S0012-821X(00)00288-0.

Bostock, M. G., S. Rondenay, and J. Shragge (2001), Multiparameter two-dimensional inversion of scattered teleseismic body waves 1. Theory for oblique incidence, *J. Geophys. Res.*, *106*(B12), 30,771–30,782, doi:10.1029/2001JB000330.

Bostock, M. G., R. D. Hyndman, S. J. Rondenay, and S. Peacock (2002), An inverted continental Moho and the serpentinization of the forearc mantle, *Nature*, *417*, 536–538, doi:10.1038/417536a.

Christensen, N. I. (1984), Pore pressure and oceanic crustal seismic structure, *Geophys. J. R. Astron. Soc.*, *79*, 411–423.

Christensen, N. I., and M. H. Salisbury (1975), Structure and constitution of the lower oceanic crust, *Rev. Geophys. Space Phys.*, *13*, 57–86, doi:10.1029/RG013i001p00057.

Couch, R., and S. Woodcock (1981), Gravity and structure of the continental margins of southwestern Mexico and northwestern Guatemala, *J. Geophys. Res.*, *86*(B3), 1829–1840, doi:10.1029/JB086iB03p01829.

Duffy, T. S., and D. L. Anderson (1989), Seismic velocities in mantle minerals and the mineralogy of the upper mantle, *J. Geophys. Res.*, *94*(B2), 1895–1912, doi:10.1029/JB094iB02p01895.

Ferrari, L. (2004), Slab detachment control on mafic volcanic pulse and mantle heterogeneity in central Mexico, *Geology*, *32*, 77–80, doi:10.1130/G19887.1.

Ferrari, L., C. M. Petrone, and L. Francalanci (2001), Generation of oceanic-island basalt-type volcanism in the western Trans-Mexican volcanic belt by slab rollback, asthenosphere infiltration, and variable flux melting, *Geology*, *29*, 507–510, doi:10.1130/0091-7613(2001)029<0507:GOOIBT>42.0.CO;2.

Gephart, J. W. (1994), Topography and subduction geometry in the central Andes: Clues to the mechanics of a noncollisional orogen, *J. Geophys. Res.*, *99*(B6), 12,279–12,288, doi:10.1029/94JB00129.

Gómez-Tuena, A., L. Mori, N. E. Rincon-Herrera, F. Ortega-Gutierrez, J. Sole, and A. Iriondo (2008), The origin of a primitive trondhjemite from the Trans-Mexican volcanic belt and its implications for the construction of a modern continental arc, *Geology*, *36*, 471–474, doi:10.1130/G24687A.1.

Gorbatov A., and Y. Fukao (2005), Tomographic search for missing link between the ancient Farallon subduction and the present Cocos subduction, *Geophys. J. Int.*, *160*, 849–854, doi:10.1111/j.1365-246X.2005.02507.x.

Greene, F. (2009), Geometría de la placa de Cocos usando funciones receptor a lo largo de la línea MASE, M.S. thesis, 34 pp., Univ. Nac. Autón. de México, Mexico City, June.

Gutscher, M.-A. (2002), Andean subduction styles and their effect on thermal structure and interplate coupling, *J. S. Am. Earth Sci.*, *15*, 3−10, doi:10.1016/S0895-9811(02)00002-0.

Gutscher, M.-A., W. Spakman, H. Bijwaard, and E. R. Engdahl (2000), Geodynamics of flat subduction: Seismicity and tomographic constraints from the Andean margin, *Tectonics*, *19*, 814−833, doi:10.1029/1999TC001152.

Husker, A., and P. M. Davis (2009), Tomography and thermal state of the Cocos plate subduction beneath Mexico City, *J. Geophys. Res.*, *114*, B04306, doi:10.1029/2008JB006039.

Iglesias, A., R. W. Clayton, X. Pérez-Campos, S. K. Singh, J. Pacheco, D. Garcia, and C. Valdes-Gonzalez (2009), S-wave velocity structure below Central Mexico using high resolution surface wave tomography, *J. Geophys. Res.*, *115*, B06307, doi:10.1029/2009JB006332.

Jödicke, H., A. Jording, L. Ferrari, J. Arzate, K. Mezger, and L. Rüpke (2006), Fluid release from the subducted Cocos plate and partial melting of the crust deduced from magnetotelluric studies in southern Mexico: Implications for the generation of volcanism and subduction dynamics, *J. Geophys. Res.*, *111*, B08102, doi:10.1029/2005JB003739.

Jordings, A., L. Ferrari, J. Arzate, and H. Jödicke (2000), Crustal variations and terrane boundaries in southern Mexico as imaged by magnetotelluric transfer functions, *Tectonophysics*, *327*, 1−13, doi:10.1016/S0040-1951(00)00166-9.

Kawakatsu, H., and S. Watada (2007), Seismic evidence for deep-water transportation in the mantle, *Science*, *316*, 1468−1471, doi:10.1126/science.1140855.

Kay, R. W. (1978), Aleutian magnesian andesites: Melts from subducted Pacific ocean crust, *J. of Volcanol. and Geotherm. Res.*, *4*, 117−132, doi:10.1016/0377-0273(78)90032-X.

Kikuchi, M., and H. Kanamori (1982), Inversion of complex body waves, *Bull. Seism. Soc. Am.*, *71*, 491−506.

Kodaira, S., T. Iidaka, A. Kato, J. Park, T. Iwasaki, and Y. Kaneda (2004), High pore fluid pressure may cause silent slip in the Nankai Trough, *Science*, *304*, 1295–1298, doi:10.1126/science.1096535.

Kostoglodov, V., S. K. Singh, J. A. Santiago, S. I. Franco, K. M. Larson, A. R. Lowry, and R. Bilham (2003), A large silent earthquake in the Guerrero seismic gap, Mexico, *Geophys. Res. Lett.*, *30*(15), 1807, doi:10.1029/2003GL017219.

Lallemand, S., A. Heuret, and D. Boutelier (2005), On the relationships between slab dip, back-arc stress, upper plate absolute motion, and crustal nature in subduction zones, *Geochem. Geophys. Geosyst.*, *6*, Q09006, doi:10.1029/2005GC000917.

Langston, C. A. (1979), Structure under Mount Rainier, Washington, inferred from teleseismic body waves, *J. Geophys. Res.*, *84*(B9), 4749–4762, doi:10.1029/JB084iB09p04749.

Larson, K., V. Kostoglodov, S. Miyazaki, and J. A. S. Santiago (2007), The 2006 aseismic slow slip event in Guerrero, Mexico: New results from GPS, *Geophys. Res. Lett.*, *34*, L13309, doi:10.1029/2007GL029912.

Ligorria J. P., and C. J. Ammon (1999), Iterative deconvolution and receiver function estimation, *Bull. Seism. Soc. Am.*, *89*, 19–36.

Mainprice, D., Y. Le Page, J. Rodgers, and P. Jouanna (2008), *Ab initio* elastic properties of talc from 0 to 12 GPa: Interpretation of seismic velocities at mantle pressures and prediction of auxetic behaviour at low pressure, *Earth Planetary Sci. Lett.*, *274*, 327–338, doi:10.1016/j.epsl.2008.07.047.

Manea, V. C., and M. Gurnis (2007), Subduction zone evolution and low viscosity wedges and channels, *Earth Planetary Sci. Lett.*, *264*, 22–45, doi:10.1016/j.epsl.2007.08.030.

Manea, V. C., M. Manea, V. Kostoglodov, C. A. Currie, and G. Sewell (2004), Thermal structure, coupling and metamorphism in the Mexican subduction zone beneath Guerrero, *Geophys. J. Int.*, *158*, doi:10.1111/j.1365-246X.2004.02325x.

Morán-Zenteno, D. J., M. Cerca, and J. D. Keppie (2007), The Cenozoic tectonic and magmatic evolution of southwestern Mexico: Advances and problem interpretation, *Geology of Mexico, Celebrating the Centenary of the Geological Society of Mexico*, edited by S. A. Alaniz-Álvarez and Á. F. Nieto-Samanieto, *Spec. Pap. Geol. Soc. Am.*, *422*, 71–91.

Müller, R. D., M. Sdrolias, C. Gaina, and W. R. Roest (2008), Age, spreading rates, and spreading asymmetry of the world's ocean crust, *Geochem. Geophys. Geosyst.*, *9*, Q04006, doi:10.1029/2007GC001743.

Nieto-Samaniego, Á. F., A. S. Alaniz-Álvarez, G. Silva-Romo, M. H. Eguiza-Castro, and C. Mendoza-Rosales (2006), Latest Cretaceous to Miocene deformation events in the eastern Sierra Madre del Sur, Mexico, inferred from the geometry and age of major structures, *Geol. Soc. Am. Bull.*, *118*, 238–252, doi:10.1130/B25730.1.

Pardo, M., and G. Suárez (1995), Shape of the subducted Rivera and Cocos plates in southern Mexico: Seismic and tectonic implications, *J. Geophys. Res.*, *100*(B7), 12,357–12,373, doi:10.1029/95JB00919.

Pawley, A. R., S. A. T. Redfern, and B. J. Wood (1995), Thermal expansivities and compressibilities of hydrous phases in the system MgO-SiO2-H2O: talc, phase A and 10-A phase, *Contrib. Mineral. Petrol.*, *122*, 301–307, doi:10.1029/2007GL032877.

Payero, J. S., V. Kostoglodov, N. Shapiro, T. Mikumo, A. Iglesias, X. Pérez-Campos, and R. W. Clayton (2008), Nonvolcanic tremor observed in the Mexican subduction zone, *Geophys. Res. Lett.*, *35*, L07305, doi:10.1029/2007GL032877.

Pérez-Campos, X., Y. Kim, A. Husker, P. M. Davis, R. W. Clayton, A. Iglesias, J. F. Pacheco, S. K. Singh, V. C. Manea, and M. Gurnis (2008), Horizontal subduction and truncation of the Cocos Plate beneath central Mexico, *Geophys. Res. Lett.*, *35*, L18303, doi:10.1029/2008GL035127.

Reynard, B., N. Hilairet, E. Balan, and M. Lazzeri (2007), Elasticity of serpentines and extensive serpentinization in subduction zones, *Geophys. Res. Lett.*, *34*, L13307, doi:10.1029/2007GL030176.

Rubinstein, J. L., D. R. Shelly, and W. L. Ellsworth (2010), Non-Volcanic Tremor: A window into the roots of fault zones, *New Frontiers in Integrated Solid Earth Sciences*, edited by S. Cloetingh and J. Negendank, pp. 287–314, Springer, Dordrecht, Netherlands.

Sanchez-Valle, C., S. V. Sinogeikin, J. R. Smyth, and J. D. Bass (2008), Sound velocities and elasticity of DHMS phase A to high pressure and implications for seismic velocities and anisotropy in subducted slabs, *Phys. Earth Planet. Inter.*, *170*, 229–239, doi:10.1016/j.pepi.2008.07.015.

Schellart, W. (2008), Overriding plate shortening and extension above subduction zones: a parametric study to explain formation of the Andes mountains, *Geol. Soc. Am. Bull.*, *120*(11), 1441–1454, doi:10.1130/B26360.1.

Schellart, W., J. Freeman, D. Stegman, L. Moresi, and D. May (2007), Evolution and diversity of subduction controlled by slab width, *Nature*, *446*, 308–311, doi:10.1038/nature05615.

Song, T.-R. A.,D. V. Helmberger, M. R. Brudzinski, R. W. Clayton, P. Davis, X. Pérez-Campos, and S. K. Singh (2009), Subducting slab ultra-slow velocity layer conincident with silent earthquake in southern Mexico, *Science*, *324*, 502–506, doi:10.1126/science.1167595.

Valdes-Gonzalez, C., and R. P. Meyer (1996), Seismic structure between the Pacific coast and Mexico City from the Petatlan earthquake (Ms=7.6) aftershocks, *Geofís. Int.*, *35*, 4377–4401.

Van Avendonk H., W. S. Holbrook, D. Lizarralde, M. M. Mora, S. Harder, A. D. Bullock, G. E. Alvarado, and C. J. Ramirez (2009), Seismic evidence for fluids in fault zones on top of the subducting Cocos plate beneath Costa Rica, *Geophys. J. Int.*, *181*, 997–1016, doi:10.1111/j.1365-246X.2010.04552.x.

Wagner L. S., M. L. Anderson, J. M. Jackson, S. L. Beck, and Z. Zandt (2008), Seismic evidence for orthopyroxene enrichment in the continental lithosphere, *Geology*, *36*, 935–938, doi:10.1130/G25108A.1.

Yan, Z., and R. W. Clayton (2007), Regional mapping of the crustal structure in southern California from receiver functions, *J. Geophys. Res.*, *112*, B05311, doi:10.1029/2006JB004622.

Zandt, G., and C. J. Ammon (1995), Continental crust composition constrained by measurements of crustal Poisson's ratio, *Nature*, *374*, 152–154, doi:10.1038/374152a0.

Zhu L., and H. Kanamori (2000), Moho depth variation in southern california from teleseismic receiver functions, *J. Geophys. Res.*, *105*(B2), 2969–2980, doi:10.1029/1999JB900322.

Chapter 2

Evidence of a Collision between the Yucatán Block and Mexico in the Miocene

Abstract

We present the evidence for an anomalous south-dipping slab in southern Mexico. The main evidence comes from a clear receiver function image along a seismic line across the Isthmus of Tehuantepec and is also supported by a previous global tomographic model. The slab dips at 35 degrees, is approximately 250 km in length, and appears to truncate the Cocos slab at about 120 km depth. We hypothesize that the slab was created by the collision of the Yucatán Block with Mexico at approximately 12 Ma. This scenario would explain the Chiapas Fold and Thrust Belt as the product of this collision, and its age constrains the date of the event to be in the Miocene.

2.1 Introduction

Southern Mexico is a transition zone between the flat slab subduction of central Mexico (Pardo & Suárez, 1995; Pérez-Campos et al., 2008; Kim et al., 2010) and the steep subduction of northern Central America (Syracuse & Abers, 2006). The seismicity indicates that the Wadati-Benioff zone transitions smoothly through the region, even as it crosses the boundary between the North American (NA) and Caribbean (CA) Plates (Burbach et al., 1984; Rebollar et al., 1999). The slab dip varies from horizontal near Mexico City, 30° where it crosses the Isthmus of Tehuantepec, to 45° where it crosses the Mexico-Guatemalan border (Burbach et al., 1984; Rebollar et al., 1999) (Figure 2.1a).

The volcanic arc, however, does not follow this smooth transition (Figure 2.1a). In central Mexico, the arc was active along the coast until it extinguished ∼25 Ma. During the early Miocene, the arc reappeared rapidly inland ∼250 km to the northern edge of the Trans Mexican Volcanic Belt (TMVB) (Ferrari, 2004). Slab rollback in the mid- to late-Miocene has brought it to its current location along the southern edge of the TMVB (Ferrari, 2004). In Central America, southeast of the Mexico-Guatemala border, the active arc is along the coast where the Cocos Plate is at 100 km depth under the NA Plate. In between, in southeastern Mexico, the active arc is discontinuous, and consists of three isolated volcanic zones: Los Tuxtlas Volcanic Field (LTVF), El Chichión, and the Modern Chiapanecan Volcanic Arc (MCVA). These zones do not have the usual location relative to the underlying slab.

In 2007−2008, a 45-station broadband Veracruz-Oaxaca (VEOX) seismic line was deployed in southeastern Mexico across the Isthmus of Tehuantepec in order to image the subduction zone. The receiver function (RF) results show an image of the northward-dipping Cocos slab down to ∼100 km depth, but in addition, the RF image also shows a slab-like structure that dips 35° to the south that can be seen to 250 km depth. This anomalous feature has no known role in the current tectonic models of the region.

In this paper we show the receiver function results and present a model to support a hypothesis that the anomalous slab may have been due to the collision of the Yucatán Block with Mexico. The timing of this event is likely indicated by the

Chiapas Fold and Thrust Belt (CFTB), which is a compressional structure parallel to the proposed suture zone and was created ∼13−11 Ma (Mandujano-Velazquez & Keppie, 2009). Other authors have proposed that the Yucatán Block (including the Campeche shelf) fits in a Wegnerian sense into the coast along the northern Gulf of Mexico (e.g., Bird et al., 2005; Dickinson, 2009, and references therein), but have generally assumed its separation from the Gulf coast occurred in the Jurassic. This is consistent with the standard model for the age of the deep sea floor in the Gulf of Mexico (Pindell & Dewey, 1982; Marton & Buffler, 1994). The model we are proposing would have the Yucatán Block rotate clockwise to a position near Florida during opening of the Gulf in the Jurassic, and then move southwestwards relative to North America to its current position during the Miocene.

2.2 Data and Receiver Function Imaging Method

We use the teleseismic P-to-S (Ps) converted wave, equivalently receiver function (RF) (e.g., Vinnik, 1977; Langston, 1979), for imaging the lithospheric structure beneath southern Mexico. The method removes source-related and mantle-path effects by deconvolution, enhancing Ps conversions and reverberations associated with crustal and mantle structure beneath the receiver. The amplitudes of the Ps phases primarily depend on the incidence angle of the impinging teleseismic P wave and the velocity contrast across the discontinuities. The relative arrival times of the converted phases and multiples depend on the depth of the velocity discontinuities, and the P- and S-wave velocity structure between the discontinuities and the surface (Zhu & Kanamori, 2000).

We will mainly concentrate on radial RFs, which can be obtained by deconvolving the vertical component seismograms from the radial components. All references to the RF in this paper will be to the radial RF. In similar manner, tangential RFs can be calculated using the tangential component seismograms, and provide information on anisotropy and help to identify dipping structures (Savage, 1998). We note that the tangential RF image (Figure 2.4b) does not show strong conversions at the anomalous south-dipping slab from the Gulf of Mexico (see Section 2.3).

The location of the VEOX line is shown in Figures 2.1a and 2.1b. Of 45 stations

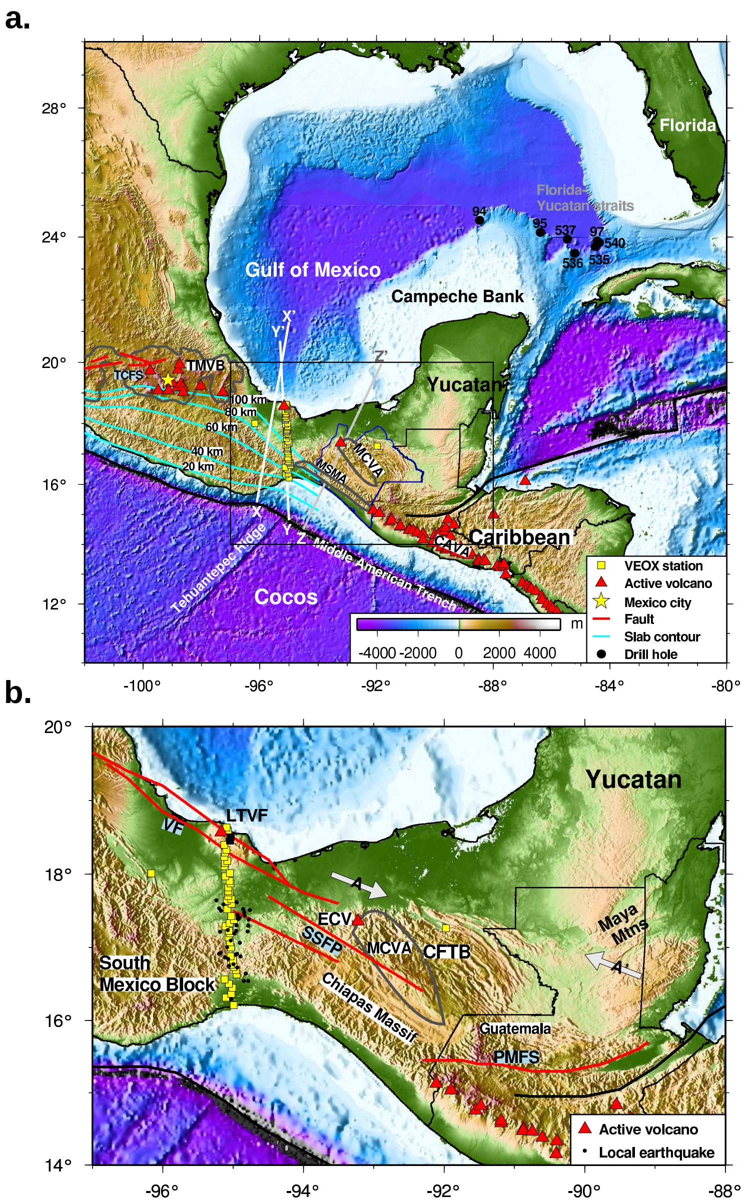

Figure 2.1: Topographic-bathymetric maps showing the region of the study and stations. (a) The map showing station locations of the VEOX seismic line in yellow squares and active volcanoes in red triangles. Isodepth contours of the Cocos Plate beneath the North American (NA) Plate (Pardo & Suárez, 1995) are shown as cyan lines in the map. Locations of tomographic profiles are indicated as lines X-X′, Y-Y′ (along the VEOX line), and Z-Z′. Black dots with site numbers indicate selected Deep Sea Drilling Project (DSDP) drill holes. Gray solid lines represent volcanic belts (TMVB in central Mexico and MCVA in the Chiapas State). A blue solid line represents the Chiapas State. Red lines within the TMVB outline the TCFS, and their locations were extracted from Andreani et al. (2008). The abbreviations shown in the map are TMVB, Trans Mexican Volcanic Belt; MCVA, Modern Chiapanecan Volcanic Arc; MSMA, Miocene Sierra Madre Arc; CAVA, Central American Volcanic Arc; TCFS, Tula-Chapala fault system. (b) Regional topographic map showing a lineament in the approximate location of the proposed Mexico-Yucatán suture zone, indicated by two gray arrows (A and A′). The selected local earthquakes, recorded from the VEOX line, are plotted as black dots near the VEOX line. Red lines outline main fault systems in southern Mexico, and their locations from Andreani et al. (2008). The abbreviations shown in the map are LTVF, Los Tuxtlas Volcanic Field; ECV, El Chichón; VF, Veracruz Fault; SSFP, Strike-Slip Fault Province; PMFS, Polochic-Motagua Fault System; CFTB, Chiapas Fold and Thrust Belt. The location of this map is shown in (a).

installed in southern Mexico, only 40 provided useable seismic records. The average distance between stations is about 6 km. For the RF analysis, a total of 68 teleseismic earthquakes of magnitude greater than 6.1 from July 2007 to October 2008, with epicentral distances between 30° and 90° and depth ranges between 6 km and 635 km, were used (Figure 2.2a). The range in incident angles of the impinging P wave at the top of the anomalous south-dipping slab is illustrated in Figure 2.2b. Individual waveform data are time-windowed to 90 s and rotated to radial and tangential coordinates. These data were then processed in two passbands, (1) a lower frequency band from 0.08 to 0.33 Hz and (2) a higher frequency band from 0.01 to 1 Hz.

We first used a lower frequency band (0.08 to 0.33 Hz) to constrain the geometry of the Cocos slab based on the radial RFs. The lower frequency band is used to improve the signal-to-noise ratio for those stations, especially near the Pacific coast, and to minimize the effect of local seismicity where the data quality was significantly affected by frequent flooding. We then used the iterative time domain deconvolution technique (Kikuchi & Kanamori, 1982; Ligorria & Ammon, 1999) to compute the RFs. The time domain deconvolution worked better in sharply constraining the geometry than the frequency domain deconvolution (Langston, 1979; Ammon et al., 1990). As shown in Figure 2.2a, the earthquakes generally occurred in four different back azimuth groups. The RFs from each group is separately stacked to investigate the azimuthal variations. In particular, 20 events from the southeast (SE) back azimuth group are separately analyzed to study the south-dipping slab. With these data the higher frequency band (0.01−1.0 Hz) is used.

The RFs used in the analysis are sorted first by station position along the array, and second for each station, by back azimuth of incident wavefields. Each column for a single station is then separated by the vertical line as shown in Figure 2.3. We do this procedure for all 40 stations and concatenate along the station position. The distance between center points of two adjacent columns represents the distance between two stations. The thickness of the RF column bin is thus not uniform for each station. The red and blue colors of the RF amplitudes in Figure 2.3 correspond to velocity increase and decrease with depth, respectively. The color of the images for radial and tangential RFs represents the absolute amplitudes of RFs.

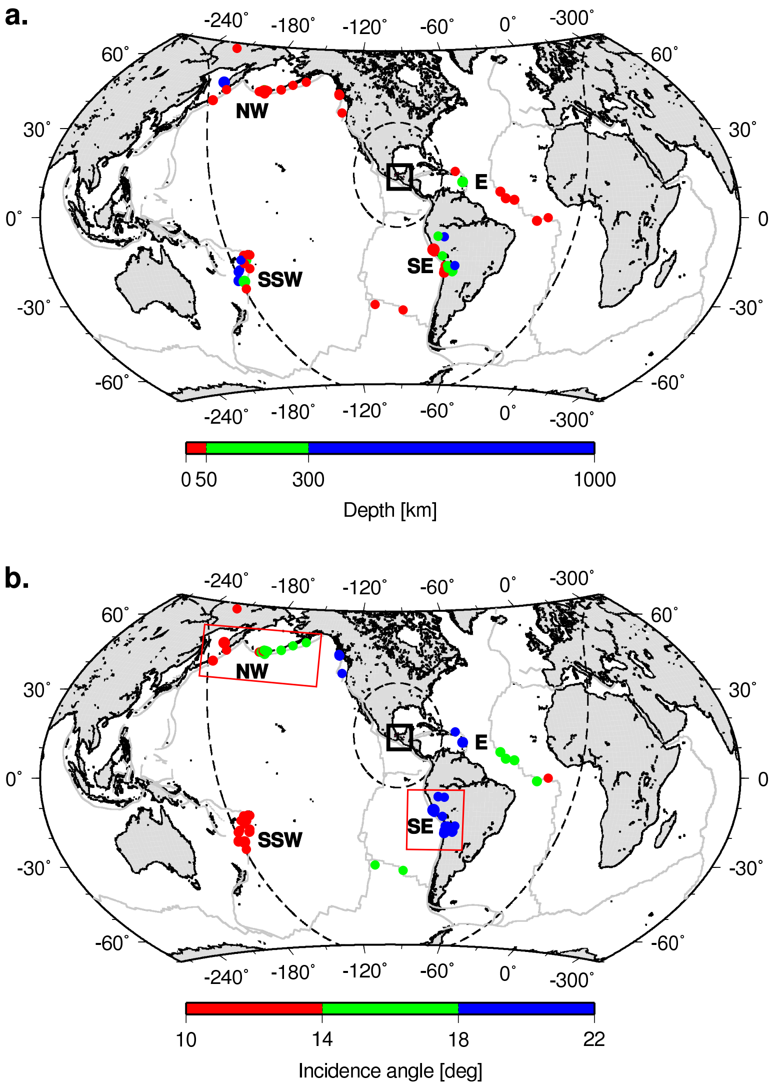

Figure 2.2: Distribution of teleseismic events used in the analysis, including 7 events in a east (E) back azimuth band from 83° to 97°, 20 events in a southeast (SE) band from 138° to 149°, 15 events in a south-southwest (SSW) band from 244° to 253°, and 23 events in a northwest (NW) band from 319.1° to 341.5° from the VEOX line enclosed in the box. Dashed lines are a distance of 30° and 90° away from the central point of the VEOX line. (a) Distribution of the teleseismic events colored according to depths. The size of the circle is scaled to the size of the earthquake. (b) Distribution of the teleseismic events colored according to the incidence angles of the teleseismic P waves impinging through the south-dipping slab from the Gulf of Mexico (Yucatán slab). The size of the circle is also scaled to the size of the earthquake. The events in SE and NW bands are enclosed in red boxes.

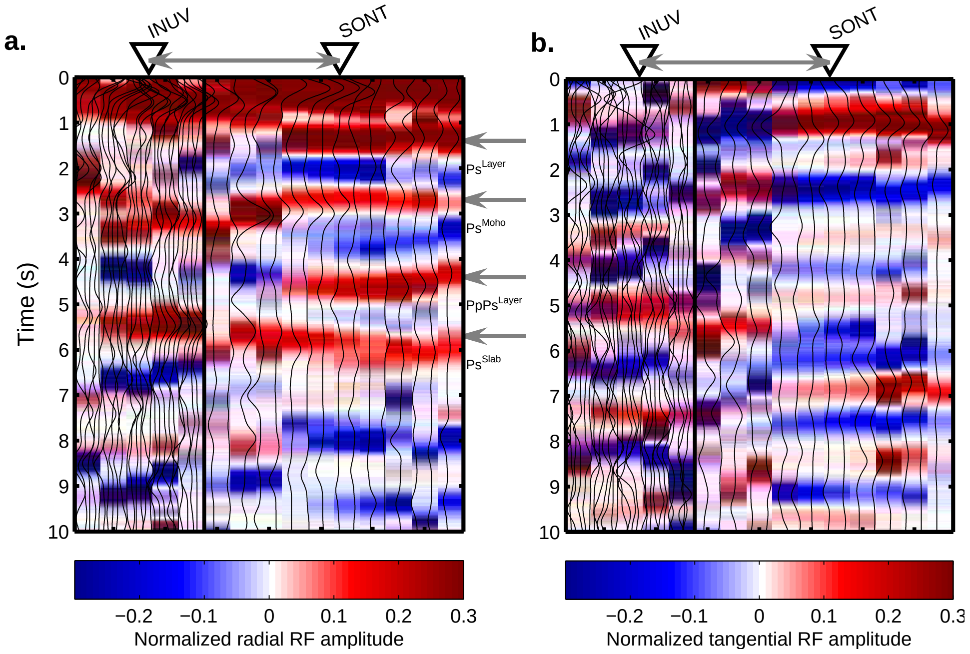

Figure 2.3: High-pass version of RF record section and RF image for two stations (INUV and SONT). The locations of the two adjacent stations are indicated as black squares at the northern part of VEOX line in Figure 2.1b. The figure demonstrates how the RF imaging is done. The RFs for each station are sorted by the order of increasing back azimuth of the incident wavefield. (a) The radial RF image overlain with 29 and 16 RF traces for stations INUV and SONT, respectively. A strong positive arrival between 4 and 5 s in SSW and NW bands is the seismic multiple phase (PpPs) from Ps phase between 1 and 1.5 s after P arrival at 0 s. Double pulses for the P arrival are commonly observed in the northern part of VEOX line, especially LTVF. Zamora-Camacho et al. (2010) also observed a layer at 10−14 km from the RF analysis, which they interpreted as the layer between the upper sedimentary layer and transitional crust found elsewhere in the margins of the Gulf of Mexico. (b) The tangential RF image overlain with 29 and 16 traces for stations INUV and SONT, respectively.

2.3 Slab Image in Southern Mexico

Figures 2.4a−d show an image of the Cocos slab to a depth of about 120 km, along with the continental Moho of the overriding NA Plate between 3 and 5 s after the P wave arrival at 0 s. The images are constructed incorporating the teleseismic events from all azimuths (Figure 2.2), filtered to 0.08−0.33 Hz to increase signal-to-noise ratio by suppressing the high noise level in the seismic waveforms near the coast. The top and bottom interfaces of the oceanic crust of the Cocos slab are defined by the negative (blue) and positive (red) radial RF pulses, respectively (Figure 2.4a). Oppositely polarized Ps pulses are the result of waves converted from the top and bottom boundaries of a dipping, low-velocity layer, indicated by dashed lines (Figure 2.4c). A similar RF image of the Cocos slab can be found from Melgar (2009) and Melgar & Pérez-Campos (2010) using the teleseismic data filtered in the same low-pass band. The dip of the Cocos slab is estimated to be 25 degrees. The consistent negative RF pulse before the positive RF pulse indicates an existence of the low-velocity layer at the top part of the subducting oceanic crust,which is discussed in detail in Kim et al. (2010). The location of the Cocos oceanic crust can be also traced from the tangential RF image (Figures 2.4b and 2.4d) although the tangential RF amplitudes are a factor of 2 smaller than the radial ones.

The local seismicity in Figures 2.4c and 2.4d delineates a Wadati-Benioff subduction zone beneath the continental Moho. A total of 38 local earthquakes in the magnitude range from 3.4 to 5.7 are taken from the VEOX line from September 2007 to March 2009. These events were relocated using data from the VEOX array and the S-wave velocity model of Campillo et al. (1996), derived from the inversion of group velocity dispersion data (Castro Artola, 2010). The double-difference algorithm of Waldhauser & Ellsworth (2000) was used leading to an estimated depth error of 2−4 km. As shown in Figures 2.4c and 2.4d, most of the seismicity occurs below the oceanic crust and within the oceanic mantle of the subducted Cocos slab. We note that small difference in slope between the relocated seismicity and converted Ps phases corresponding to the oceanic crust is primarily from the difference in the velocity model used. The main difference comes from the crustal velocities from 0 to 17 km, which will lead to a 3.07 s delay in phase arrival times.

The image shown in Figure 2.5a is the stack of 20 events that span a distance range of 40−50 degrees with source depths ranging from 20 to 635 km (Figure 2.5a). In the figure, there is a clear south-dipping structure (denoted hereafter as the Yucatán slab) that extends from the northernmost station on the Gulf of Mexico to 250 km depth with a 35° dip. This image is constructed incorporating teleseismic events from the SE back azimuth band (Figure 2.2a), filtered to 0.01−1 Hz. The Yucatán slab appears to truncate the Cocos slab image at ∼120 km depth (Figure 2.5a). We note that the Cocos slab is weakly visible in this image from the dataset filtered to 0.01−1 Hz because of the high noise level in the coastal area. There is some indication that the seismicity follows the trend of the Yucatán slab starting at the intersection point with the Cocos slab (Figures 2.4c and 2.5a). A similar focused zone of earthquakes ("the Bucaramanga nest") was also found where the Caribbean and Nazca Plates collide under Colombia (Zarifi et al., 2007).

The image of the Yucatán slab is sharp and well-defined for its entire length, except for its termination at depth, which is somewhat ambiguous (Figure 2.5a). Examples of receiver gathers for three stations in the middle and northern section of the VEOX line show clear arrivals from the slab structure only in the SE back azimuth range (Figure 2.6). This indicates that the Yucatán slab exists primarily to the east of the VEOX line. Later, this result is also supported by the global tomography result (see Section 2.5). We note that the Yucatán slab is also observed in the low-passed RFs in Figure 2.4a, but it is somewhat fuzzy because events from all back azimuths are included in the RF stack.

The image of the Yucatán slab is unlikely to be an artifact because the various raypaths (Figure 2.2) that are used to construct the image are sufficiently different, and are also far enough away from the triplications in the upper mantle. Thus, it is unlikely that source-side structure and path effects are mapped into the image. Scattering from near-surface structures adjacent to the VEOX line would tend to produce weak incoherent arrivals and not the strong linear image that is seen in Figure 2.5a. A linear feature could be produced by scattering of surface waves by an unknown shallow feature at the northern end of the VEOX line, but the arrival would not have the apparent phase velocity that is seen in the RF images. The RF image using the transverse component does not show a strong image of the Yucatán slab (Figure 2.4b).

2.4 Receiver Function Finite-Difference Modeling

To further investigate the RF images that show the Cocos and Yucatán slabs, we produce synthetic RFs with a 2 D finite-difference wave propagation program for particular velocity and slab geometry models and compare these to the data. The laterally complicated structure, such as two opposing slabs (Cocos and Yucatán slabs) and Moho, leads to very complicated images containing converted phases, Pds (P-to-S conversion at a discontinuity, d) and Pms (P-to-S conversion at the Moho, m), and their seismic multiples. To focus on the subducted slabs, we construct two simple models that only include the Cocos slab (Model 1) or the Yucatán slab (Model 2) (Figures 2.7 and 2.8). In this section, we investigate how the RF synthetics behave with different frequency filters (1, 2, and 3 s) and polarity of the incidence angle of the incoming plane waves (SE or NW). In addition, we only show the RF synthetics generated from one velocity model, which primarily fits the amplitude of the negative and positive pulses corresponding to the top and bottom of the subducting crusts, respectively, and the timing of these two pulses for 1 s data.

On the basis of our observations in Section 2.3 (Figure **??**a), Model 1 includes the Cocos slab, which dips 25° (Figure **??**a). Model 2 includes the Yucatán slab, which dips 35° (Figure **??**a). We did not include the continental crust in the model (3−5 s based on Figure **??**a) to avoid strong seismic multiples, which interfere with direct arrivals from the Cocos and Yucatán slabs.

For both models, we strictly limit lateral and vertical extents of the models and pick the section where the amplitude of the converted phases (at the top and bottom of the crust part of the slabs) is somewhat uniform in the data within the specified model space. The vertical extent is set from 0 km to 150 km, and the lateral extent from 0 km to 110 km for Model 1 (Figure 2.7b) and to 75 km for Model 2 (Figure 2.8a). The 14 receivers at zero depth with the receiver spacing of 8 km are placed for Model 1 (Figure 2.7a), and the 13 receivers are placed with the receiver spacing of 6.25 km for Model 2 (Figure 2.8a).

Figure 2.2b shows calculated incident angles at the top of the Yucatán slab, which

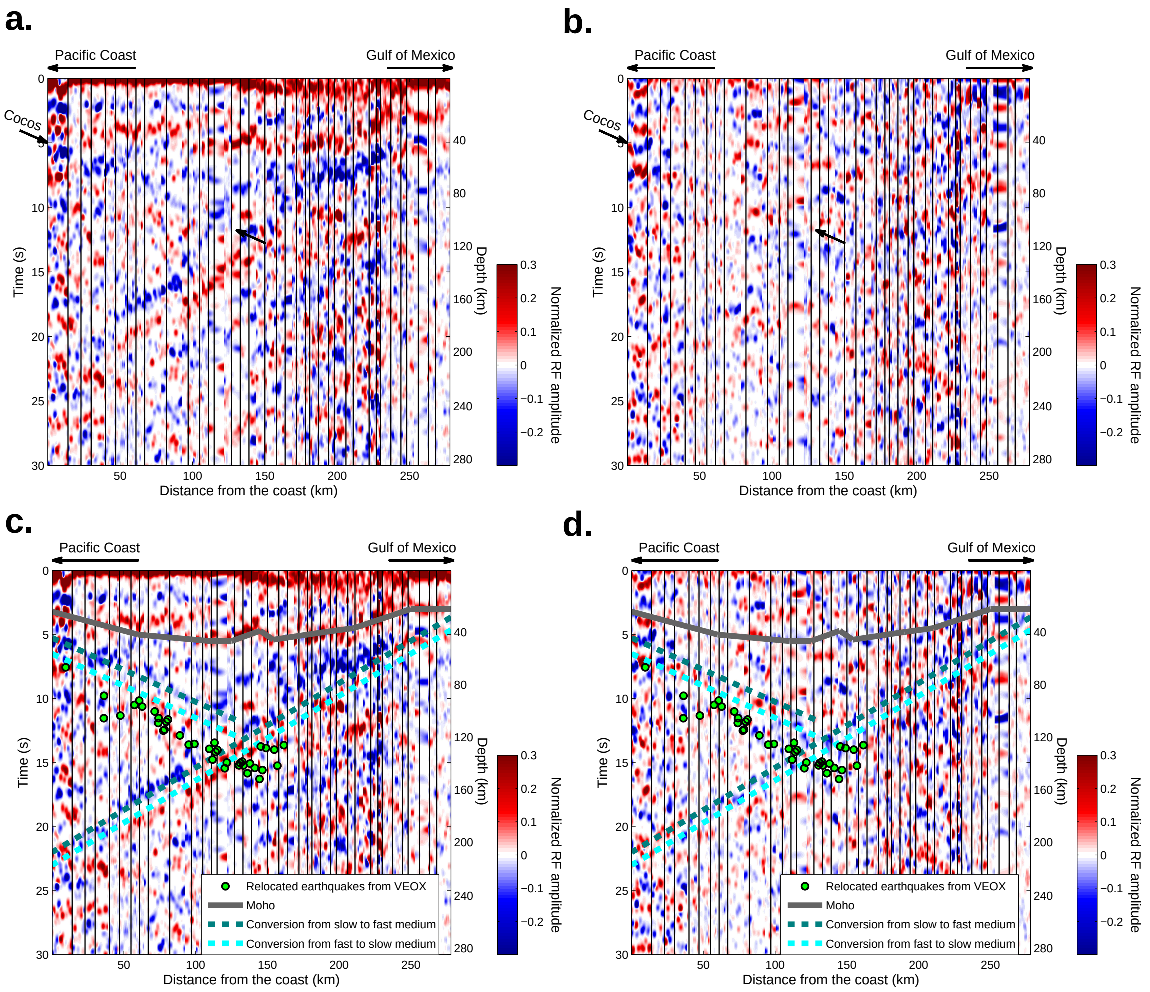

Figure 2.4: Low-pass version of the radial (a, c) and tangential (b, d) RF images showing Cocos slab, utilizing data from all azimuths (Figure 2.2a). The seismograms from the 68 teleseismic earthquakes are filtered to 0.08−0.33 Hz. The time axis on the left hand side is mapped directly to the depth on the right hand side using IASP91 velocity model (Kennett & Engdahl, 1991). (a) The radial RF image without interpretation lines. (b) The tangential RF image without interpretation lines. (c) The radial RF image showing Cocos slab with local seismicity. The top and bottom interfaces of the Cocos oceanic crust are indicated by dotted lines, and separated by 8−10 km thickness. The local earthquakes plotted are recorded from the VEOX line as green circles. The 38 earthquakes from the VEOX line are relocated using the double-difference algorithm of Waldhauser & Ellsworth (2000) (Castro Artola, 2010). The earthquakes are selected from epicenters within 25 km of the VEOX line (Figure 2.1b). (d) The tangential RF image with interpretation lines and local seismicity.

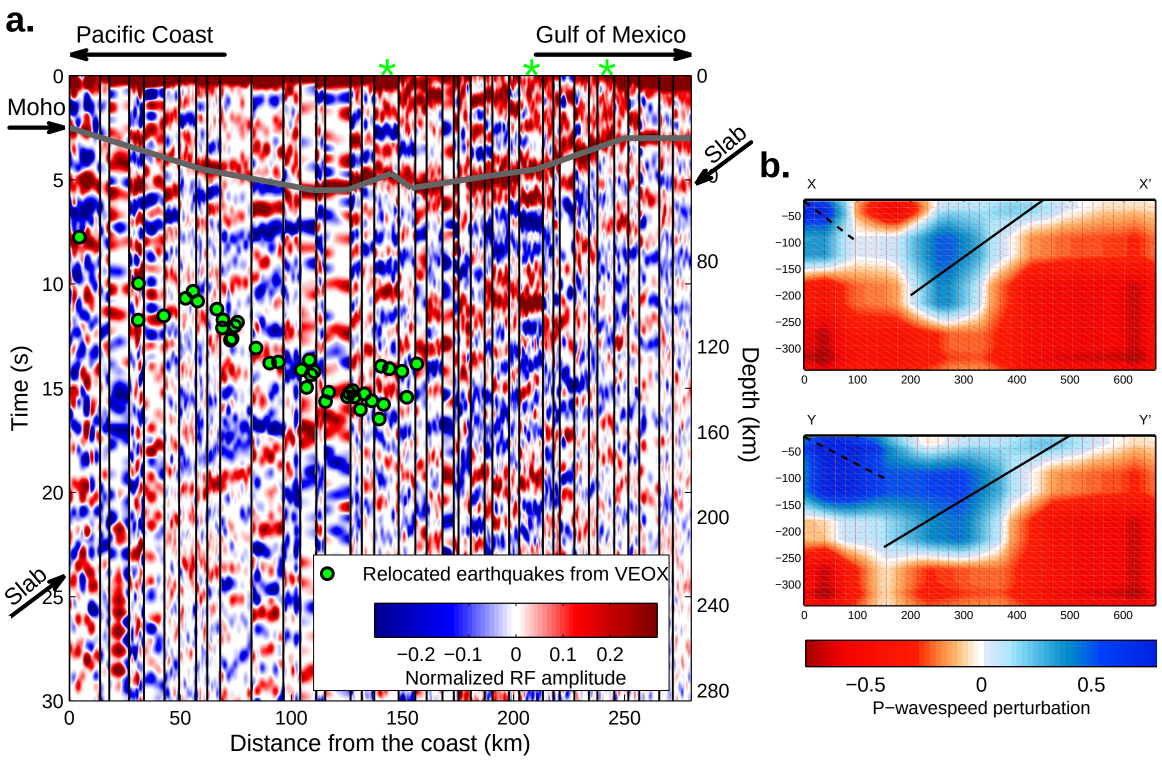

Figure 2.5: High-pass version of RF and global tomography results. (a) RF image showing the Moho and the Yucatán slab from the Gulf of Mexico. The seismograms from the 20 teleseismic earthquakes are filtered to 0.01−1 Hz. The locations of teleseismic earthquakes used to construct the RF image are shown in Figure 2.2b (red box, labeled as SE). The local earthquakes plotted are the same ones in Figures 2.4c and 2.4d. The receiver gathers for stations indicated as green asterisk symbols are in Figure 2.6. (b) Cross sections of the profile X-X′ and Y-Y′ (Figure 2.1) through the global P-wave tomography model of Li et al. (2008), showing the image of the Yucatán slab (solid lines) and Cocos slab (dotted lines).

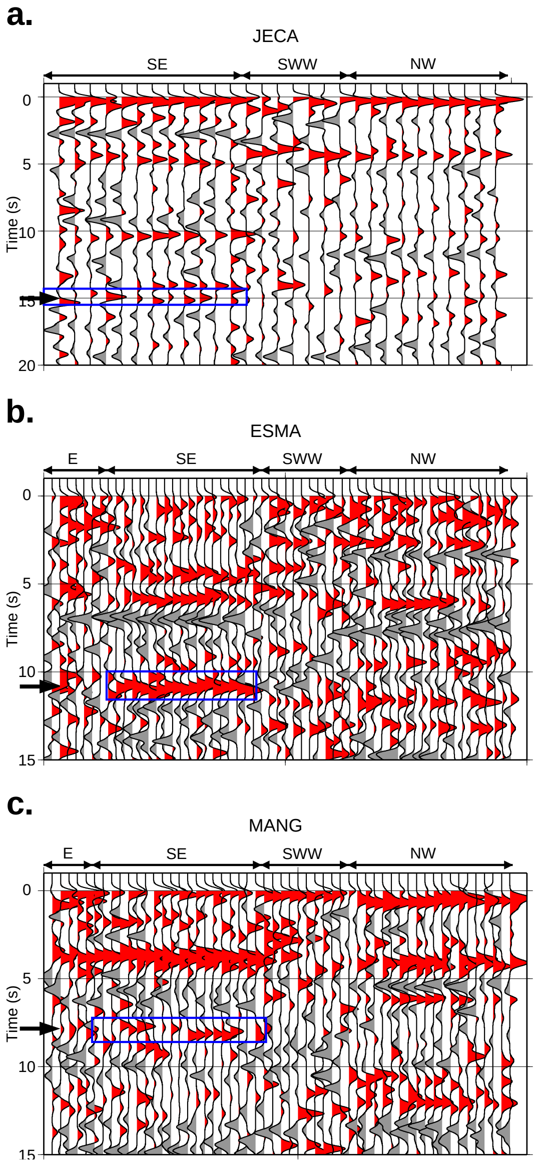

Figure 2.6: RF gathers from three stations (JECA, MANG, and ESMA) that show the arrival (in a blue box) from the Yucatán slab only on the SE back azimuths. Each seismogram is filtered to 0.01−1 Hz. Locations of the stations are shown in Figure 2.5a, and the stations from top to bottom are in the order of increasing distance from the Pacific coast.

range from 18° to 22° for the SE quadrant and from 10° to 18° for the NW quadrant. For the typical RF synthetics, plane waves with variable incident angles in the range of the ray parameter from 0.04 to 0.08 (18.66° to 39.79°) are used. In our analysis, since the incoming angle is quite small (10° to 22°), we only generate the synthetic seismograms using the ray parameter of 0.04 (18.66°). In addition, we use the iterative time domain deconvolution (Kikuchi & Kanamori, 1982; Ligorria & Ammon, 1999) to convert the synthetic seismograms to the radial RFs (Figures 2.7b and 2.8b).

We first note that the amplitudes of the synthetic RFs for the SE and NW quadrants are different for all three frequency bands (Figures 2.7b and 2.8b). The amplitudes of the converted waves from both slabs are more sensitive to the direction of the incoming wave. In Figure 2.8b, the amplitudes of the synthetic RFs for the NW quadrant are consistently smaller than those for the SE quadrant for the Yucatán slab. We do not see such a significant reduction in amplitude for the Cocos slab (Figure 2.7b). Our simulation result may explain why we do not see strong amplitudes from the Yucatán slab in the NW back azimuth from the real data (Figures 2.5a and 2.6), and also why this dipping feature becomes degraded if all the azimuth data are added in the image (Figure 2.4a).

2.5 Tomographic Images

Many cross sections through Mexico from global P-wave tomographic inversions have shown a coarse-scale image of the Cocos slab (Gorbatov & Fukao, 2005; Rogers et al., 2002; Li et al., 2008). In Figure 2.5b, two slices from a tomographic P-wave model of Li et al. (2008) show a southward-dipping structure (in blue color, representing fast P-wave perturbations) similar in dip and length to the one seen in the RF image (Figure 2.6a). This dipping structure is not present in the northern part of the VEOX line from the tomography model and previous RF studies in central Mexico (Pérez-Campos et al., 2008; Kim et al., 2010). The grid size that Li et al. (2008) used in the tomographic inversion is approximately 0.7 degrees in latitude and longitude and 45 km in depth. The resolution of the tomographic models is poor at this scale, but they do confirm the existence of the Yucatán slab and that it continues farther to the southeast of the VEOX line (Figure 2.9b). In addition, the recent tomographic

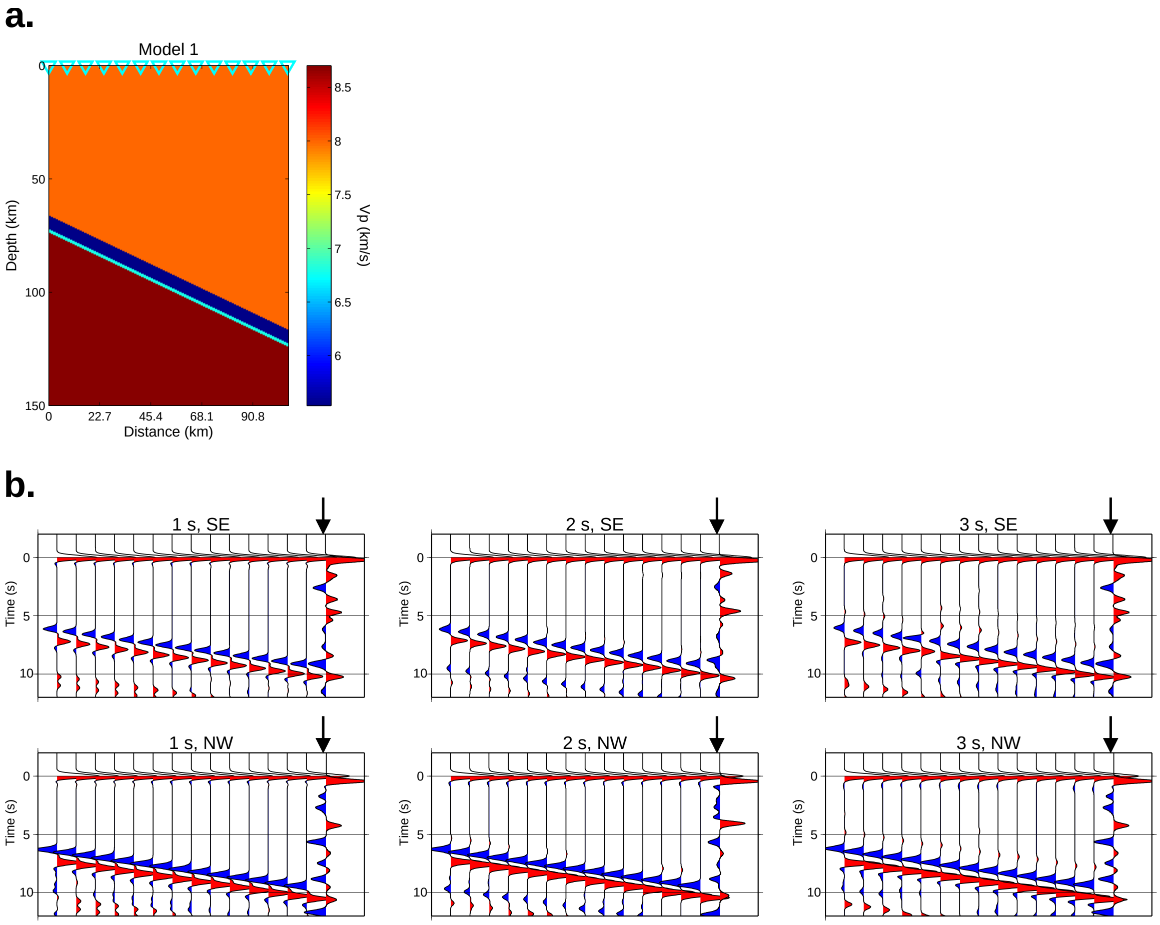

Figure 2.7: RF finite-difference modeling result for the Cocos slab. (a) Geometry of the model, including the Cocos slab with a dip of 25 degrees. We insert two layers with low velocity in the oceanic crust. The top part of the subducting oceanic crust includes very low S-wave velocity based on the analysis by Kim et al. (2010). We note that the estimate of the thickness of the low-velocity layers for the oceanic crust slightly trades off with their velocities. The color represents the P-wave velocity in km/s. (b) The 1 s, 2 s, and 3 s synthetics with two different directions of incoming plane waves (SE or NW) are shown. The red and blue colors represent the positive and negative impedance contrasts, respectively. The data trace included in each record section is indicated by the arrow.

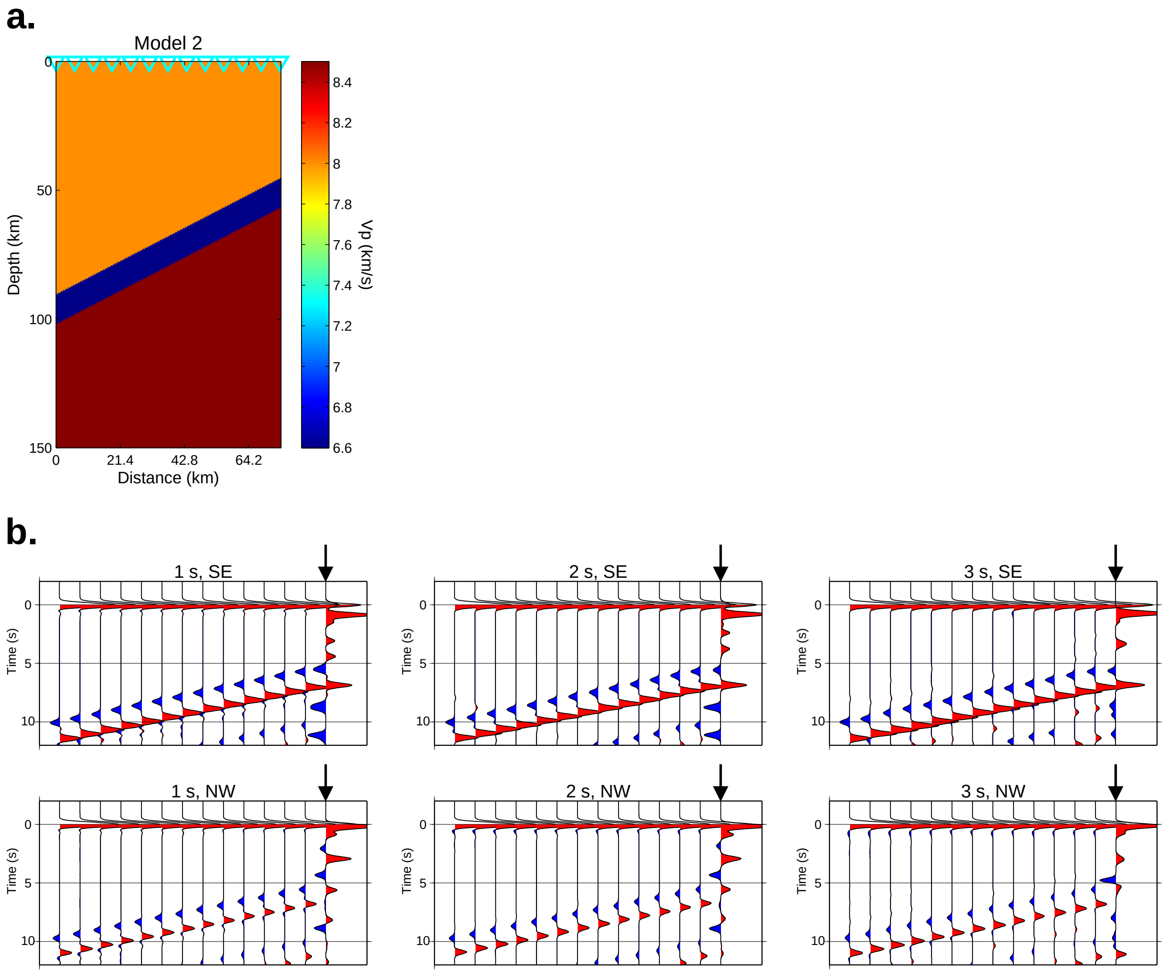

Figure 2.8: RF finite-difference modeling result for Yucatán slab. (a) Geometry of the model, including the Yucatán slab with a dip of 35 degrees. The color represents the P-wave velocity in km/s. (b) RF synthetics from the model shown in a. The 1 s, 2 s, and 3 s synthetics with two different directions of incoming plane waves (SE or NW) are shown. The red and blue colors represent the positive and negative impedance contrasts, respectively. The data trace included in each record section is indicated by the arrow. Note that the ~50% reduction in the converted amplitudes at the top interface of the subducted Yucatán slab in the NW swath compared to ones in the SE swath.

images of P- and S-wave velocities derived from local earthquakes recorded by the VEOX line (Chen & Clayton, 2010) also show the Cocos and Yucatán slabs, although their images are limited to 100 km in depth due to the maximum depth range of the local earthquakes.

The model by Li et al. (2008) also shows that the Cocos slab appears to have broken with the detached portion having descended to about 300 km depth (Figure 2.9b). This evidence of slab truncation along with profiles farther to the southeast was used by Rogers et al. (2002) to argue that the uplift of the highlands in Honduras is due to the inflow of the asthenosphere resulting from the breaking of the slab. Using hypsometry of the uplift in Honduras, the slab detachment is estimated to be ∼10−5 Ma (Rogers et al., 2002). The gap in the slab provides an avenue for the Yucatán slab to cross the Cocos slab, and may indicate that the Yucatán slab is responsible for the truncation.

2.6 Tectonic and Volcanic Features

There are a number of interesting and anomalous tectonic features in southern Mexico that are assumed to be a result of subduction, but are not well explained by a simple model of the Cocos Plate subducting under the NA Plate. The Isthmus of Tehuantepec is an anomalous topographic low above the Cocos subduction zone (Figure 2.1b). To the east, the CFTB is a compressive structure with ∼106 km of shortening that occurred between ∼13 and ∼11 Ma (Mandujano-Velazquez & Keppie, 2009). Both this topographic low and the CFTB shortening have been attributed to subduction of the Tehuantepec Ridge (TR) asperity on the Cocos Plate (Manea et al., 2005; Mandujano-Velazquez & Keppie, 2009). The CFTB is confined to the southern Mexican interior northeast of the Chiapas massif, and the deformation trace may continue eastward into Guatemala (Figure 2.1b). These features of the CFTB appear to depart from deformation that can be attributed to subduction of the TR.

In Figure 2.1a, the currently active volcanoes in the region are shown. In central Mexico, the active arc is along the southern edge of the TMVB where the slab is at ∼100 km depth. In the south, the Central American Volcanic Arc (CAVA, Figure 2.2a) is along the coast, where the slab is also at 100 km depth. In between, the Modern Chiapanecan Volcanic Arc (MCVA, Figure 2.2a) is at a strike of ~30° clockwise from the strike of the MAT and lies ~200 km above the Cocos slab (Manea & Manea, 2008). In this region the Cocos slab, as delineated by seismicity (Rebollar et al., 1999), ranges in dip from 50° to 54°, which is not sufficient to explain the MCVA's oblique strike angle. The volcanoes become progressively older to the south-southeast with initial dates ranging from 1.3 to 3 Ma (Mora et al., 2007), which indicates the system is evolving.

The Miocene Sierra Madre arc (Figure 2.1a) lies along the coast and extinguished at approximately 9−3 Ma (Damon & Montesinos, 1978). A model by Manea & Manea (2008) to explain the MCVA and the extinct Miocene Sierra Madre arc along the coast proposes that the influx of hot mantle wedge material from slab flattening event in central Mexico at 29−19 Ma is the source for the modern volcanism, while the cold (flattened) slab shuts off the Miocene Sierra Madre arc. In the northern part of the Tehuantepec Isthmus, the LTVF is ~7−0 Ma in age and alkaline by affinity (Verma, 2006). If the Cocos slab is projected beneath the LTVF, it would lie ~250 km beneath the LTVF, or deeper if the slab truncation models are correct (Rogers et al., 2002).

El Chichón lies between the MCVA and the LTVF, and is a very young (0.2 Myr) isolated adakite volcano, that may be related to the subduction of the TR (Manea & Manea, 2008). The MCVA, LTVF, and El Chichón volcanism do not appear to be the result of normal Cocos slab dehydration because slab depths are 200 km or deeper below the volcanic centers.

2.7 Discussion

Previous models of Yucatán Block motion and Gulf of Mexico opening since the breakup of Pangea in the Mesozoic seem to provide no explanation for the Yucatán slab structure. Most models suggest that the Yucatán Block rotated in counterclockwise fashion away from the northern Gulf of Mexico margin during the Jurassic (Pindell & Kennan, 2009) (block trajectory shown in Figure 2.10b). Dextral shear zones in eastern Mexico/western Gulf of Mexico accommodated this motion. This motion is compatible with some interpretations of magnetic anomalies in the deep

Gulf of Mexico basin (Hall & Najmuddin, 1994), possible hotspot tracks in the deep Gulf of Mexico basin (Bird et al., 2005), and preferred positions of the Yucatán Block in Pangean reconstructions (e.g., Dickinson, 2009). This interpretation would not be compatible with the Yucatán slab because it does not predict convergence between the Yucatán and the South Mexico Blocks. Also, if the Yucatán slab structure formed during the Jurassic, it seems unlikely that such an old inactive structure would have sufficient buoyancy to remain as shown in Figure 2.6a, and it should have descended into the deeper mantle long ago (Billen, 2008).

Our preferred hypothesis is that the Yucatán slab represents sea floor subducted prior to a collision of the Yucatán Block with southeastern Mexico (Figure 2.10a). Strictly speaking, neither the timing of the proposed collision nor the relative motion of the Yucatán and South Mexico Blocks are constrained by the Yucatán slab structure. However, we speculate on a possible evolutionary model as follows. To accommodate this hypothesis and the Jurassic age of the Gulf of Mexico basin, we suggest that the historical motion of the Yucatán Block took place in two stages. During the opening of the Gulf, a first Jurassic stage involves a clockwise rotation of the Yucatán Block away from the northern Gulf of Mexico coast (Figure 2.10b). The key difference is that we propose this stage finishes with the Yucatán Block placed off the southwest coast of Florida. Then, a second stage, in the Miocene, would involve the southwest migration of the Yucatán Block <250 km (i.e., up to the inferred length of the Yucatán slab) into its current position (Figure 2.10). The late stage would finish with the collision of the Yucatán Block against southeast Mexico and provides an explanation for the formation of the CFTB in southeast Mexico.

In this model, the ∼13−11 Ma age of deformation in the CFTB constrains the timing of continental collision. The model in Figure 2.9a shows the place where the proposed suture zone intersects the surface along the northward projection of the VEOX line. The most prominent lineament to the southeast of this point is the northern edge of the CFTB, marked by the gray A-A arrows in Figure 2.1b. There is a clear lineament in the approximate location where we predict the suture zone should be. It is terminated on its eastern end by the Northern Boundary Fault of the Maya Mountains (Figure 2.1b).

The South Mexico Block appears to have been moving southeastwards relative to the main NA Plate, since the Miocene (Andreani et al., 2008). This has been accommodated by sinistral transtension in the Tula-Chapala fault system (TCFS), roughly parallel to the TMVB (Andreani et al., 2008) (Figure 2.1a). Southeastwards migration of the South Mexico Block may have initiated shortening at its eastern margin. Progressive shortening between the South Mexico and Yucatán Blocks may have evolved into a self-sustaining south-dipping subduction zone, which would account for the inferred southwestwards migration of the Yucatán Block. We prefer a model that incorporates relative southwestwards migration of the Yucatán Block, because we hypothesize that evidence for sufficient extension in the deep water Florida-Yucatán straits is more likely to be found than evidence for sufficient sinistral slip in the TCFS. Our model predicts early- to mid-Miocene extension in the Florida-Yucatán straits between Florida and the Campeche Bank (Figure 2.1a), prior to the formation of the CFTB.

The idea of the Yucatán once being connected to Florida is support by the 30-50 s Rayleigh-wave phase-velocity maps which show that Yucatán and Florida have a velocity that is distinctly faster than the rest of Mexico or the western Gulf region (Gaite et al., 2010). In addition, bathyal sediments of Cretaceous age observed in drill core from the Deep Sea Drilling Project (DSDP) holes 10-94, 10-95, 10-97, 77-535, 77-536, 77-537, 77-540 (Figure 2.1) have been interpreted to indicate a stable basin within the Florida-Yucatán straits throughout the Cenozoic (Buffler et al., 1984; Worzel, 1973). On the other hand, missing intervals of Cenozoic section in these cores indicate significant slumping and mass wasting has occurred since the Miocene. The slumping and mass wasting could simply be due to gravitational instabilities, but may also be compatible with the tectonic extension predicted in our model. The extension does not appear to involve spreading along a ridge, and in this respect it may be similar to the extension that is currently occurring in the northern Gulf of California (Gonzalez-Fernandez et al., 2005). The opening of a deep water channel between the Yucatán Block and Florida may also explain the initiation of the oceanic Loop Current in the eastern Gulf of Mexico in the mid-Miocene (Mullins et al., 1987).

The dynamics of the slab subduction appear to be quite unusual in this region. The Yucatán slab appears to cut off the Cocos slab at $\sim$120 km depth (Figure 2.9a) thus stopping standard 2D mantle-wedge flow for both systems. It is almost certain

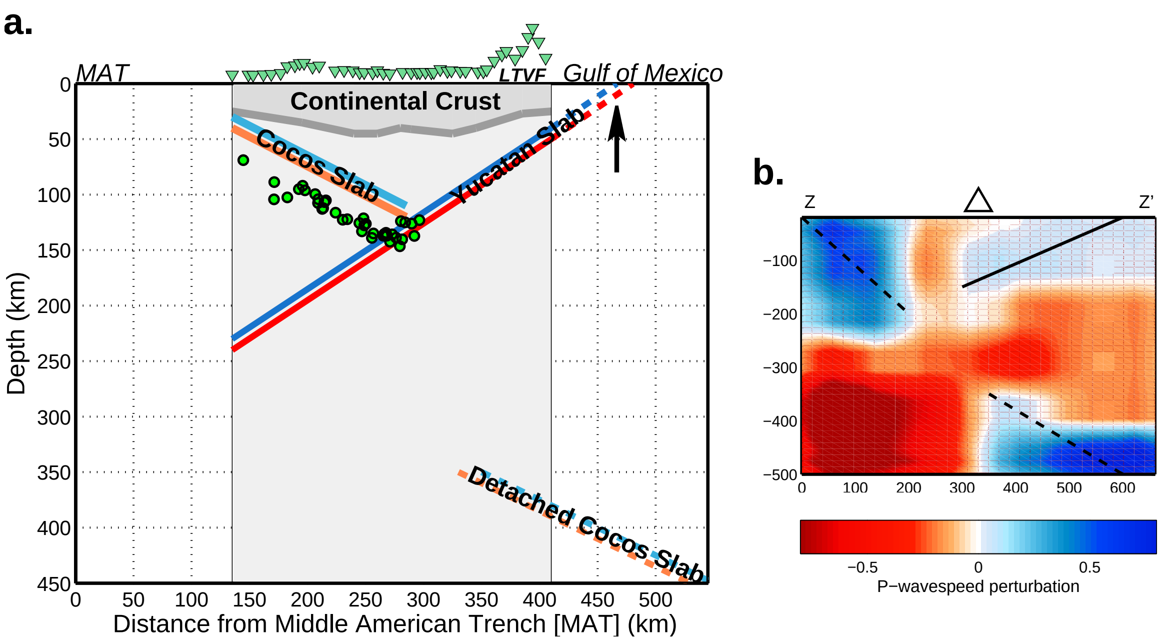

Figure 2.9: The model showing the structures constrained by the RF and tomography results. (a) The composite model showing the structures along the VEOX line, based on the RFs and global tomographic image by Li et al. (2008). The structures down to a depth of 250 km are constrained by the RFs, and the location of the detached slab is from the global P-wave tomographic image. The local earthquakes plotted as green circles are the same ones in Figures 2.4c and 2.5a. The black arrow indicates the location of the proposed suture zone. The green triangles show stations indicating relative elevations. (b) Cross section image of the profile Z-Z′ (Figure 2.1) through the tomography model of Li et al. (2008). The Cocos slab is indicated by dotted lines, and the Yucatán slab by the solid line. The profile crosses the active El Chichón volcano (triangle symbol).

that the 3D flow is important in this region, and this may explain the unusual configuration of the arc volcanism in southern Mexico. A poorly understood mechanism involving competition between the Cocos slab and the Yucatán slab may be related to the proposed detachment of the Cocos slab at ∼10−5 Ma (Rogers et al., 2002). The truncation of the Cocos slab would need to have occurred near the Pacific ocean trench in order to put the leading edge of the present Cocos slab at a depth of about 120 km as interpreted in Figure 2.4a.

2.8 Conclusions

The RF image along the VEOX line in southern Mexico reveals the presence of the south-dipping structure (Yucatán slab) that descends to 250 km depth. The extent

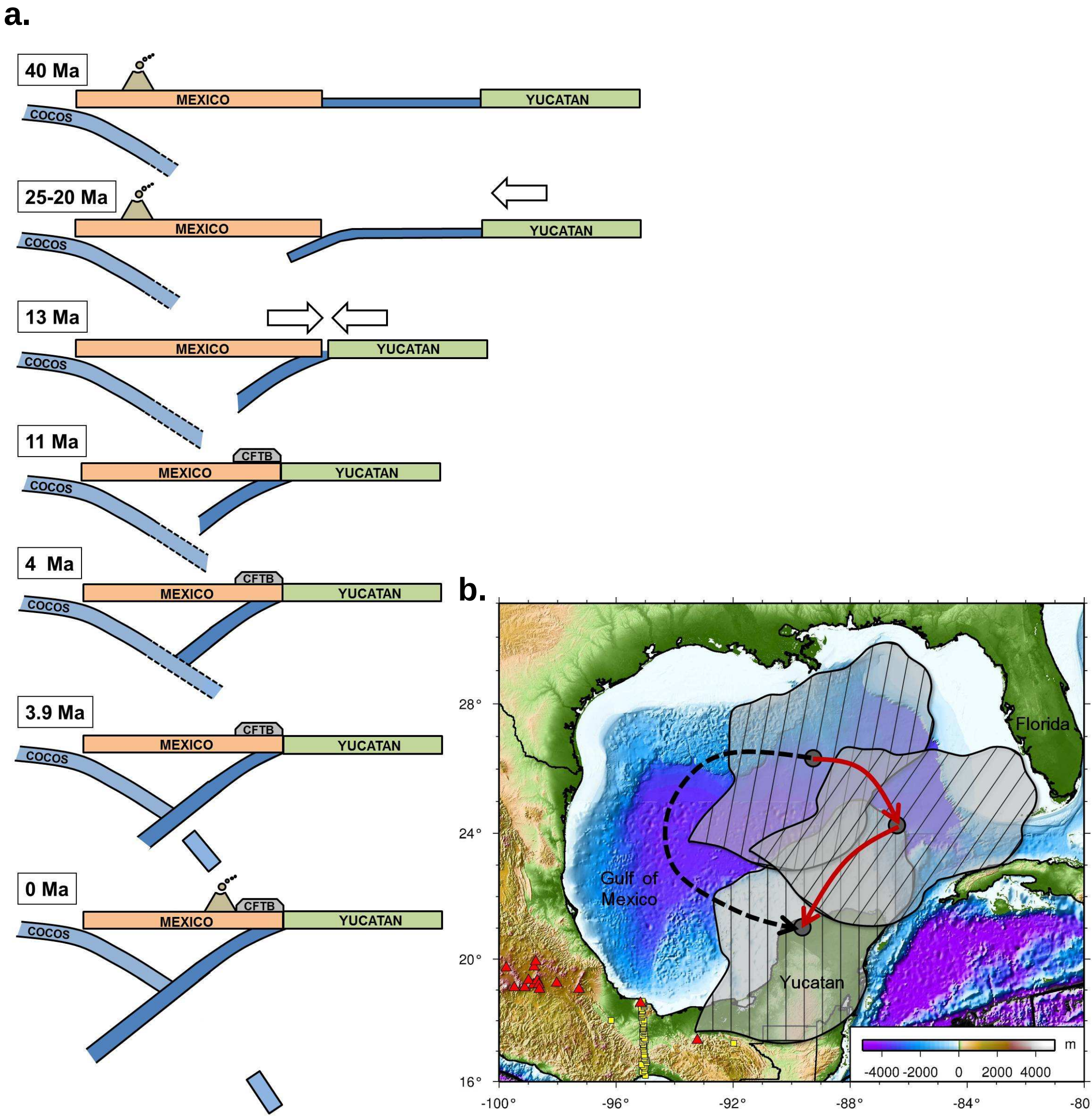

Figure 2.10: Tectonic reconstruction diagram for southern Mexico. (a) A schematic model showing the collision of the Yucatán in Mexico. The onset of subduction (25−20 Ma) is estimated assuming a subduction rate of 2−5 cm/yr and a slab length of 250 km. The date of truncation of the Cocos slab is taken from Rogers et al. (2002). The volcanism is extinguished at the Miocene arc due to the collision, and reappears after 3 Ma (Manea & Manea, 2008). The last stage at 0 Ma shows a present-day model for southern Mexico, and the volcano symbol indicates the MCVA. It is also directly analogous to Figure 2.9b. (b) Map view of the Yucatán Block rotations. The black dotted-line arrow represents the counter-clockwise movement of the Yucatán Block based on the standard model by Pindell & Kennan (2009). The red solid-line arrow represents our proposed model.

of this structure to the southeast is primarily supported by the receiver functions and tomographic images. A model with the Yucatán Block colliding with Mexico in the Miocene can explain the anomalous structures in the region. The proposed suture zone of this collision is the Chiapas Fold and Thrust Belt.

Bibliography

Ammon, C. J., Randall, G. E., & Zandt, G., 1990. On the nonuniqueness of receiver function inversions, *J. Geophys. Res.*, **95**(B10), 15303–15318.

Andreani, L., Rangin, C., Martínez-Reyes, J., Le Roy, C., Aranda-García, M., Le Pichon, X., & Peterson-Rodriguez, R., 2008. The Neogene Veracruz fault: Evidences for left-lateral slip along the southern Mexico block, *Bull. Soc. géol. Fr.*, **179**(2), 195–208.

Billen, M. I., 2008. Modeling the Dynamics of Subducting Slabs, *Annu. Rev. Earth Planet. Sci.*, **36**(1), 325–356.

Bird, D. E., Burke, K., Hall, S. A., & Casey, J. F., 2005. Gulf of Mexico tectonic history: Hotspot tracks, crustal boundaries, and early salt distribution, *Am. Assoc. Pet. Geol. Bull.*, **89**(3), 311–328.

Buffler, R. T., Schlager, W., & Pisciotto, K. A., 1984. *Initial Reports of the Deep Sea Drilling Project Leg 77*, pp. 5–22.

Burbach, G. V., Frohlich, C., Pennington, W. D., & Matumoto, T., 1984. Seismicity and Tectonics of the Subducted Cocos Plate, *J. Geophys. Res.*, **89**(B9), 7719–7735.

Campillo, M., Singh, S. K., Shapiro, N., Pacheco, J., & Hermann, R. B., 1996. Crustal structure of the Mexican volcanic belt based on group velocity dispersion, *Geofis. Int.*, **35**, 361–370.

Castro Artola, O. A., 2010. *Caracterizacion de la geometria de la zona benioff con una red densa de banda ancha en el istmo de tehuantepec*, Ba thesis, Universidad Nacional Autónoma de México.

Chen, T. & Clayton, R. W., 2010. Three-dimensional attenuation and velocity structure of the Cocos subduction zone in Mexico, *Abstract DI31A-1943 presented at 2010 Fall Meeting, AGU, San Francisco, Calif., 13–17 Dec.*

Damon, P. E. & Montesinos, E., 1978. Late Cenozoic volcanism and metallogenesis over an active Benioff zone in Chiapas, Mexico, *Arizona Geol. Soc. Digest*, **X1**, 155–168.

Dickinson, W. R., 2009. The Gulf of Mexico and the southern margin of Laurentia, *Geology*, **37**, 479–481.

Ferrari, L., 2004. Slab detachment control on mafic volcanic pulse and mantle heterogeneity in central Mexico, *Geology*, **32**(1), 77–80.

Gaite, B., Villaseñor, A., Herraiz, M., Iglesias, A., & Pacheco, J. F., 2010. Ambient noise surface wave tomography in Mexico, Gulf of Mexico and Central America, *Abstract S23B-06 presented at 2010 Fall Meeting, AGU, San Francisco, Calif., 13–17 Dec.*

Gonzalez-Fernandez, A., Danobeita, J. J., Delgado-Argote, L. A., Michaud, F., Cordoba, D., & Bartolome, R., 2005. Mode of extension and rifting history of the upper Tiburon and upper Delfin basins, northern Gulf of California, *J. Geophys. Res.*, **110**(B01313), 1–17.

Gorbatov, A. & Fukao, Y., 2005. Tomographic search for missing link between the ancient Farallon subduction and the present Cocos subduction, *Geophys. J. Int.*, **160**(3), 849–854.

Hall, S. A. & Najmuddin, I. J., 1994. Constraints on the tectonic development of the eastern Gulf of Mexico provided by magnetic anomaly data, *J. Geophys. Res.*, **99**(B4), 7161–7175.

Kennett, B. L. N. & Engdahl, E. R., 1991. Traveltimes for global earthquake location and phase identification, *Geophys. J. Int.*, **105**(2), 429–465.

Kikuchi, M. & Kanamori, H., 1982. Inversion of complex body waves, *Bull. Seism. Soc. Am.*, **72**(3), 491–506.

Kim, Y., Clayton, R. W., & Jackson, J. M., 2010. Geometry and seismic properties of the subducting Cocos plate in central Mexico, *J. Geophys. Res.*, **115**(B6), 1–22.

Langston, C. A., 1979. Structure under Mount Rainier, Washington, inferred from teleseismic body waves, *J. Geophys. Res.*, **84**(B9), 4749–4762.

Li, C., van der Hilst, R. D., Engdahl, E. R., & Burdick, S., 2008. A new global model for P wave speed variations in Earth's mantle, *Geochem. Geophys. Geosyst.*, **9**(5), 1–21.

Ligorria, J. P. & Ammon, C. J., 1999. Iterative deconvolution and receiver-function estimation, *Bull. Seism. Soc. Am.*, **89**(5), 1395–1400.

Mandujano-Velazquez, J. & Keppie, J. D., 2009. Middle Miocene Chiapas fold and thrust belt of Mexico: a result of collision of the Tehuantepec Transform/Ridge with the Middle America Trench, *Geol. Soc. Spec. Publ.*, **327**, 55–69.

Manea, M. & Manea, V. C., 2008. On the origin of El Chichón volcano and subduction of Tehuantepec Ridge: A geodynamical perspective, *J. Volcanol. Geotherm. Res.*, **175**(4), 459–471.

Manea, M., Manea, V., Ferrari, L., Kostoglodov, V., & Bandy, W., 2005. Tectonic evolution of the Tehuantepec Ridge, *Earth Planet. Sci. Lett.*, **238**(1-2), 64–77.

Marton, G. & Buffler, R. T., 1994. Jurassic reconstruction of the Gulf of Mexico Basin, *Int. Geol. Rev.*, **36**, 545–586.

Melgar, D., 2009. *El proceso de subducción en la zona del Istmo de Tehuantepec a partir de funciones receptor*, Phd thesis, Universidad Nacional Autónoma de México.

Melgar, D. & Pérez-Campos, X., 2010. Imaging the Moho and Subducted Oceanic Crust at the Isthmus of Tehuantepec, Mexico, from Receiver Functions, *Pure Appl. Geophys.*, pp. 1–12.

Mora, J., Jaimes-Viera, M., Garduño Monroy, V., Layer, P., Pompa-Mera, V., & Godinez, M., 2007. Geology and geochemistry characteristics of the Chiapanecan

Volcanic Arc (Central Area), Chiapas Mexico, *J. Volcanol. Geotherm. Res.*, **162**, 43–72.

Mullins, H., Gardulski, A., Wise, S., & Applegate, J., 1987. Middle Miocene oceanographic event in the eastern Gulf of Mexico: Implication for seismic stratigraphic succession and Loop Current/Gulf Stream circulation, *Geol. Soc. Am. Bull.*, **98**, 702–713.

Pardo, M. & Suárez, G., 1995. Shape of the subducted Rivera and Cocos plates in southern Mexico: Seismic and tectonic implications, *J. Geophys. Res.*, **100**(B7), 12357–12373.

Pérez-Campos, X., Kim, Y., Husker, A., Davis, P. M., Clayton, R. W., Iglesias, A., Pacheco, J. F., Singh, S. K., Manea, V. C., & Gurnis, M., 2008. Horizontal subduction and truncation of the Cocos Plate beneath central Mexico, *Geophys. Res. Lett.*, **35**(18), 1–6.

Pindell, J. & Dewey, J. F., 1982. Permo-Triassic reconstruction of western Pangea and the evolution of the Gulf of Mexico/Caribbean region, *Tectonics*, **1**(2), 179–211.

Pindell, J. & Kennan, L., 2009. Tectonic evolution of the Gulf of Mexico, Caribbean and northern South America in the mantle reference frame: An update, *Geol. Soc. Lond. Spec. Publ.*, **328**(2009), 1–55.

Rebollar, C. J., Espíndola, V. H., Uribe, A., Mendoza, A., & Pérez-Vertti, A., 1999. Distributions of stresses and geometry of the Wadati-Benioff zone under Chiapas, Mexico, *Geofis. Int.*, **38**, 95–106.

Rogers, R., Karason, H., & van der Hilst, R. D., 2002. Epeirogenic uplift above a detached slab in northern Central America, *Geology*, **30**(11), 1031–1034.

Savage, M. K., 1998. Lower crustal anisotropy or dipping boundaries? Effects on receiver functions and a case study in New Zealand, *J. Geophys. Res.*, **103**, 15069–15087.

Syracuse, E. M. & Abers, G. A., 2006. Global compilation of variations in slab depth beneath arc volcanoes and implications, *Geochem. Geophys. Geosyst.*, **7**(5), 1–18.

Verma, S. P., 2006. Extension-related origin of magmas from a garnet-bearing source in the Los Tuxtlas volcanic field, Mexico, *Int. J. Earth Sci.*, **95**, 871–901.

Vinnik, L. P., 1977. Detection of waves converted from P to SV in the mantle, *Phys. Earth Planet. Inter.*, **15**, 39–45.

Waldhauser, F. & Ellsworth, W. L., 2000. A Double-Difference Earthquake Location Algorithm: Method and Application to the Northern Hayward Fault, California, *Bull. Seism. Soc. Am.*, **90**(6), 1353–1368.

Worzel, J. L., 1973. *Initial Reports of the Deep Sea Drilling Project Leg 10*, vol. 25, pp. 3–6.

Zamora-Camacho, A., Espindola, V. H., Pacheco, J. F., Espindola, J. M., & Godinez, M. L., 2010. Crustal thickness at the Tuxtla Volcanic Field (Veracruz, Mexico) from receiver functions, *Phys. Earth Planet. Inter.*, **182**(1-2), 1–9.

Zarifi, Z., Havskov, J., & Hanyga, A., 2007. An insight into the Bucaramanga nest, *Tectonophysics*, **443**(1-2), 93–105.

Zhu, L. & Kanamori, H., 2000. Moho depth variation in southern California from teleseismic receiver functions, *J. Geophys. Res.*, **105**(B2), 2969–2980.

Chapter 3

Distribution of Hydrous Minerals in the Cocos Oceanic Crust, Mexico

Abstract

Teleseismic converted phases are used to estimate the mineralogy of the downgoing oceanic crust as a function of depth along the Cocos slab in central and southern Mexico. The upper part of the oceanic crust includes a thin low-velocity layer of a thickness of 4±1 km, which has much lower seismic velocities than lower (normal) crust. Using Vp/Vs as a function of S wave velocity (Vs) in a range of likely pressures and temperatures for candidate hydrous/anhydrous phases, we determine candidate hydrous mantle mineral assemblages, which can explain the low seismic velocity anomaly in both upper and lower oceanic crusts underneath Mexico. In central Mexico, the compositions of the steeply subducting oceanic crust, enriched with lawsonite and zoisite, transitions into gabbroic and eclogitic assemblages at ∼100 km, which supports the arc volcanism at the Trans-Mexican Volcanic Belt directly above the slab as well as the slab rollback. Whereas, the dominant mineral phase in the upper oceanic crust of southern Mexico is amphibole on top of unaltered gabbroic oceanic crust. The difference in mineral assemblages of the subducted oceanic crust may help explain the difference in slab geometries between central and southern Mexico.

3.1 Introduction

The presence of hydrous minerals in the oceanic crust reduces the seismic velocity to considerably less than the velocity of the surrounding mantle according to laboratory measurements on candidate phases (e.g., Jacobsen & van der Lee, 2006). As oceanic plates subduct, mineral-bound H_2O is transported down into the deep mantle (Abers, 2000; Hacker et al., 2003; Jacobsen & van der Lee, 2006; Maruyama & Okamoto, 2007; Mainprice & IIdefonse, 2009). The evidence has been seismically detected in various subduction environments as a low-velocity layer atop of the subducting plate (e.g, Alaska (Rondenay et al., 2008), Cascadia (Nicholson et al., 2005; Audet et al., 2009), Central Andes (Yuan et al., 2000), and northeast Japan (Kawakatsu & Watada, 2007; Tsuji et al., 2008)).

The receiver function (RF) images based on teleseismic P-to-S converted phases for central and southern Mexico show a thin low-velocity layer (much lower than normal oceanic crustal velocities) on top of the subducting oceanic lithosphere (Pérez-Campos et al., 2008; Kim et al., 2010; Melgar & Pérez-Campos, 2010). In central Mexico, the finite-difference (FD) modeling of the RFs for the shallow-to-flat slab region (∼45 km depth) suggested anomalously low S wave velocity (Vs) of 2.4-3.4 km/s (Kim et al., 2010). Similar velocities were also obtained by modeling local converted S-to-P phases and teleseismic underside reflections (Song et al., 2009). Kim et al. (2010) suggested that the presence of fluid and hydrous minerals or high pore pressure might explain such a low-velocity anomaly in the upper part of the oceanic crust. The evidence of high H_2O content within the upper oceanic crust may explain the top (horizontal) interface of the Cocos plate for 200 km without strong coupling between two plates during the slab flattening process since ∼20 Ma (Nieto-Samaniego et al., 2006; Morán-Zenteno et al., 2007). This could also be an explanation for the nonvolcanic tremor activity (Payero et al., 2008) and slow slip events (Larson et al., 2007; Vergnolle et al., 2010) in the subducted oceanic crust and the overlying crust. Recent studies suggest strong correlations between episodic tremor and slip (ETS) events and a low-velocity layer at the top of the subducting oceanic crust (Abers et al., 2009; Song et al., 2009; Audet et al., 2010).

Hydrous minerals initially form within oceanic lithosphere as a result of hydrothermal circulation and alteration at spreading ridges, along fracture zones, and along faults in the region of the trench and outer rise (Maruyama & Okamoto, 2007; Audet et al., 2009). However, there is little constraint on in situ abundance and distribution of hydration in the fluid and minerals within subducting crust to fully assess the strength of the plate interface and nature of seismogenesis. Also, experimental measurements of expected seismic wave speeds and anisotropy of the hydrous minerals in the subducted oceanic crust under different pressure (P) and temperature (T) conditions are limited, although progress has been made (Jacobsen & van der Lee, 2006). Nevertheless, knowledge of the material properties (seismic velocities and densities) of mineral phase assemblages along with appropriate phase equilibria are important in interpretation of geophysical observations and geodynamic simulations.

The RFs were previously used to estimate the mineralogy of the subducted oceanic crust as a function of depth (∼20 km to 45 km) along the Cocos slab in central Mexico (Kim et al., 2010). The amplitudes of the distinct negative/positive signature of the RF pulses from the top and bottom interfaces of the oceanic crust were used to constrain the Vs and density of the upper and lower oceanic crusts (Kim et al., 2010). Inverted Vs in the upper oceanic crust with a thickness of 4±1 km are anomalously low, and a low-pressure mineral phase such as talc (low-strength hydrous mineral) is considered a candidate for such an anomaly (Kim et al., 2010). The data for the lower oceanic crust suggested the presence of unaltered (MORB-like) oceanic crustal compositions over the dry-depleted mantle rock (Kim et al., 2010). High-pressure hydrous phases such as Fe-bearing phase A and depleted mantle rocks (pyroxenite and harzburgite) were characterized by higher Vs values than the lower crustal data (Kim et al., 2010). A similar assessment was previously done at the Chile-Argentina flat slab region using velocities derived from the tomography to determine candidate mantle mineral phases (Wagner et al., 2008). A low Vp/Vs ratio, ranging from 1.6 to 1.74, (along with high Vs), over the flat slab region suggested orthopyroxene enrichment in the continental lithosphere above the flat slab (Wagner et al., 2008).

In this study, we extend the analysis to further examine the seismic and mineralogical properties of steeply and shallowly dipping oceanic crust in central and southern Mexico, respectively. Our study region in central Mexico (265−350 km from the trench) largely covers the Quaternary Chichináutzin Volcanic Field, which is part of the subduction-related TMVB and contains numerous cinder cones and shield volcanoes as well as larger stratovolcanoes such as the active Popocatépetl (Figure 3.1) (Cervantes & Wallace, 2003; Johnson et al., 2009). By contrast, the study region in southern Mexico does not include an active volcanic arc, and the notable tectonic feature in the area is the Tehuantepec ridge subducting underneath the continent. On the basis of our inferred mineralogy for central and southern Mexico from the RF amplitude inversion, we attempt to compare the differences in the slab properties betweeen central and southern Mexico.

3.2 Geometries of the Subducted Cocos Oceanic Crust in Mexico

Two passive seismic experiments were carried out in central and southern Mexico to image the structure of the subducting Cocos plate and to investigate different subduction processes along the Middle America Trench (MAT). Approximately two years of broadband seismic data from the Meso-American Subduction Experiment (MASE) line in central Mexico and Veracruz-Oaxaca (VEOX) line in southern Mexico (Figure 3.1) were collected and processed to compute receiver functions (RFs) based on teleseismic P-to-S conversions. The subducted Cocos plate beneath central Mexico, as imaged with the RFs from the MASE line, dips shallowly (∼15°) near Acapulco on the Pacific coast (Figure 3.1) and then tectonically underplates the continental crust for a distance of approximately 300 km from the MAT (Pérez-Campos et al., 2008; Kim et al., 2010). After the flat segment, the Cocos plate is imaged to be subducting steeply (∼75°) underneath the Trans-Mexican Volcanic Belt (TMVB) from P wave tomography (Husker & Davis, 2009) and RF migration (Kim et al., 2010). Since ∼20 Ma, the Cocos plate may be rolling back as evidenced by the southward migration of TMVB volcanism (Ferrari, 2004). In contrast, the RF image across the VEOX line in southern Mexico shows the Cocos slab dipping ∼25° to a depth of ∼120 km (Melgar & Pérez-Campos, 2010).

Teleseismic waveforms from earthquakes with magnitude greater than 6.1, and epicentral distances between 30° and 90°, were collected and then band-passed from

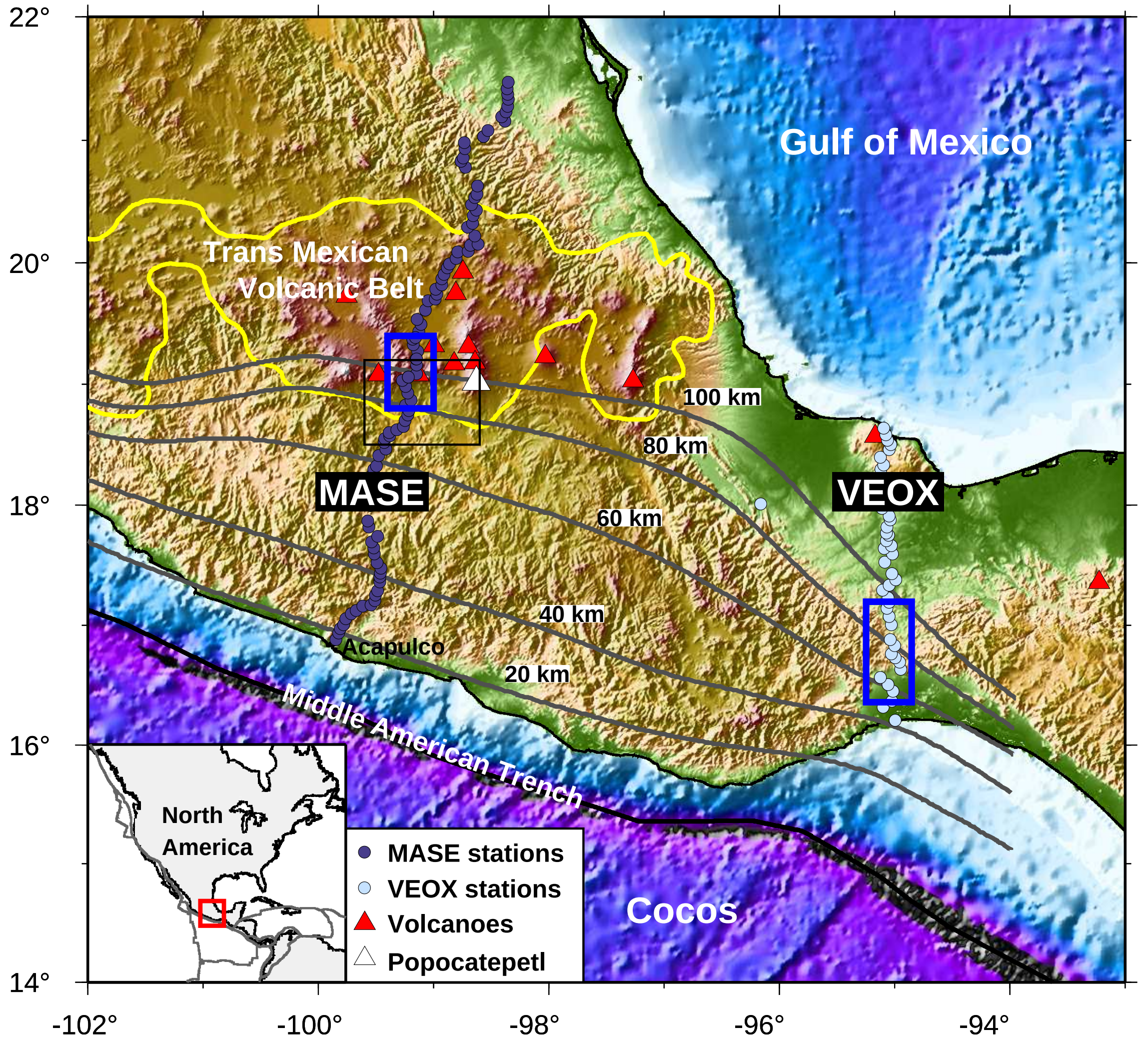

Figure 3.1: Location of the arrays in central and southern Mexico. MASE in central Mexico consists of 100 broadband stations with inter-station distance of about 6 km, and VEOX in southern Mexico of 45 stations with similar inter-station distance. Gray lines depict isodepth contours of the subducted Cocos plate beneath the North American plate based on local seismicity (Pardo & Suárez, 1995). The regions of the focus are included in blue boxes. The black box outlines the Chichináutzin Volcanic Field in central Mexico (Johnson et al., 2009).

0.01 to 1 Hz. For this study, 28 events recorded on 8 stations in central Mexico from 06/2005 to 02/2007 and 43 events from 12 stations in southern Mexico from 08/2007 to 10/2008 are used to compute the RFs. The smaller dataset for MASE reflects difficulties in picking phases corresponding to the top and bottom of the oceanic crust in the steeply dipping geometry (Figure 3.2) from only eight stations above the TMVB. We note that the first two VEOX stations at the Pacific coast (Figure 3.1), which sample the Cocos oceanic crust at 35−45 km depth, are not included in the analysis because their seismic responses were heavily affected by frequent flooding events during the experiment. Individual waveform data are time-windowed to 90 s and rotated to radial and tangential coordinates. We then use the iterative time-domain deconvolution technique (Kikuchi & Kanamori, 1982; Ligorria & Ammon, 1999) to compute the RFs. We measure amplitudes of the negative and positive RF pulses at the interfaces of top and bottom of oceanic crusts in our study regions (Figure 3.2). The collection of the RF amplitudes for each station is used for the inversion which we describe in the following section.

3.3 Bayesian Inversion of Receiver Function Amplitude

For the inversion, we use the linearized Zoeppritz equation, which describes the elastic, plane wave transmission coefficients between two half-spaces (Aki & Richards, 2002) for small incidence angles. The P-to-S transmission coefficient T^{PS} depends only on Vs and density variations, and based on the small angle approximation ($p^2 \rightarrow 0$) it can be simplified as

$$T^{PS} = \frac{p\alpha}{2}\left[\left(1 - \frac{2\beta}{\alpha}\right)\frac{\Delta\rho}{\rho} - \frac{4\beta}{\alpha}\frac{\Delta\beta}{\beta}\right], \tag{3.1}$$

where p represents the ray parameter, α the P wave velocity, β the S wave velocity, and ρ the density. The inversion capability is demonstrated for the shallow to flat oceanic crust in central Mexico ($\sim$20−45 km depth). Kim et al. (2010) used a single optimum reference velocity model for α, β, and ρ in equation (3.1), primarily constrained by

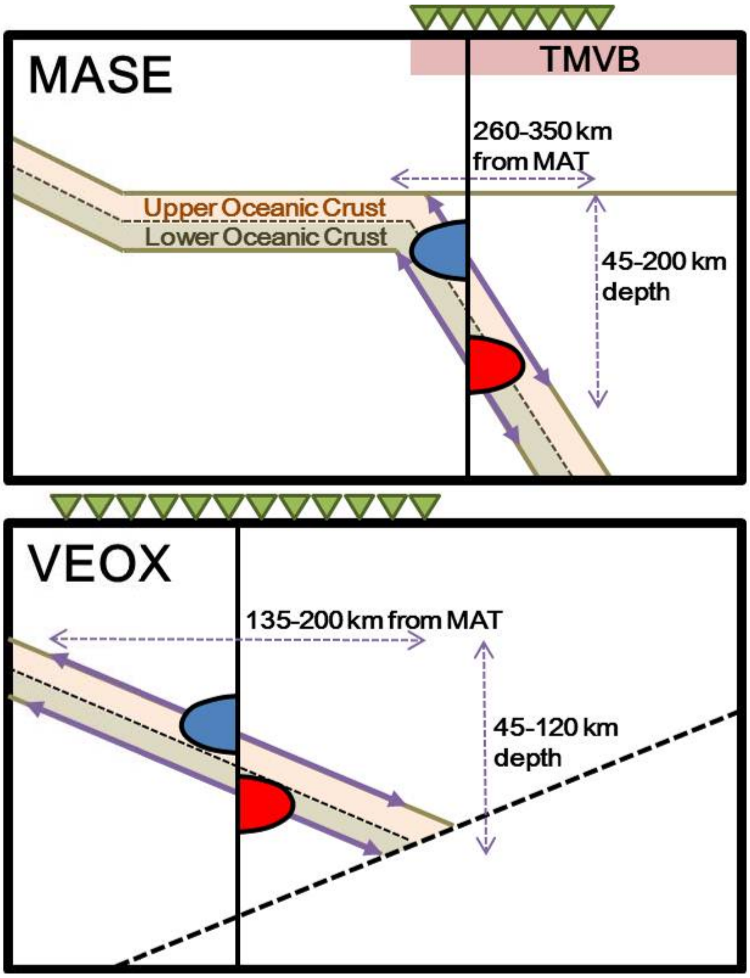

Figure 3.2: Geometry of the oceanic crust in central (top) and southern (bottom) Mexico, constrained by the RFs (Pérez-Campos et al., 2008; Kim et al., 2010; Melgar & Pérez-Campos, 2010). The negative and positive RF pulses are sampled from the depth of 45 to 200 km for MASE and 45 to 120 km for VEOX. The P-T ranges for MASE are 1.2−3.5 GPa and 450−1000°C, and for VEOX are 1.2−2.0 GPa and 450−700°C (Manea et al., 2004).

the FD modeling of the RFs and local velocity model by Valdes-Gonzalez & Meyer (1996), and inverted for absolute Vs and densities rather than the perturbations. The detailed analysis of the inversion procedure is described in Kim et al. (2010).

In our analysis, we implement Bayesian sampling in the inversion for Vs and density of the upper and lower oceanic crusts because inverted parameters are highly sensitive to the choice of seismic parameters (α, β, and ρ) of the layer above/below the oceanic crust. In particular, we do not have a well-constrained velocity model that describes the structure beneath the TMVB in central Mexico. The Bayesian sampling is a probabilistic approach that samples models in the solution space proportionally to how consistent the models are with data (likelihood), given certain prediction errors, as well as with the prior information, producing a distribution of possible models (posterior) for the inverse problem (Tarantola, 2005; Minson, 2010). The seismic parameters for the layer above/below the upper/lower oceanic crust (Figure 3.2) are randomly generated from Gaussian distribution curves with given mean and standard deviation parameter. For the mean, we use a value 3% larger than the IASP91 Earth reference model (Kennett & Engdahl, 1991) based on the tomographic model for central Mexico provided by Husker & Davis (2009). The standard deviation is set to 1 km/s. The Bayesian approach yields an estimate of the probability density function of all the possible input parameters, which can then be propagated through the forward model to determine the Vs and densities and their associated uncertainty distributions. We generate 10,000 models for each station to ensure a proper sampling of the Gaussian probability distribution.

3.4 Hydrous Minerals in Dipping Oceanic Crust

Figures 3.3a and 3.3b show the Vp/Vs as a function of the inverted Vs based on the Bayesian sampling of 10,000 possible models for (a) MASE and (b) VEOX. The figures also show candidate phases such as amphibole, lawsonite, zoisite, eclogite, pyroxene and gabbro as ellipses in different color and line properties. The gabbroic rock is computed using the Voigt-Reuss-Hill (VRH) approximation on the combination of 50% plagioclase and 50% pyroxene (Mavko et al., 2003). Predicted seismic velocities for each mineral phase are computed using elastic constants, which most have been previously experimentally determined (see Figure 3.3 caption for details), and third-order finite strain theory (Duffy & Anderson, 1989) for different P-T conditions corresponding to different depths. The P-T ranges for MASE are 1.2−3.5 GPa and 450−1000°C, and for VEOX are 1.2−2.0 GPa and 450−700°C. The P-T information at 45 km, 120 km, and 200 km is taken from a thermal model of the central Mexico subduction zone (Manea et al., 2004). Based on these P-T conditions, candidate minerals and rocks are computed without the presence of a fluid, and the results represent lower-right curvature of each ellipse. Upper-left curvature represents needle-shaped, water-filled cracks with 10% porosity in each mineral or rock, calculated based on the Kuster and Toksöz formulation (Mavko et al., 2003) and appropriate P-T conditions. We note that each ellipse also includes different shape cracks (sphere- and penny-shape). Also, the lower-right area of each ellipse corresponds to high P-T values whereas the upper-right area represents low P-T.

The color contours in Figures 3.3a and 3.3b show amplitudes of the probability distribution functions of the inverted Vs. We determine major mineral phases for the subducted oceanic crust underneath central and southern Mexico according to depths by comparing high-amplitude contours of our inverted values with the computed candidate phases. For both regions, the shallower portion of the oceanic crust corresponds to the higher Vp/Vs ratio (and lower Vs), and the deeper portion corresponds to the lower Vp/Vs ratio (and higher Vs). Also, the high-amplitude patterns between upper and lower oceanic crusts are very similar due to the fact that the input seismic parameters for the layer above/below the upper/lower oceanic crusts are not very different from each other.

In central Mexico, small variances between the peak patterns for the upper and lower oceanic crusts probably mean that the oceanic crust becomes more homogeneous in composition as the depth increases. The major mineral assemblages at 60 to 100 km depth in the upper and lower oceanic crusts underneath central Mexico are zoisite and lawsonite (∼0−5% porosity) (Figure 3.3a). The candidate phases which explain our deeper-depth (>∼100 km) data are gabbro (∼0−4% porosity) and eclogite (∼6% porosity). The eclogitization underneath the TMVB is in good agreement with the slab rollback mode evidenced by the southward migration of the volcanism (Ferrari et al., 2001) and seismic images (Husker & Davis, 2009; Kim et al., 2010). Fluids

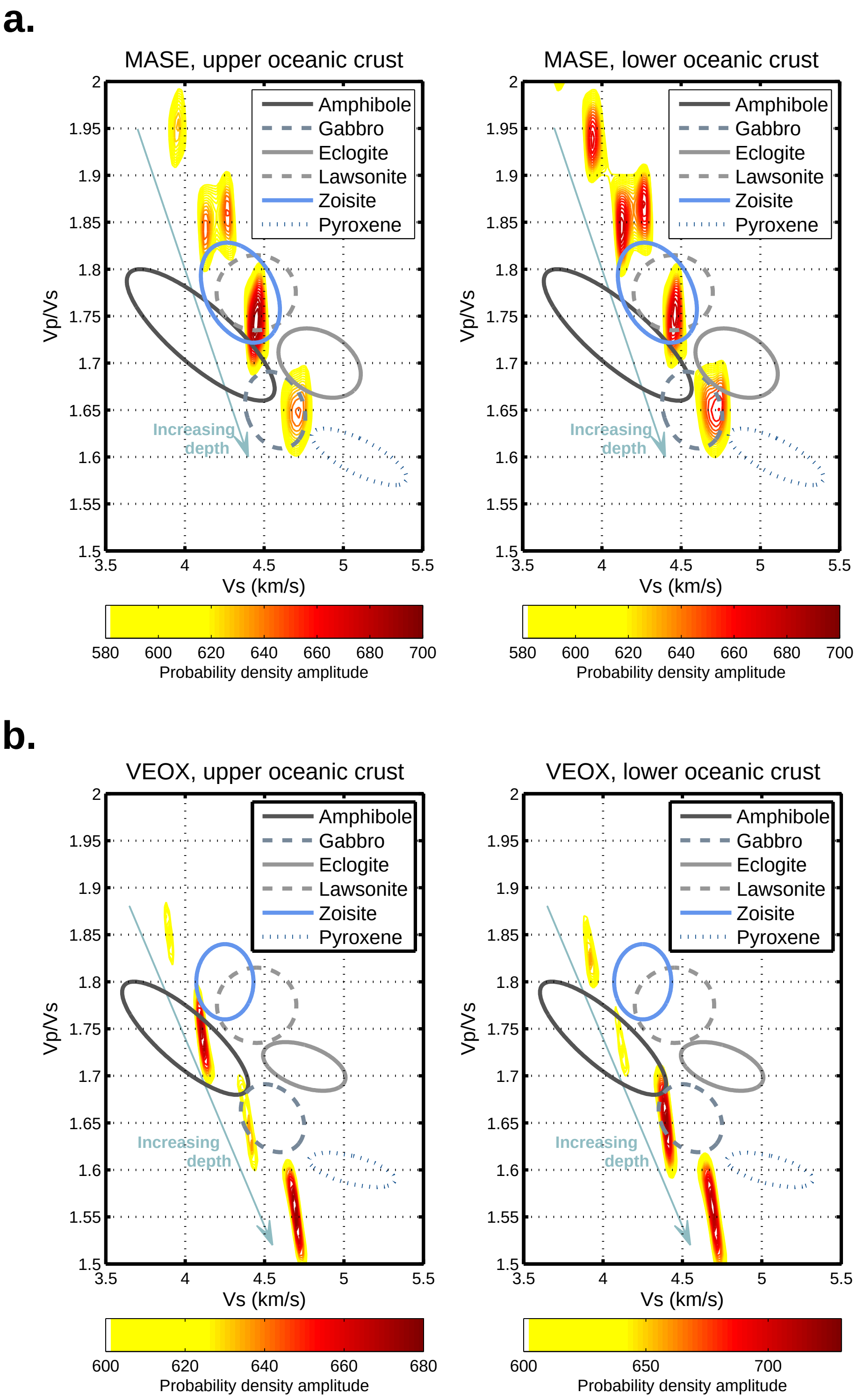

Figure 3.3: Calculated Vp/Vs ratio versus Vs at depth ranges for (a) MASE from 45 km to 200 km and for (b) VEOX from 45 km to 120 km. The colorbar represents probability amplitudes corresponding to all the possible Vs as contours, and we only show high end of the amplitude range in warm colors. The ellipses in cold colors and solid and dotted lines represent candidate mantle mineral and rock properties. The lower-right curvature of each ellipse represents poreless mineral or rock phases, and the upper-left curvature represents the phases with various shape-crack, water-filled inclusions of maximum porosity 0.1. The shallow depth part of the oceanic crust corresponds to the higher Vp/Vs ratio (and lower Vs), and the deeper depth part corresponds to the lower Vp/Vs ratio (and higher Vs). The points for amphibole are obtained from Tatham et al. (2008); gabbro from Christensen (1978), Anderson (1989), and Fei (1995); eclogite from Ringwood & Green (1966), Anderson (1989), Fei (1995), Ghent et al. (2004), and James et al. (2004); lawsonite from Daniel et al. (1999), Scott & William (1999), Grevel et al. (2000), Sinogeikin et al. (2000), and Schilling et al. (2002); zoisite from Holland et al. (1996), Pawley et al. (1996), and Grevel et al. (2000); plagioclase from Askarpour et al. (1993) and Angel (2004); pyroxene from Angel & Jackson (2002).

in pore spaces of the hydrous minerals may explain the anomalous data points at very-shallow depth from 45 to 60 km (lower Vs region).

In southern Mexico, the dominant phase is amphibole ($<\sim$5% porosity) in upper oceanic crust (Figure 3.3b). Lower crustal data suggest dominant gabbroic compositions ($\sim$10% porosity) (Figure 3.3b). Based on this anaysis, we note that the gabbro-to-eclogite transformation has not occurred in southern Mexico. As a comparison, Cascadia, the youngest and warmest slab in the world (Hyndman & Wang, 1993), has the formation of nearly anhydrous eclogite at 80-90 km (Hacker et al., 2003).

The probability distributions of the inverted densities for both central and southern Mexico show rather broad distributions of values between $3200-3400$ kg/m^3 without any distinct peak. Kim et al. (2010) discussed that the inversion is more sensitive to the perturbation in Vs rather than density. Therefore, density is not as good of an indicator to distinguish the mineralogy from this data set.

3.5 Conclusions

We apply the inversion technique using the receiver function (RF) amplitudes to obtain the S wave velocity (Vs) and density of the subducted oceanic crust in central and southern Mexico. Because inverted Vs and density are highly sensitive to the input reference model, we approach the inverse problem from a Bayesian perspective, allowing us to completely characterize the model parameter space by computing allowable models instead of seeking a single optimum model. The resulting probability distribution of the inverted Vs is then used to provide tighter constraints on the physical properties of the subducted Cocos oceanic crust and to explain the difference in slab geometries between central and southern Mexico from a mineral physics perspective.

In central Mexico, the compositions of the more steeply subducting oceanic crust, enriched with lawsonite and zoisite, transitions into gabbro and eclogite phases at $\sim$100 km depth. This result fully supports arc volcanism at the Trans-Mexican Volcanic Belt (TMVB) directly above the slab as well as the slab rollback. In particular, the release of H_2O by slab dehydration could be in the form of a fluid phase or could lower the melting temperature of surrounding phases, where either scenario correlates well with arc volcanism. On the other hand, the dominant mineral phase in the upper oceanic crust of southern Mexico is suggested to be amphibole on top of unaltered gabbroic oceanic crust. We note that both regions contain seismic observations that do not fully match the candidate phases (Figures 3.3a and 3.3b). Fluids in pore spaces, phase transitions, and seismic anisotropy of these assemblages may explain anomalous distributions.

Bibliography

Abers, G. A., 2000. Hydrated subducted crust at 100−250 km depth, *Earth Planet. Sci. Lett.*, **176**, 323–330.

Abers, G. A., MacKenzie, L. S., Rondenay, S., Zhang, Z., Wech, A. G., & Creager, K. C., 2009. Imaging the source region of Cascadia tremor and intermediate-depth earthquakes, *Geology*, **37**, 1119–1122.

Aki, K. & Richards, P. G., 2002. *Quantitative Seismology, 2nd ed.*, University Science Books, Sausalito, California.

Anderson, D. L., 1989. *Theory of the Earth*, Blackwell Scientific Publications.

Angel, R. J., 2004. Equations of state of Plagioclase Feldspars, *Contrib. Mineral Petrol.*, **146**, 506–512.

Angel, R. J. & Jackson, J. M., 2002. Elasticity and equation of state orthoenstatite, $MgSiOi_3$, *Amer. Mineral.*, **87**, 558–561.

Askarpour, V. M., Manghnani, H., & Richet, P., 1993. Elastic properties of diopside, anorthite, and grossular glasses and liquids: a brillouin scattering study up to 1400K, *J. Geophys. Res.*, **98**(B10), 17683–17689.

Audet, P., Bostock, M. G., Christensen, N. I., & Peacock, S. M., 2009. Seismic evidence for overpressured subducted oceanic crust and megathrust fault sealing, *Nature*, **457**, 76–78.

Audet, P., Bostock, M. G., Boyarko, D. C., & Brudzinski, M. R., 2010. Slab morphology in the Cascadia fore arc and its relation to episodic tremor and slip, *J. Geophys. Res.*, **115**(B00A16), 1–15.

Cervantes, P. & Wallace, P. J., 2003. Role of H_2O in subduction-zone magmatism: New insights from melt inclusions in high-Mg basalts from central Mexico, *Geology*, **31**, 235–238.

Christensen, N. I., 1978. Ophiolites, seismic velocities and oceanic crustal structure, *Tectonophysics*, **47**, 131–157.

Daniel, I., Fiquet, G., Gillet, P., Schmidt, M. W., & Hanfland, M., 1999. P-V-T equation of state of lawsonite, *Phys. Chem. Minerals*, **26**, 406–414.

Duffy, T. S. & Anderson, D. L., 1989. Seismic velocities in mantle minerals and the mineralogy of the upper mantle, *J. Geophys. Res.*, **94**(B2), 1895–1912.

Fei, Y., 1995. *Thermal Expansion. In: Ahrens, T. J. (Ed.) Mineral Physics and Crystallography: A Handbook of Physical Constants*, American Geophysical Union, Washington, DC.

Ferrari, L., 2004. Slab detachment control on mafic volcanic pulse and mantle heterogeneity in central Mexico, *Geology*, **32**(1), 77–80.

Ferrari, L., Petrone, C. M., & Francalanci, L., 2001. Generation of oceanic-island basalt-type volcanism in the western TransMexican volcanic belt by slab rollback, asthenosphere infiltration, and variable flux melting, *Geology*, **29**(6), 507–510.

Ghent, E. D., Dipple, G. M., & Russel, J. K., 2004. Thermodynamic models for eclogitic mantle lithosphere, *Earth Planet. Sci. Lett.*, **218**, 451–462.

Grevel, K.-D., Nowlan, E. U., Fasshauer, D. W., & Burchard, M., 2000. In situ X-ray diffraction investigation of lawsonite and zoisite at high pressures and temperatures, *Amer. Mineral.*, **85**, 206–216.

Hacker, B. R., Peacock, S. M., Abers, G. A., & Holloway, S. D., 2003. Subduction factory 2. Are intermediate-depth earthquakes in subducting slabs linked to metamorphic dehydration reactions?, *J. Geophys. Res.*, **108**(B1), 1–20.

Holland, T. J. B., Redfern, S. A. T., & Pawley, A. R., 1996. Volume behavior of hydrous minerals at high pressure and temperature: II. Compressibilities of lawsonite, zoisite, clinozoisite, and epidote, *Amer. Mineral.*, **81**, 341–348.

Husker, A. & Davis, P. M., 2009. Tomography and thermal state of the Cocos plate subduction beneath Mexico City, *J. Geophys. Res.*, **114**(B04306), 1–15.

Hyndman, R. D. & Wang, K., 1993. Thermal constraints on the zone of possible major thrust earthquake failure on the Cascadia margin, *J. Geophys. Res.*, **98**, 2039–2060.

Jacobsen, S. D. & van der Lee, S., 2006. *Earth's Deep Water Cycle*, American Geophysical Union, Washington, DC.

James, D. E., Boyd, F. R., Schutt, D., Bell, D. R., & Carlson, R. W., 2004. Xenolith constraints on seismic velocities in the upper mantle beneath southern Africa, *Geochem. Geophys. Geosyst.*, **5**(1), 1–32.

Johnson, E. R., Wallace, P. J., Granados, H. D., Manea, V. C., Kent, A. J. R., Bindeman, I. N., & Donegan, C. S., 2009. Subduction-related volatile recycling and magma generation beneath central Mexico: Insights from melt inclusions, oxygen isotopes and geodynamic models, *J. Petrology*, **50**(9), 1729–1764.

Kawakatsu, H. & Watada, S., 2007. Seismic evidence for deep-water transportation in the mantle, *Science*, **316**, 1468–1471.

Kennett, B. L. N. & Engdahl, E. R., 1991. Traveltimes for global earthquake location and phase identification, *Geophys. J. Int.*, **105**(2), 429–465.

Kikuchi, M. & Kanamori, H., 1982. Inversion of complex body waves, *Bull. Seism. Soc. Am.*, **72**(3), 491–506.

Kim, Y., Clayton, R. W., & Jackson, J. M., 2010. Geometry and seismic properties of the subducting Cocos plate in central Mexico, *J. Geophys. Res.*, **115**(B6), 1–22.

Larson, K., Kostoglodov, V., Miyazaki, S., & Santiago, J. A. S., 2007. The 2006 aseismic slow slip event in Guerrero, Mexico: New results from GPS, *Geophys. Res. Lett.*, **34**(L13309), 1–5.

Ligorria, J. P. & Ammon, C. J., 1999. Iterative deconvolution and receiver-function estimation, *Bull. Seism. Soc. Am.*, **89**(5), 1395–1400.

Mainprice, D. & IIdefonse, B., 2009. *Subduction Zone Geodynamics*, pp. 63–84, Springer.

Manea, V. C., Manea, M., Kostoglodov, V., Currie, C. A., & Sewell, G., 2004. Thermal structure, coupling and metamorphism in the Mexican subduction zone beneath Guerrero, *Geophys. J. Int.*, **158**, 775–784.

Maruyama, S. & Okamoto, K., 2007. Water transportation from the subducting slab into the mantle transition zone, *Gondwana Res.*, **11**, 148–165.

Mavko, G., Mukerji, T., & Dvorkin, J., 2003. *The Rock Physics Handbook: Tools for Seismic Analysis of Porous Media*, Cambridge University Press, Cambridge, United Kingdom.

Melgar, D. & Pérez-Campos, X., 2010. Imaging the Moho and Subducted Oceanic Crust at the Isthmus of Tehuantepec, Mexico, from Receiver Functions, *Pure Appl. Geophys.*, pp. 1–12.

Minson, S., 2010. *A Bayesian Approach to Earthquake Source Studies*, Phd thesis, California Institute of Technology, Pasadena, California.

Morán-Zenteno, D. J., Cerca, M., & Keppie, J. D., 2007. The Cenozoic tectonic and magmatic evolution of southwestern Mexico: Advances and problem interpretation, *Spec. Pap. Geol. Soc. Am.*, **422**, 71–91.

Nicholson, T., Bostock, M. G., & Cassidy, J. F., 2005. New constraints on subduction zone structure in northern Cascadia, *Geophys. J. Int.*, **161**, 849–859.

Nieto-Samaniego, A. F., Alaniz-Álvarez, A. S., Silva-Romo, G., Eguiza-Castro, M. H., & Mendoza-Rosales, C., 2006. Latest Cretaceous to Miocene deformation events in the eastern Sierra Madre del Sur, Mexico, inferred from the geometry and age of major structures, *Geol. Soc. Am. Bull.*, **118**, 238–252.

Pardo, M. & Suárez, G., 1995. Shape of the subducted Rivera and Cocos plates in southern Mexico: Seismic and tectonic implications, *J. Geophys. Res.*, **100**(B7), 12357–12373.

Pawley, A. R., Redfern, S. A. T., & Holland, T. J. B., 1996. Volume behavior of hydrous minerals at high pressure and temperature: I. Thermal expansion of lawsonite, zoisite, clinozoisite, and diaspore, *Amer. Mineral.*, **81**, 335–340.

Payero, J. S., Kostoglodov, V., Shapiro, N., Mikumo, T., Iglesias, A., Pérez-Campos, X., & Clayton, R. W., 2008. Nonvolcanic tremor observed in the Mexican subduction zone, *Geophys. Res. Lett.*, **35**(L07305), 1–6.

Pérez-Campos, X., Kim, Y., Husker, A., Davis, P. M., Clayton, R. W., Iglesias, A., Pacheco, J. F., Singh, S. K., Manea, V. C., & Gurnis, M., 2008. Horizontal subduction and truncation of the Cocos Plate beneath central Mexico, *Geophys. Res. Lett.*, **35**(18), 1–6.

Ringwood, A. E. & Green, D. H., 1966. An experimental investigation of the Gabbro-Eclogite transformation and some geophysical implications, *Tectonophysics*, **3**(5), 383–427.

Rondenay, S., Abers, G. A., & van Keken, P. E., 2008. Seismic imaging of subduction zone metamorphism, *Geology*, **34**, 275–278.

Schilling, F. R., Sinogeikin, S. V., & Bass, J. D., 2002. Single-crystal elastic properties of lawsonite and their variation with temperature, *Phys. Earth Planet. Inter.*, **136**, 107–118.

Scott, H. P. & William, Q., 1999. An infrared spectroscopic study of lawsonite to 20 GPa, *Phys. Chem. Minerals*, **26**, 437–445.

Sinogeikin, S. V., Schilling, F. R., & Bass, J. D., 2000. Single crystal elasticity of lawsonite, *Amer. Mineral.*, **85**, 1834–1837.

Song, T. A., Helmberger, D. V., Brudzinski, M. R., Clayton, R. W., Davis, P., PérezCampos, X., & Singh, S. K., 2009. Subducting slab ultraslow velocity layer conincident with silent earthquake in southern Mexico, *Science*, **324**, 502–506.

Tarantola, A., 2005. *Inverse Problem Theory and Methods for Model Parameter Estimation*, Society for Industrial and Applied Mathematics, Philadelphia, PA, US.

Tatham, D. L., Lloyd, G. E., Butler, R. W. H., & Casey, M., 2008. Amphibole and lower crustal seismic properties, *Earth Planet. Sci. Lett.*, **267**, 118–128.

Tsuji, Y., Nakajima, J., & Hasegawa, A., 2008. Tomographic evidence for hydrated oceanic crust of the Pacific slab beneath northeastern Japan: Implications for water transportation in subduction zones, *Geophys. Res. Lett.*, **35**, 1–5.

Valdes-Gonzalez, C. & Meyer, R. P., 1996. Seismic structure between the Pacific coast and Mexico City from the Petatlan earthquake (Ms = 7.6) aftershocks, *Geofis. Int.*, **35**, 4377–4401.

Vergnolle, M., Walpersdorf, A., Kostoglodov, V., Tregoning, P., Santiago, J. A., Cotte, N., & Franco, S. I., 2010. Slow slip events in Mexico revised from the processing of 11 year GPS observations, *J. Geophys. Res.*, **115**(B08403), 1–18.

Wagner, L. S., Anderson, M. L., Jackson, J. M., Beck, S. L., & G., Z., 2008. Seismic evidence for orthopyroxene enrichment in the continental lithosphere, *Geology*, **36**, 935–938.

Yuan, X., Sobolev, S. V., Kind, R., Oncken, O., Bock, G., Asch, G., Schurr, B., Graeber, F., Rudloff, A., Hanka, W., Wylegalla, K., Tibi, R., Haberland, C., Rietbrock, A., Giese, P., Wigger, P., Röwer, P., Zandt, G., Beck, S., Wallace, T., Pardo, M., & Comte, D., 2000. Subduction and collision processes in the Central Andes constrained by converted seismic phases, *Nature*, **408**, 958–961.

Chapter 4

Generation of Talc from the Mantle Wedge and its Role in the Subduction Dynamics in Central Mexico

Abstract

Modeling of the receiver function (RF) conversion amplitudes of the underplated features in central Mexico reveals a thin very-low-velocity zone between the plate and the continental crust that appears to absorb nearly all of the strain between the upper plate and the Cocos slab. Using Vp/Vs as a function of S wave velocity (Vs) in a range of likely pressures and temperatures for candidate mineral phases, the thin upper oceanic crust in the flat slab region of central Mexico is determined to be enriched with hydrous minerals such as talc over the normal oceanic crustal compositions such as MORB-like gabbro. From a petrologic point of view, the generation of talc by the oceanic crust subduction at the trench side is nearly impossible. We therefore propose that the talc-rich layer in the upper oceanic crust is generated from the mantle wedge side during the slab flattening process coupled with trench rollback. The talc-rich rocks at the slab interface can be formed in the mantle by the addition of silica transported by rising fluids via the dehydration reaction from the subducting oceanic crust and by mechanical mixing of mantle and siliceous rocks. The thin low-strength layer decouples the horizontal slab from the continental crust, and originated from the mantle wedge side rather than the trench side. The evolution of this low-strength zone has important implications for the dynamics of the subduction system including the flattening process of the slab as well as the geochemistry of the mantle wedge and arc in central Mexico.

4.1 Introduction

Knowledge of the material properties of mineral phase assemblages plays a central role in interpretation of geophysical observations and geodynamic simulations. Hydrous minerals initially form within oceanic lithosphere as a result of hydrothermal circulation and alteration at spreading ridges, along fracture zones, and in the region of the trench and outer rise (Maruyama & Okamoto, 2007; Audet et al., 2009). About 5−6 wt.% H_2O is stored in hydrous minerals due to ocean-floor hydrothermal metamorphism (Maruyama & Okamoto, 2007). As oceanic crust subducts, mineral-bound H_2O is transported down into the mantle (Abers, 2000; Hacker et al., 2003b; Maruyama & Okamoto, 2007; Mainprice & IIdefonse, 2009). The evidence has been seismically detected in various subduction environments as a low-velocity layer at the top of the subducting plate (e.g, Alaska (Rondenay et al., 2008), Cascadia (Nicholson et al., 2005; Audet et al., 2009), Central Andes (Yuan et al., 2000), and northeast Japan (Kawakatsu & Watada, 2007; Tsuji et al., 2008)).

In particular, the receiver function (RF) analysis based on high-frequency teleseisms for central Mexico (Figure 4.1) showed that shallowly subducting Cocos plate horizontally underplates the continental crust for ∼200 km from the Pacific coast to the Trans-Mexican Volcanic Belt (TMVB) (Figure 4.2) (Pérez-Campos et al., 2008; Kim et al., 2010). Modeling of the RF amplitudes of the underplated features suggested anomalously low shear speeds (Vs) of 2.4-3.4 km/s at the upper horizontal layer of the oceanic crust with a thickness of 4±1 km at a depth of ∼45 km (Kim et al., 2010). Similar velocities were also obtained by modeling local converted S-to-P phases and teleseismic underside reflections (Song et al., 2009). These seismic velocities are far too low with respect to velocities obtained for unaltered MORB and gabbro over ranges of pressure (P)-temperature (T) space (Hacker et al., 2003a). Manea & Gurnis (2007) suggested that a thin channel of low-velocity mantle (LVC) above the subducted oceanic crust in central Mexico is a remnant of the mantle wedge, and provided a numerical model to support the current flat-slab configuration. The candidate mineral phase such as talc (low-strength hydrous mineral) is proposed for such a low speed at the depth of the flat slab (∼45 km) and a range of likely temperatures (500−800°C) (Figure 4.2).

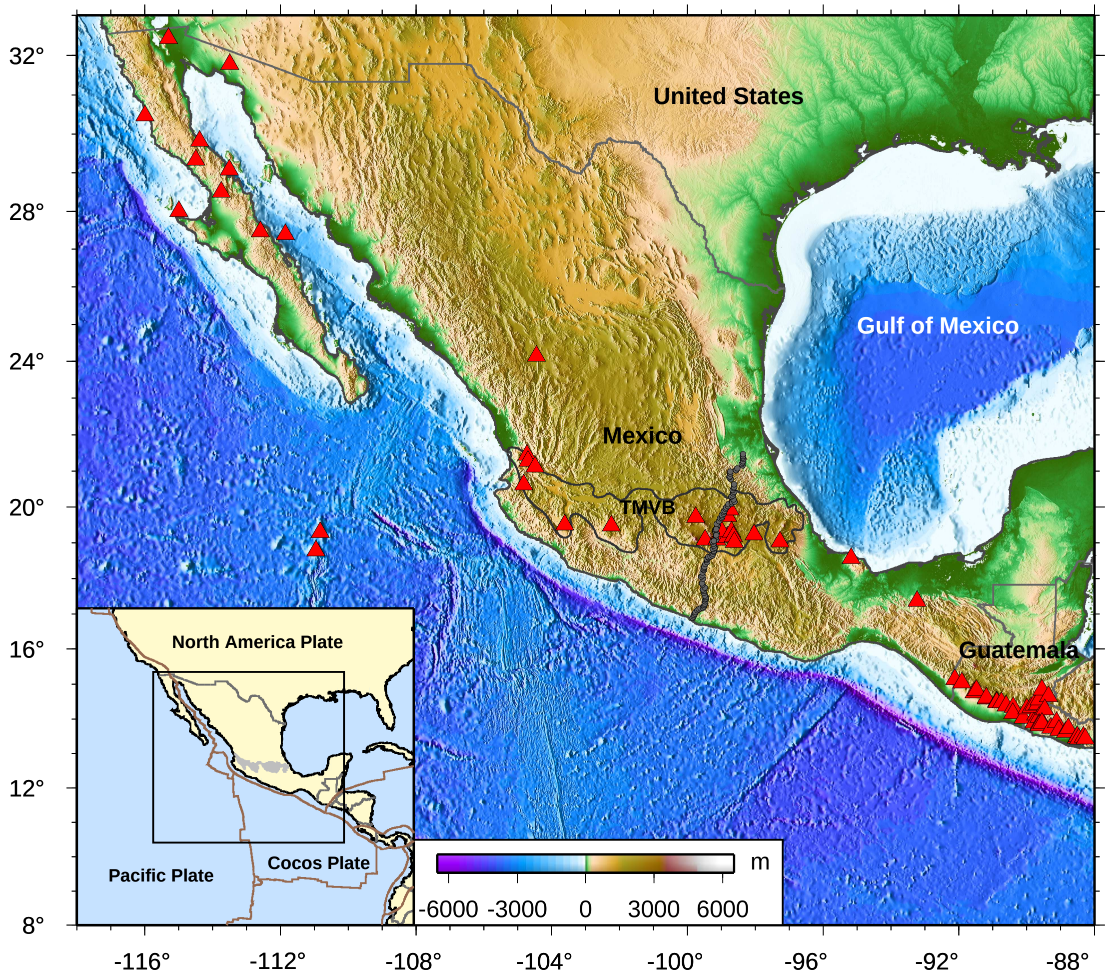

Figure 4.1: Topography map of the Mexico subduction zone with 100 broadband seismic stations from the Meso-American Subduction Experiment (MASE) in central Mexico. Dark gray-filled circles indicate the seismic stations, and red triangles indicate the location of active volcanoes. Dark gray line in the North American continent delineates Quaternary volcanic arc known as Trans-Mexican Volcanic Belt (TMVB).

In this paper, we discuss two cases for the genesis of talc in the upper oceanic crust of the subducted Cocos plate in central Mexico, and suggest that the talc formation from the trench side is not possible based on the P-T curve for equilibria involving talc, calculated from thermodynamic data (Deer et al., 1992). Also, we discuss its critical role on the subduction dynamics during the flattening process since ∼20 Ma coupled with trench rollback.

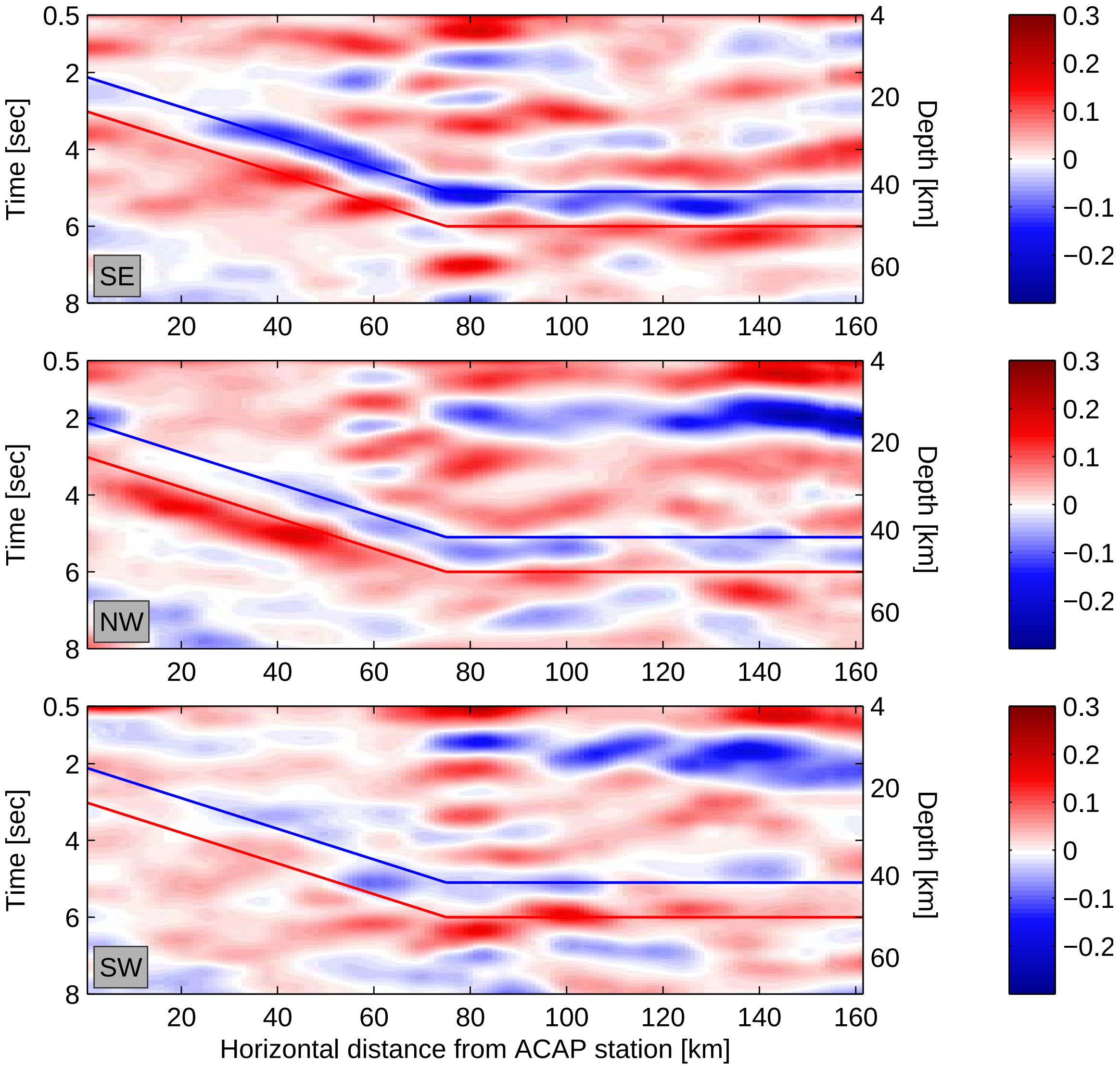

Figure 4.2: Receiver function (RF) images showing the shallow-to-flat slab structure from the Pacific coast to inland Mexico. The images are plotted according to different back-azimuth (SE, NW and SW) bands, and are constructed in the frequency ranges of 0.01−1 Hz. These images are produced by assigning the amplitude of stacked RF within a spatial grid and linearly interpolating among stations, which are typically 6 km apart in the MASE. The P wave in the stacked RF is removed to enhance the converted PS waves, and the color of the image represents the absolute amplitude of RFs. The negative and positive RF conversions at the top and bottom of the oceanic crust are shown as blue and red lines, respectively.

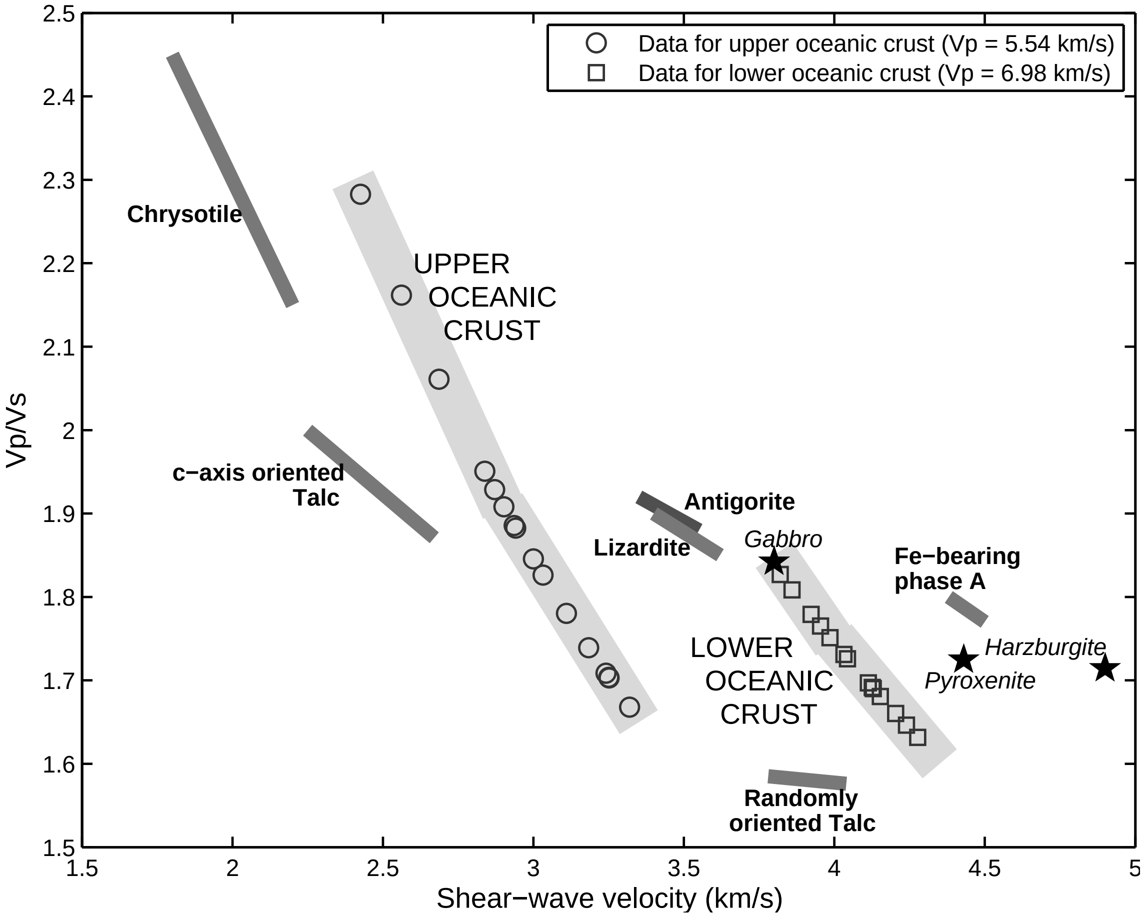

Figure 4.3: Calculated Vp/Vs ratio versus S wave velocity (Vs) at the depth of the flat slab and a range of likely temperatures (500−800°C) for candidate hydrated phases (gray lines) and rock types (black stars). We note that the data corresponding to the flat slab region (∼40−50 km depth) are plotted in this figure. The points for randomly oriented talc and c axis oriented talc are from Mainprice et al. (2008), and those for different rock types from Christensen & Salisbury (1975). The light-gray shaded regions denote uncertainties due to the choice of Vp. The lower bound of the uncertainty for the upper oceanic crust is computed when Vp = 5.39 km/s, and the upper bound is when Vp = 5.69 km/s. The lower bound of the uncertainty for the lower oceanic crust is computed when Vp = 6.90 km/s, and the upper bound is when Vp = 7.06 km/s.

4.2 Generation of Talc at the Thin Horizontal Interface of the Subducted Cocos Plate

During transport of oceanic crust from the mid-ocean ridge to the trench, there are no significant metamorphic and dynamic events occurring between the mid-oceanic ridge and subduction zone (Buck et al., 2000). The dominant process in the Middle America Trench (MAT), inferred from the free-air gravity anomaly, is suggested to be sediment subduction and scraping of unconsolidated pelagic sediments from the top of the subducting oceanic plate (Manea et al., 2003). The terrigenous sediment contribution is suggested to be minimal (Manea et al., 2003). Previous seismic-refraction profiles at the MAT near Acapulco suggest that the thickness of the oceanic crust is 7-8 km (Shor & Fisher, 1961). The sedimentary (mostly unconsolidated pelagic) layer has a thickness of 0.6 km (P wave velocity, Vp = 2.15 km/s), the basement of 1.3 km (Vp = 5.74 km/s), and main crustal layer of 5.2 km (Vp = 6.75 km/s) (Shor & Fisher, 1961). Hydrated metabasalt oceanic crust subducts beneath the North American plate, undergoes subduction-zone metamorphism and continues to release H_2O via dehydration reactions to the overlying mantle wedge.

In central Mexico, the Cocos oceanic crust subducts at an angle of ~15° for 80 km inland from coastline and turns horizontal for ~200 km to the start of the TMVB (Figure 4.2) (Pérez-Campos et al., 2008; Kim et al., 2010). Based on the RF modeling results, the thickness of the oceanic crust is estimated to be $\sim 8-10$ km, and the upper oceanic crustal thickness is 4±1 km. Strong RF conversions at the top and bottom of the oceanic crust (Figure 4.2) provided constraints on the properties of the interfaces that had been intrepreted by computing seismic velocities in slab mineralogies. A large concentration of the hydrous mineral talc in the upper oceanic crust (Figure 4.3) was proposed to reconcile the extremely low seismic velocities (Kim et al., 2010). There is in fact no lithology identified in the phase diagrams provided by Hacker et al. (2003a), which can explain our observed speeds. Any drastic changes in subducted crust composition as a result of alteration and interaction with fluids and melts could potentially change its stability fields and allow greater hydration or formation of talc and related minerals. However, such a case is considered to be speculative and highly unlikely to happen based on the past tectonic activity of central Mexico. One possible mechanism to explain such a low-velocity anomaly in the upper oceanic crust is that lower crustal rocks contain an unreasonably high amount of free water ($>\sim$20 wt.%) to reduce the velocities significantly (Figure 4.4).

Talc has a P-T range of stability that extends from surficial to eclogite-facies conditions, making it of potential significance in various faulting environments (Moore & Lockner, 2008). Because of its aseismic and thermally stable behavior (~800°C at 1−2 GPa), talc may play a role in stabilizing slip at depth in a subduction zone (Moore & Lockner, 2008). In particular, talc has been recently identified in the San Andreas fault to explain the aseismic slip of the creeping section (Moore & Rymer, 2007). Talc mainly forms as a result of the reaction of serpentine minerals with silica-saturated fluid released from the subducting slab (Peacock & Hyndman, 1999; Moore & Rymer, 2007; Moore & Lockner, 2008; Wang et al., 2009). Wang et al. (2009) reported the occurrence of talc in serpentinized peridotites collected from the landward trench slope of the southern Mariana forearc, and suggested that a prominent low-velocity layer beneath the Izu-Bonin-Mariana forearc is from the serpentinized upper mantle acting as a lubricant along the plate boundary. Peacock & Hyndman (1999) and Abers et al. (2006) both suggested that the metasomatic talc at the slab-mantle interface controls the downdip limit of subduction-zone earthquakes.

Based on the P-T diagrams for depleted lherzolite and harzburgite with no free water, 11 v.% of talc above the oceanic crust or 15 v.% below the oceanic crust can be present (Hacker et al., 2003a). However, very little talc can be formed from a MORB composition (Hacker et al., 2003a). Based on the P-T curve for equilibria involving talc based on available thermodynamic data (Deer et al., 1992), the formation of talc in the upper oceanic crust, starting with a basaltic composition is nearly impossible. For any metamorphosed basalt at the pressure of ~1.5 GPa (at the depth of the flat slab), it takes an unreasonable amount of free water to obtain the Vs values sufficiently low to match with the upper oceanic crustal data (Figure 4.4). Figure 4.4 also suggests that it is only feasible to generate the talc from the altered mantle lithologies such as harzburgite, based on mineral physics data. We thus propose that the talc-rich layer in the upper oceanic crust is generated from the mantle wedge side rather than from the MAT during the slab flattening process coupled with trench

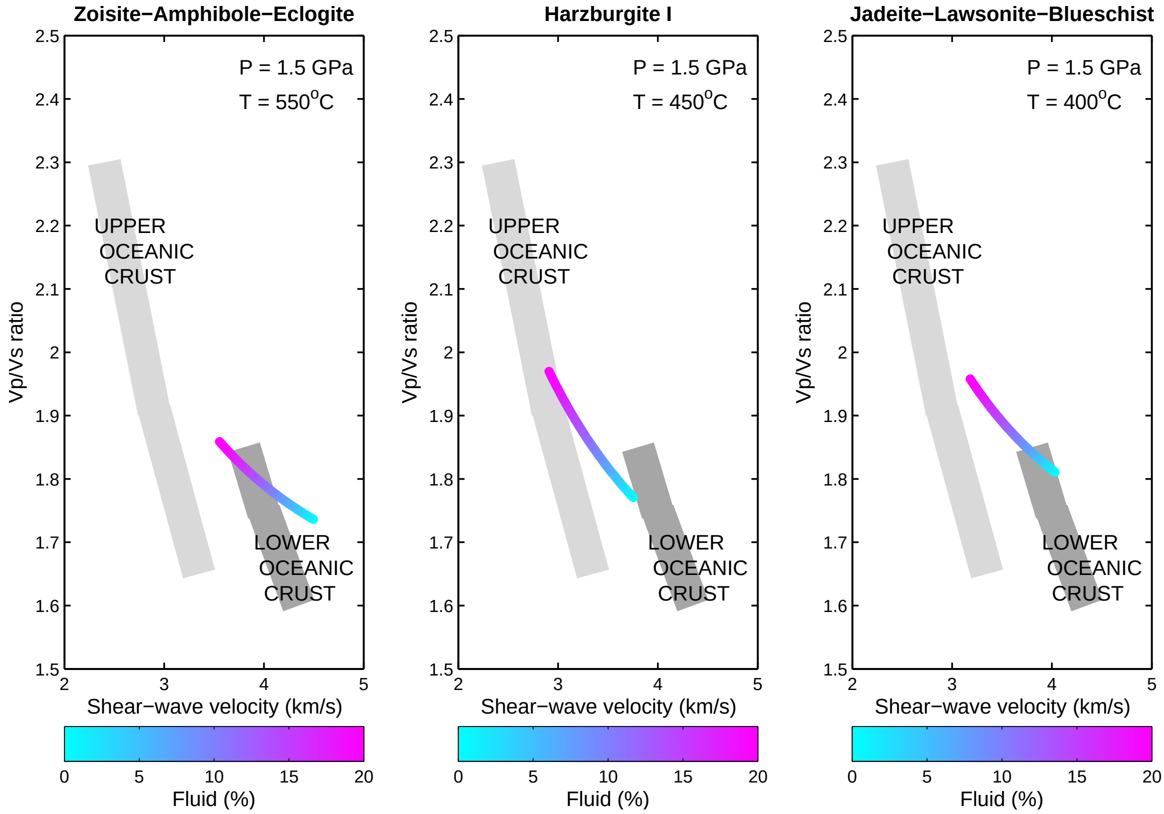

Figure 4.4: Calculated Vp/Vs ratio versus Vs at a depth of ∼40−50 km for candidate rocks considering free water from 0 to 20 wt.%. The calculation of the seismic parameters with the free water component (sphere geometry with an aspect ratio of 0.5) are based on Schmeling (1985). For each phase, the seismic velocites are computed according to slightly different temperatures at 1.5 GPa based on its stability field suggested by Hacker et al. (2003a). Light- and dark-gray shaded regions denote upper and lower oceanic crustal data considering different choices of Vp, respectively (Figure 4.4).

rollback since 17-12 Ma (Ferrari et al., 1999). The low-velocity talc-rich layer evident along the oceanic crust can also be the slip plane for the slow slip events (Larson et al., 2007; Vergnolle et al., 2010).

4.3 Influence of Talc on Subduction Dynamics

Manea & Gurnis (2007) previously proposed that the dehydration of subducting lithosphere lowers the viscosity on top of the subducting slab, and showed that the low-viscosity channel (LVC) has a significant influence on the slab evolution based on numerical models. Manea & Gurnis (2007) obtained a narrow range ($5-10\times10^{19}$ Pa s) of mantle viscosities that produce present flat slab configurations, and showed that the slab flattening process is further enhanced by the trench rollback and that the presence of the LVC can explain the absence of deformation within the continental crust above the flat slab regime. This low-viscosity layer can very well be the observed low-velocity layer, which is determined to be enriched with frictionally weak talc phases generated from the hydrated peridotites in the mantle wedge and completely decoupled from the overlying plate. Due to its unique physical properties, discussed in Section 4.2, a large concentration of talc in the upper oceanic crust plays a significant role in the subduction dynamics in central Mexico.

4.4 Conclusions

The hydrous mantle mineral talc has been previously proposed to explain anomalously low shear wave speeds at the subducted (top) interface of the Cocos plate in central Mexico. This study suggests that this large concentration of talc comes from the mantle wedge rather than from the trench based on the stability field of talc at the depth of the flat slab, and is created by serpentines in hydrated peritodites in the mantle wedge interacting with Si-saturated fluids via dewatering of the subducted slab. Our hypothesis is fully consistent with published time-dependent numerical models for generating the flat slab configuration. The evolution of the thin low-shear zone, enriched with low-strength talc, generated from the mantle wedge has significant implications for the subduction dynamics as well as the geochemistry of the mantle wedge and arc beneath the Trans-Mexican Volcanic Belt.

Bibliography

Abers, G. A., 2000. Hydrated subducted crust at 100−250 km depth, *Earth Planet. Sci. Lett.*, **176**, 323–330.

Abers, G. A., van Keken, P. E., Kneller, E. A., Ferris, A., & Stachnik, J. C., 2006. The thermal structure of subduction zones constrained by seismic imaging: Implications for slab dehydration and wedge flow, *Earth Planet. Sci. Lett.*, **241**, 387–397.

Audet, P., Bostock, M. G., Christensen, N. I., & Peacock, S. M., 2009. Seismic evidence for overpressured subducted oceanic crust and megathrust fault sealing, *Nature*, **457**, 76–78.

Buck, W. R., Delaney, P. T., Karson, J. A., & Lagabrielle, Y., 2000. *Faulting and Magmatism at Mid-Ocean Ridges*, American Geophysical Union, Washington, D.C.

Christensen, N. I. & Salisbury, M. H., 1975. Structure and constitution of the lower oceanic crust, *Rev. Geophys. Space Phys.*, **13**, 57–86.

Deer, W. A., Howie, R. A., & Zussman, J., 1992. *An Introduction to the Rock-Forming Minerals, 2nd ed.*, Longman Scientific & Technical.

Ferrari, L., López-Martinez, M., Aquirre-Díaz, G., & Carrasco-Niúñez, G., 1999. Space-time patterns of Cenozoic arc volcanism in central Mexico: From the Sierra Madre Occidental to the Mexican Volcanic Belt, *Geology*, **27**(4), 303–306.

Hacker, B. R., Abers, G. A., & Peacock, S. M., 2003a. Subduction Factory 1. Theoretical mineralogy, densities, seismic wave speeds, and H_2O contents, *J. Geophys. Res.*, **108**, 1–26.

Hacker, B. R., Peacock, S. M., Abers, G. A., & Holloway, S. D., 2003b. Subduction factory 2. Are intermediate-depth earthquakes in subducting slabs linked to metamorphic dehydration reactions?, *J. Geophys. Res.*, **108**(B1), 1–20.

Kawakatsu, H. & Watada, S., 2007. Seismic evidence for deep-water transportation in the mantle, *Science*, **316**, 1468–1471.

Kim, Y., Clayton, R. W., & Jackson, J. M., 2010. Geometry and seismic properties of the subducting Cocos plate in central Mexico, *J. Geophys. Res.*, **115**(B6), 1–22.

Larson, K., Kostoglodov, V., Miyazaki, S., & Santiago, J. A. S., 2007. The 2006 aseismic slow slip event in Guerrero, Mexico: New results from GPS, *Geophys. Res. Lett.*, **34**(L13309), 1–5.

Mainprice, D. & IIdefonse, B., 2009. *Subduction Zone Geodynamics*, pp. 63–84, Springer.

Mainprice, D., Le Page, Y., Rodgers, J., & Jouanna, P., 2008. *Ab initio* elastic properties of talc from 0 to 12 GPa: Interpretation of seismic velocities at mantle pressures and prediction of auxetic behaviour at low pressure, *Earth Planet. Sci. Lett.*, **274**, 327–338.

Manea, M., Manea, V. C., & Kostoglodov, V., 2003. Sediment fill in the Middle America Trench inferred from gravity anomalies, *Geofis. Int.*, **42**, 603–612.

Manea, V. C. & Gurnis, M., 2007. Subduction zone evolution and low viscosity wedges and channels, *Earth Planet. Sci. Lett.*, **264**, 22–45.

Maruyama, S. & Okamoto, K., 2007. Water transportation from the subducting slab into the mantle transition zone, *Gondwana Res.*, **11**, 148–165.

Moore, D. E. & Lockner, D. A., 2008. Talc friction in the temperature range $25°-400°$C: Relevance for fault-zone weakening, *Tectonophysics*, **449**, 120–132.

Moore, D. E. & Rymer, M. J., 2007. Talc, serpentinite, and the creeping section of the San Andreas fault, *Nature*, **448**, 795–797.

Nicholson, T., Bostock, M. G., & Cassidy, J. F., 2005. New constraints on subduction zone structure in northern Cascadia, *Geophys. J. Int.*, **161**, 849–859.

Peacock, S. M. & Hyndman, R. D., 1999. Hydrous minerals in the mantle wedge and the maximum depth of subduction thrust earthquakes, *Geophys. Res. Lett.*, **26**(16), 2517–2520.

Pérez-Campos, X., Kim, Y., Husker, A., Davis, P. M., Clayton, R. W., Iglesias, A., Pacheco, J. F., Singh, S. K., Manea, V. C., & Gurnis, M., 2008. Horizontal subduction and truncation of the Cocos Plate beneath central Mexico, *Geophys. Res. Lett.*, **35**(18), 1–6.

Rondenay, S., Abers, G. A., & van Keken, P. E., 2008. Seismic imaging of subduction zone metamorphism, *Geology*, **34**, 275–278.

Schmeling, H., 1985. Numerical models on the influence of partial melt on elastic, anelastic and electric properties of rocks. Part I: elasticity and anelasticity, *Phys. Earth Planet. Inter.*, **41**, 34–57.

Shor, G. G. & Fisher, R. L., 1961. Middle America Trench: Seismic-refraction studies, *Geol. Soc. Am. Bull.*, **72**, 721–730.

Song, T. A., Helmberger, D. V., Brudzinski, M. R., Clayton, R. W., Davis, P., PérezCampos, X., & Singh, S. K., 2009. Subducting slab ultraslow velocity layer conincident with silent earthquake in southern Mexico, *Science*, **324**, 502–506.

Tsuji, Y., Nakajima, J., & Hasegawa, A., 2008. Tomographic evidence for hydrated oceanic crust of the Pacific slab beneath northeastern Japan: Implications for water transportation in subduction zones, *Geophys. Res. Lett.*, **35**, 1–5.

Vergnolle, M., Walpersdorf, A., Kostoglodov, V., Tregoning, P., Santiago, J. A., Cotte, N., & Franco, S. I., 2010. Slow slip events in Mexico revised from the processing of 11 year GPS observations, *J. Geophys. Res.*, **115**(B08403), 1–18.

Wang, X., Zeng, Z., Liu, C., Chen, J., Yin, X., Wang, X., Chen, D., Zhang, G., Chen, S., Li, K., & Ouyang, H., 2009. Talc-bearing serpentinized peridotites from the southern Mariana forearc: Implications for aseismic character within subduction zones, *Chinese J. Oceanol. Limnol.*, **27**(3), 667–673.

Yuan, X., Sobolev, S. V., Kind, R., Oncken, O., Bock, G., Asch, G., Schurr, B., Graeber, F., Rudloff, A., Hanka, W., Wylegalla, K., Tibi, R., Haberland, C., Rietbrock, A., Giese, P., Wigger, P., Röwer, P., Zandt, G., Beck, S., Wallace, T., Pardo, M., & Comte, D., 2000. Subduction and collision processes in the Central Andes constrained by converted seismic phases, *Nature*, **408**, 958–961.